Advancements in Beam Manipulation and Dynamic Control of Electromagnetic Waves Using Metamaterial Arrays and Voltage-Tunable Periodic Structures

Chi Leung Tsui

A dissertation

submitted in partial fulfillment of the

requirements for the degree of

Doctor of Philosophy

University of Washington

2023

Reading Committee:

Wei-Chih Wang, Chair

Lih Y. Lin, Chair

Blake Hannaford

Program Authorized to Offer Degree:

Electrical and Computer Engineering

University of Washington

Abstract

Advancements in Beam Manipulation and Dynamic Control of Electromagnetic Waves Using Metamaterial Arrays and Voltage-Tunable Periodic Structures

Chi Leung Tsui

Chair of the Supervisory Committee:
Wei-Chih Wang
Department of Mechanical Engineering
Lih Y. Lin
Department of Electrical Engineering

Traditional beam steering techniques employ both mechanical and non-mechanical methods, finding broad applications in optical communications, displays, image sensors, optical circuits, and laser-based manufacturing systems. However, each approach has inherent limitations. In this thesis, we address these shortcomings through the investigation of various beam steering system designs.

Firstly, we explored a mechanical system that utilizes a scanning waveguide driven by an integrated mechanical actuator. This innovation aims to reduce the system's footprint and overcome the limited field of view (FOV) associated with traditional mechanical systems.

Secondly, we introduce an electro-optic thin-film polymer beam scanner capable of achieving 2D scanning. This novel approach surpasses mechanical limitations while also exhibiting lower power consumption compared to traditional bulk crystal-based electro-optic devices.

To further enhance the performance, versatility, and robustness of the electro-optic scanner, we have recently developed a method of beam manipulation based on phase modulation, employing a voltage-tunable thin-film periodic structure known as the Tunable Gradient Fishnet Metamaterial (TGFMM). This device allows unique control of the optical beam through its discrete elements, facilitating effective beam manipulation. We have developed a model for the TGFMM, analyzing its transmission phase and refractive index to optimize its phase modulation performance and operating frequency. Subsequently, we conducted a numerical study to evaluate the device's beam manipulation capabilities. The optimized design was then fabricated on a flexible substrate, with special attention given to maintaining device robustness.

Furthermore, we characterized the prototype TGFMM and experimentally evaluated its beam manipulation performance using a terahertz frequency domain spectroscopy (THz-FDS) system. The results demonstrate successful beam deflection achieved by applying a gradient voltage profile, validating the prototype TGFMM's effectiveness in beam manipulation within the Terahertz (THz) frequency range. This research represents a significant advancement in beam steering technology, providing potential applications in various domains such as wireless communications, imaging, and sensing systems. The innovative techniques and insights presented in this thesis pave the way for more efficient and sophisticated beam steering technologies in the future, providing potential applications in various domains such as wireless communications, imaging, and sensing systems.

TABLE OF CONTENTS

LIST OF FIGURES

LIST OF TABLES

ACKNOWLEDGEMENTS

I want to give my special thanks to my co-advisor, Professor Wei-Chih Wang, for introducing me to novel projects in the laboratory and his guidance in my research in beam manipulation. His encouragement in exploring different idea has definitely help overcoming difficulties and challenges in this research. I would also like to thank my co-advisor Professor Lih Lin for her academic support and also for the knowledge that I have learned from her class and from our project collaborations.

I want to give my thanks for Geroge Mo, Ting-Chun Kuo, Aditya Sharma, Howard Chan at National Tsing Hua University Taiwan Institute of Nanoengineering and Microsystems (NTHU iNEMS) for their collaborative work on the fabrication and experiments of the project. It would have been very challenging to develop and realize the design without their collaboration.

Chapter 1. INTRODUCTION

1.1 BEAM MANIPULATION

Beam steering mechanisms can be typically found in many modern world technologies where optical beam is used. They can be found optical communication system for signal delivery [1], projection displays [2], 3D image acquisition systems [3], optical circuits [4], selective laser sintering systems, and optical tweezers for sub-micron particle manipulation [5]. Both mechanical and non-mechanical methods are used in the beam steering systems find in conventional devices.

Mechanical beam steering relies mechanical motions of components to deflect an incident beam. System parts are driven using electrostatic [2], electromagnetic [6], or piezoelectric effect [7], which converts applied electric field into mechanical energies. Due to mechanical motion of the components, these systems suffer from fatigue of the moving components due to cyclic loading, sensitivity to noise due to vibrations from the environment, and low operating frequencies due physics constraints of the actuating components. The FOV of the mechanical system is also limited by the system size, which imposed a challenge when reducing system footprint.

Non-mechanical systems alter the effective refractive index of waveguide medium to modulate the phase of the traversing optical beam. The elimination of moving parts allows non-mechanical systems to overcome the issues stemmed from mechanical motions in the system, however, each method presents their own disadvantages. Acousto-optic systems require large continuous large power to generate the acoustic wave to create diffraction effect in acousto-optic materials for beam deflection [8]. Thermo-optic systems tune the property of the thermo-optic

material by changing the temperature of the material. This method has a relatively slow response time compared to other methods and it induces thermal-stress to the medium and the performance of the device can be affected by temperature fluctuations in the environment [9]. Compared to the other methods, electro-optic devices provide high switching speed and they are less susceptible to environmental perturbations and induced stress. Thus, they are able to provide rapid and accurate relay of optical beam signals in both communication and display systems. To achieve large deflection effect, electro-optic systems typically rely on bulk crystals as the electro-optic medium [10][11][12], which requires high driving voltages and they typically have a large system footprint. To resolve this problems, thin-film electro-optic devices are developed. Thin-film devices compact the overall size of the beam steering system and reduce the require driving power. They are compatible with the current micromachining process, making them relatively easy to fabricate. However, the beam steering performance of thin film electro-optic systems is restricted by the electro-optic constant of the EO material, which tend to be much lower than the bulk crystals [13], thus limiting the potential performance of the device. To increase the performance of electro-optic thin-film device, beam steering using phase-array optics method is applied. Phased array optics uses arrays of phase modulating elements to introduce different phase delays to different parts of the incident beam. The combined results of the phase delays improve the beam deflections compared to a device with a single modulating element [14]. Meta-surfaces are one of the latest developments in phased-array optics that make use of periodic resonators to produce abrupt phase changes across the incident beam profile when operating near its resonance frequency. Its ability to manipulate the wave front using sub-wavelength cells encourages flat-optics design, such as the flat lens [15]. The resonance frequency of the meta-surfaces is dependent upon the geometry in each element in the array, thus

it is possible for the elements in the array to be made tunable by varying either the geometrical parameters. Zhu et al developed a tunable flat lens based on microfluidic reconfigurable meta-surface [16]. By loading and unloading liquid metal into nano-sized split ring channels, the effective refractive index in each module can be changed due the change in resonator geometry. Komar et al developed an all-dielectric tunable meta-surface with liquid crystal as a tunable media [17], and the effective refractive index in each cell is tuned by applying heat to in each cell to switch the liquid crystal from nematic to isotropic state. Compared to other tunable optics methods [18][19], these tunable structures are more compact due to its flat device profile, and more versatile due to higher tuning flexibility. However, the tunability, the performance, and the functionality of the meta-surfaces are often limited by the pre-defined geometric pattern [17], since the phase modulation is mainly contributed by the geometrical change of the surface. Tunable metamaterials are developed to provide further improvement to the flexibility of the tunable meta-surfaces since the tunability of the device does not rely on the variation in physical geometry, but rather it depends the permittivity change of the device. Brad et al [20] has demonstrated a tunable fishnet metamaterial that is capable of introducing large refractive index change by the minimal tuning the permittivity of the dielectric layer (Figure 1.1).

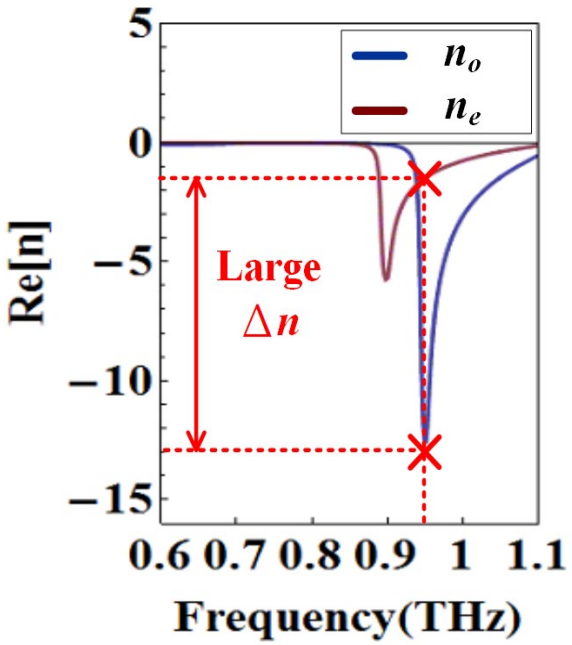

Figure 1.1. Large refractive index difference is achieved by switching the permittivity of dielectric layer in a tunable metamaterial structure described in [20]

1.2 TERAHERTZ

Terahertz (THz) radiation is gaining interest in the recent years for its unique characteristics. Its low energy level and its remarkable ability to penetrate opaque materials makes it potential for non-destructive sensing for security [21][22][23], and non-invasive medical imaging [24]. Being able to manipulate THz wave and modulate its phase is critical for these applications, thus, the development of beam steerers and phase shifters in the THz region is essential to its wide adoption.

1.2.1 *Terahertz Imaging*

Terahertz imaging systems functions by passing THz radiation through a target sample and analyzing the detected output signal. Current imaging systems are based on either Terahertz Time Domain Spectroscopy (THz-TDS) or Terahertz Frequency Domain Spectroscopy (THz-FDS).

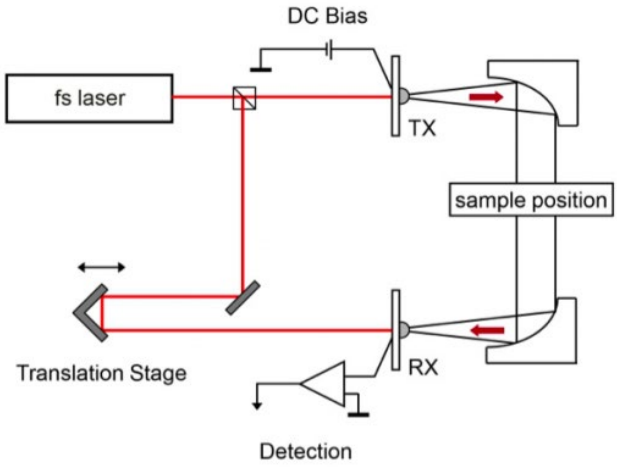

Figure 1.2. THz-TDS Imaging System [25]

In a THz-TDS system (Figure 1.2), the THz radiation is generated by the excitation of a low temperature grown gallium arsenide (LT-GaAs) photo conductive antenna using a femto-second pulse laser at the near infrared (NIR) frequency. The THz radiation is passed through the sample and the output electric field is detected using another LT-GaAS antenna. The output waveform of the detector antenna is compared to the time delayed input laser pulse after they are transformed into the frequency domain using Fast Fourier Transform (FFT) to obtain the spectrum of the sample.

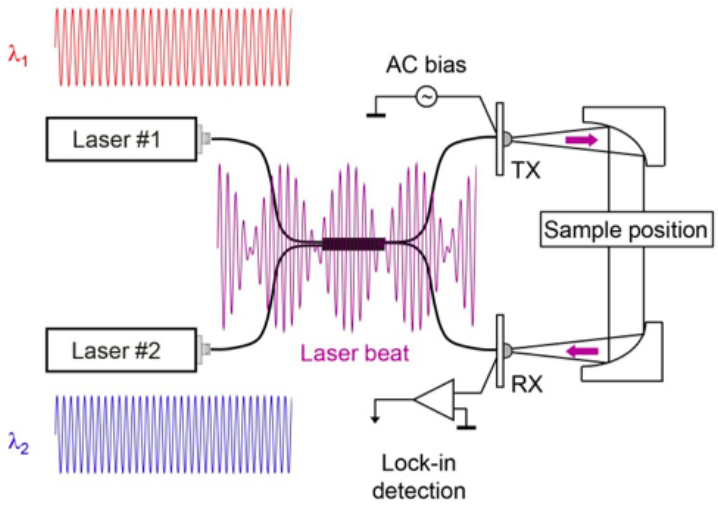

Figure 1.3. THz-FDS Imaging System [25]

In a THz-FDS system (Figure 1.3), the THz radiation is generated by mixing two continuous wave lasers with different frequencies and exciting a photomixer at the beat frequency of the two lasers. The THz radiation passes through the sample and the output electric field is detected. Frequency spectrum of the sample can be obtained by tuning the frequency on one of the continuous wave lasers to generate the desired beat frequency. Compared to THz-TDS system, the THz-FDS system allows for a less complex system due to less component requirement and also it provides a higher spectral resolution

Both of the THz imaging methods relies on mechanical scanning to acquire an image across an entire sample, which have unavoidable problems such as mechanical fatigue and instability, signal drift, limited Field of View (FOV), slow scanning speed and a low, fixed spatial resolution as described in Section 1.1.

1.3 PROPOSED WORK

In this project, a voltage tunable metamaterial beam manipulation device that is suitable for operating in the THz region is proposed to increase the change in the effective refractive index and phase of the device from the tuning of the Electro-optic (EO) material using electric field and allow fine manipulation of the beam profile via different control pattern of the discrete cells. The proposed Tunable Gradient Fishnet Metamaterial (TGFMM) device consists of an electro-optic material layer sandwiched between two specially design electrode geometry. The metal electrode is designed to be a periodic nano-cell fishnet-like pattern that will allow the local tuning the electro-optic layer forming a desire refractive index pattern. Another function of the periodic pattern is to introduce drastic change to the effective refractive index and the phase modulation of the device to potentially achieve large beam deflection while minimizing the required power consumption. The simple structure of the device will allow for a simple fabrication process and the footprint of the device will be compact. The proposed device will also be built on a flexible substrate as opposed to conventional substrate, which allows the device to be more versatile in its applications. Building the device on a flexible substrate also eases the integration of the device into other system due to the reduction in system footprint size.

Chapter 2. BACKGROUND AND PRIOR WORK

Various types of beam steering systems have been investigated prior to the development of the TGFMM with the goal of developing a system with compact footprint for ease of system integration. Different beam manipulation methods are explored and eventually inspired the design and development of the TGFMM device.

2.1 MECHANICAL BEAM STEERING

2.1.1 *2D Scanning Display with Mechanically Resonating Optical Fiber*

A pair of commercially available lead zirconate titanate (PZT) bimorph actuators are used to drive an optical fiber in a raster scanning motion, which eliminates the need of the mirrors and deflectors found in traditional mechanical system. Figure 2.1 shows the overall device configuration. The pair of PZT actuators are combined and arranged perpendicularly to actuations in orthogonal directions. The end of the vertically oriented actuator is anchored to form a fix-free structure. An optical fiber is attached at the free end of the actuator structure serves as a waveguide for the optical beam. During system operation, the optical fiber is excited by the actuators at near-resonant frequency to produce large deflection for large FOV, thus the power requirement is relatively low.

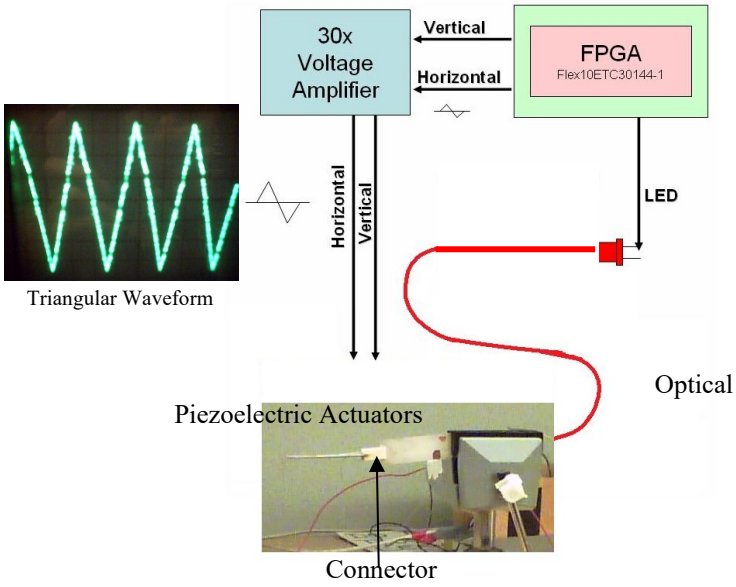

Figure 2.1. System Schematics for PZT Bimorph Actuated Scanner

A standalone FPGA system controls the driving waveforms for the pair of actuators at their respective pre-determined operating frequencies to create raster scanning motion. The frequencies are determined by Finite Element Analysis of the actuator geometry (Figure 2.2) to optimize the deflection angle of the waveguide and the resolution of the system.

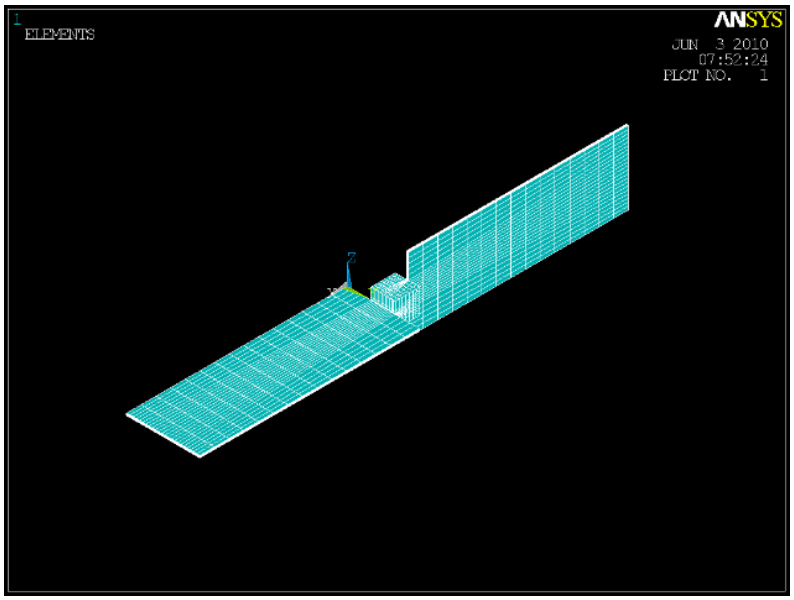

Figure 2.2. ANSYS Model of the PZT Bimorph Actuated Scanner

When operating at the resonant frequencies, the system is able to successfully drive the optical fiber in raster scanning motion with large displacement. When combined with a synchronized modulated LED, it is able to display simple static images of simple characters (Figure 2.3) that are preprogramed into the FPGA. However, the system is not able to produce consistent result every time it restarts and it requires an image comparison algorithm to tune the system's operating frequency during initialization [26]. This is due to the use of off-the-shelf parts, which make the assembly process of the system difficult and hard to repeat. Also, the system footprint is still relatively large for the resulting scanning area.

Figure 2.3. Output static images from the PZT Bimorph Actuated Scanner

2.1.2 *Aerosol PZT based Stainless Steel Scanner*

To reduce the overall size and increase system robustness, the off-the-shelf PZT actuator is replaced with a custom-designed actuator. The actuators in the new scanner design are arrange in a planar configuration (shown in Figure 2.4), and a waveguide is attached at the bridge connecting the two actuators. This configuration reduces the device's rigid length to ease the device's integration into compact optical systems. The planar design simplified the layout and composition

of the device and enabled the robust fabrication process of the device. The custom-designed PZT actuator will be fabricated with the aerosol PZT process [27]. The aerosol PZT deposition process is compatible with traditional MEMS fabrication flow, which makes the assembly process of the device simple, repeatable and robust against large variations. To form the actuator, PZT is deposited using the aerosol method onto the suspended part of a stainless steel substrate and a metal layer is deposited on top of the PZT. The stainless steel substrate and the top metal layer serves as the top and bottom electrode for exciting the PZT actuator. The PZT layer is then poled to enhance the piezoelectric effect. When a sinusoidal voltage is applied across the PZT layer, the PZT layer will expand and contract due to piezoelectric effect. The periodic excitation of the PZT layer will create vibrations and rotations on the bridge and drive the attached waveguide in motion. Modal Analysis is performed on the design geometry to predict the behavior of the waveguide for different driving frequencies and the results shows that the waveguide (in this case, a tapered fiber) will be driven in a horizontal motion at the second mode (Figure 2.5). Thus, it is shown to be possible to drive the waveguide in 2D motion with 1D actuators. It can be observed the 1st mode and the 2nd mode of the simulation model are at very similar frequencies, which is an expected result due to the symmetrical nature of the tapered fiber geometry. This result is consistent with the behavior of a similar MEMS actuator shown in [28], and the actuator is expected to be able to perform raster scanning when the driving method detailed in [28] is applied to the device. For high resolution scanning, a large deviation between the horizontal and vertical frequency is desired, thus a higher order mode obtained from the modal analysis needs to be selected as the operating frequency for either scanning direction. Additionally, harmonic analysis is performed to predict the displacement of the optical fiber. The result of modal analysis, harmonic analysis, and experimental measurement of the scanner system is reported in [29]. In the modal analysis, it is

observed the fiber is displaced horizontally with the actuators are out of phase at 930Hz and the optical fiber is displaced vertically with the actuators in phase at 5899Hz. This shows that 2D displacement of the scanning fiber is possible with 1D actuation of the actuators at 2 different frequencies. A harmonic analysis is then performed on the simulation model to predict the displacement of the fiber actuation at various modes. The harmonic analysis predicts that the optical fiber will have maximum displacements at 896 Hz, 5.4 kHz and 5.9kHz, which agrees with the results in the modal analysis. The displacement of the fiber on the device prototype (shown in Figure 2.6) fabricated using the methods detailed in [29] is experimentally measured via 2 different methods: optical observation and laser vibrometer. Both of the method concludes that the optical fiber will show maximum displacement at 896Hz, which matches with the results from the harmonic analysis. The image acquisition capability of the device is reported in [30] and the device is able to capture line pattern and cross pattern images on a target test mask via circular scanning of the fiber driven by the in-plane stainless steel actuators.

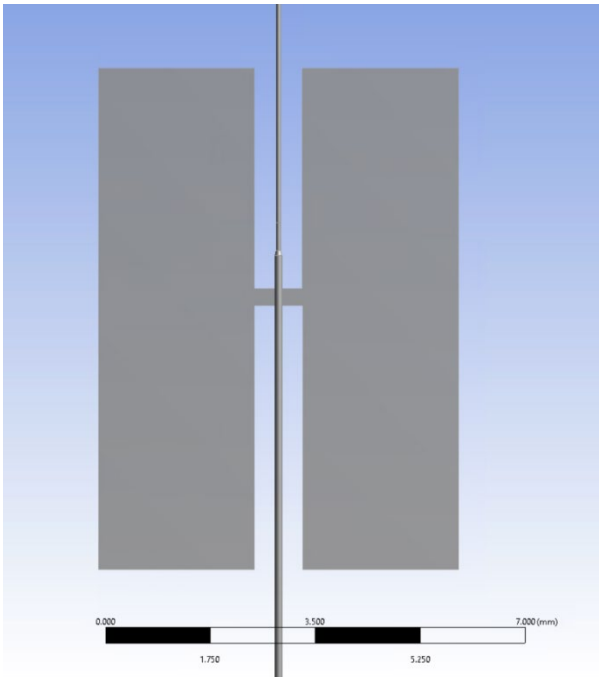

Figure 2.4. Aerosol PZT actuator design

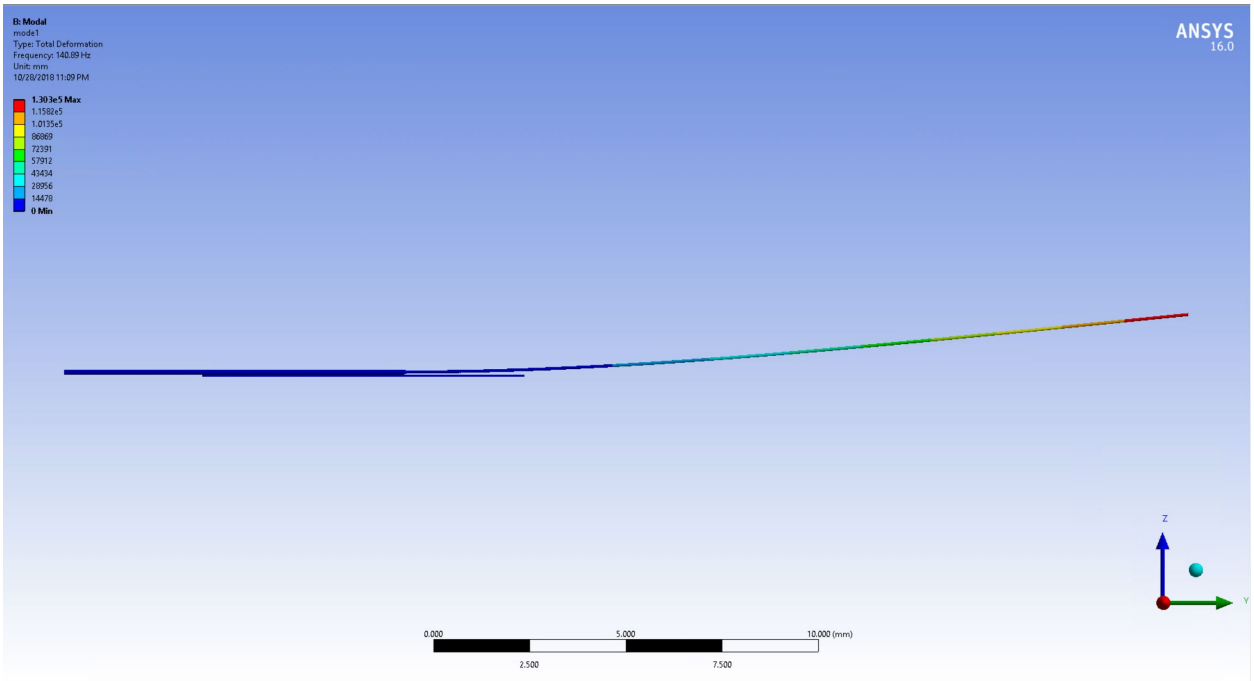

(a)

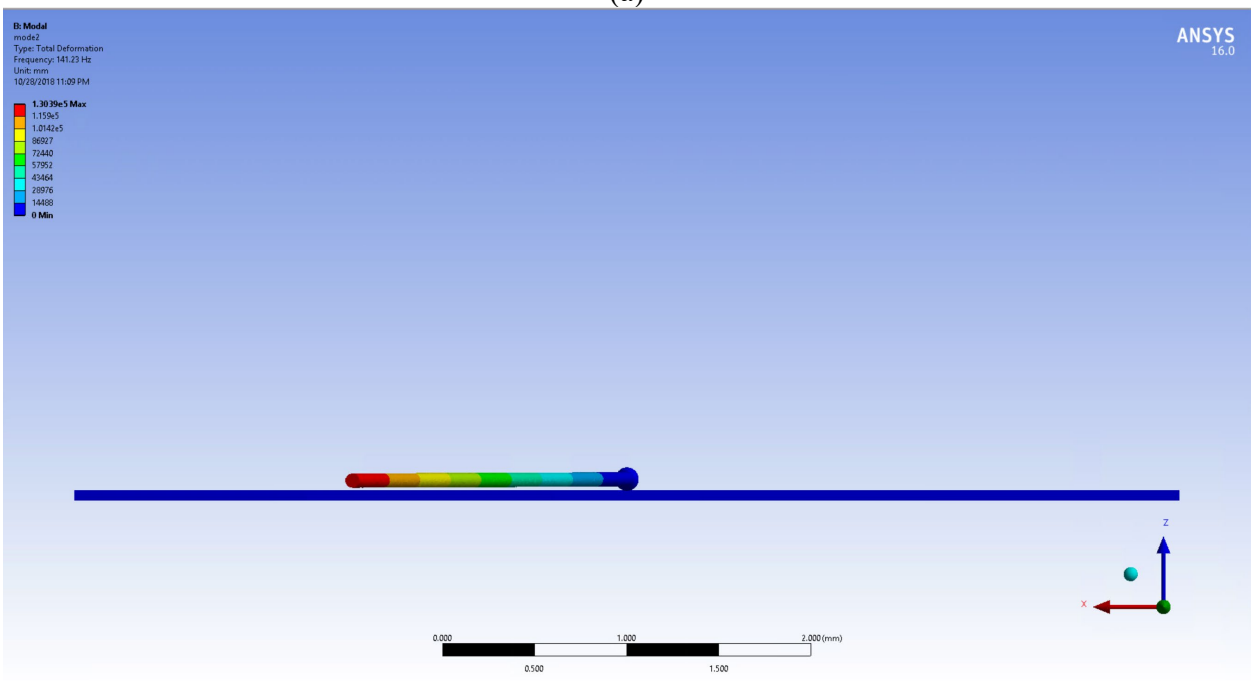

(b)

Figure 2.5. Modal Analysis Results of the preliminary PZT Actuator Geometry. (a) Deformation at 1st Mode (140.89Hz). (b) Deformation at 2nd Mode (141.23Hz)

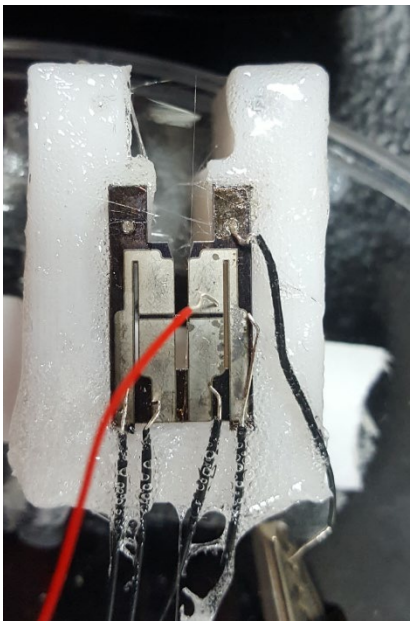

Figure 2.6. Device Prototype

2.2 Electro-optic Beam Steering Design

2.2.1 *2D Electro-optic Polymer Scanner*

While the improved designs of mechanical scanner can potentially decrease device footprint and improve the reliability of the system, it is still prone to problems that plague mechanical systems. To overcome the limitations in mechanical scanning systems, a beam scanner based on Electro-optic (EO) polymer is developed due to its many advantages over other non-mechanical methods [31]. The refractive index of an electro-optic material to change proportionally to applied electric field due to Pockel's effect (2.1):

$$\Delta n = \frac{1}{2} n^3 r E \tag{2.1}$$

where n is the refractive index of the material, r is the EO coefficient of the material and E is the electric field. The change in refractive index will change the refracting angle of an incident beam (Snell's Law) causing a variation in exit angle of the beam when different voltages are applied.

AJTB141/APC EO polymer [32] is used for the scanner due to relatively high refractive index compared to air, which makes it a suitable material as a waveguide. AJTB141/APC EO polymer has relatively high EO coefficient for thin-film EO material (45pm/V @ 1.3μm) and it can to be formed into a desired free-standing structure using hot embossing due to its ability to withstand the temperature of the process.

To achieve 2D beam steering, the EO scanner device [31] is consisted of a collimator stage, a prism stage, and a grating stage. The three stages are placed in cascading arrangement on a planar substrate to minimize the vertical profile of the system. The collimator stage is micro-fabricated SU-8 lens array used collimate the incident beam from an optical fiber into the subsequent stages. At the prism stage, the collimated beam is guided through the sidewall of a free standing EO prism array, the exit angle of the beam can be tuned by adjusting the voltage across the top and bottom of the prism structure and the geometry of the prism array is carefully designed to amplify the output angle change by maximizing the refraction angle on each prism interface. The free-standing prism structure is created by applying heat while molding the polymer under high pressure using a silicon mold as shown in Figure 2.7.

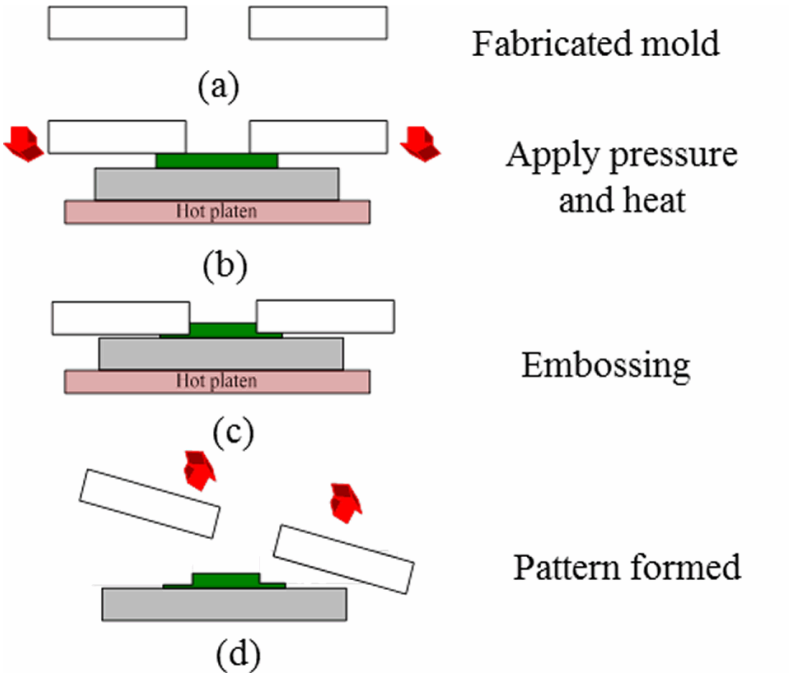

Figure 2.7. Hot Embossing Process

After the structure is formed, the EO Polymer is poled to improve its electro-optic effect along the direction of applied electric field. During the poling process, the temperature of the sample is gradually raised to just below its glass transition temperature, and then a variable voltage gradually increasing from 0 to 600V is applied to the sample. The current across the device is observed to ensure that the device is not damaged due to breakdown during the poling process.

At the grating stage, a polymer grating is placed on top of a free standing EO waveguide formed using the hot embossing method to couple the beam inside the EO material when phase matching condition is met [31]:

$$K_{out} \mathrm{Sin}\,\theta_{out} = K_{EO} + m\frac{2\pi}{\Lambda} \qquad (2.2)$$

where:

K_{out} : Wave-vector of the outgoing light with incidence angle θ_{out}

K_{EO} : Wave-vector of Electro-optic polymer film

Λ : Period of the grating structure and

m : An integer that defines the order of the scattering process.

$K_{EO} = \frac{2N_e\pi}{\lambda}$, where λ is wavelength of applied wave and $K_{out} = \frac{2\pi}{\lambda}$

The exit angle of coupled beam is going to be dependent on the refractive index of the EO material, thus it can also be tuned by applying different voltages across the EO polymer. The grating period can be determined from (2.2) for a desired exit angle. The entire device can be fabricated using conventional micromachining and lithography method, which is highly robust and repeatable. Combining the horizontal scanning from the prism stage and the vertical scanning of the grating stage, 2D scanning can be achieved and the results of the EO scanner is shown in Figure 2.8.

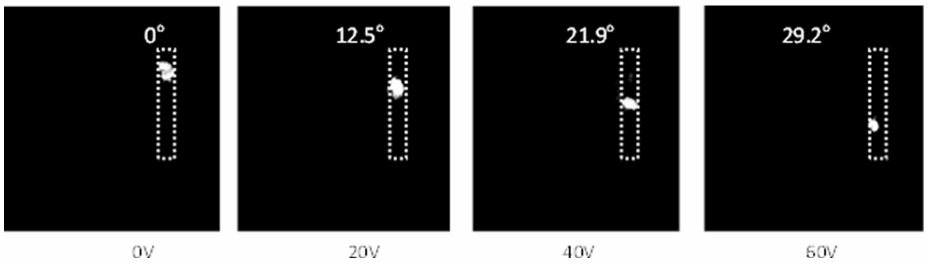

(a)

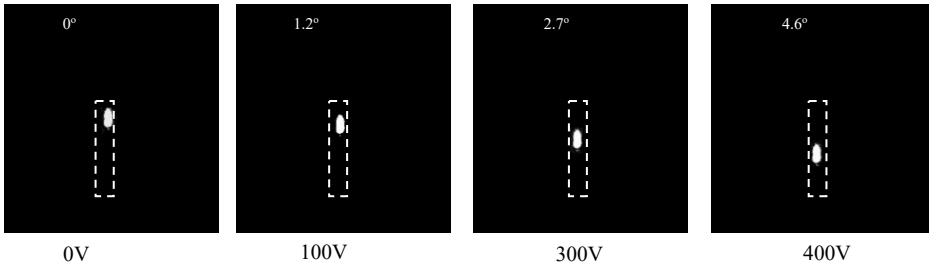

(b)

Figure 2.8. (a) Beam Output from the Prism Stage for various applied voltages (b) Beam Output from the Grating Stage for various applied voltages.

2.2.2 *Out-of-Plane Beam Steering using Electrode-Grating*

The footprint of the device can be further compacted by replacing the polymer grating coupler with a grating patterned into the top electrode. The metal grating electrode functions both as an output coupler and an electrode for applying voltage to drive the EO material layer. The E-Field distribution for the electrode grating design is simulated using FEA and the result is shown in Figure 2.9, it can be seen that a uniform electric field can be created a cross the EO material layer.

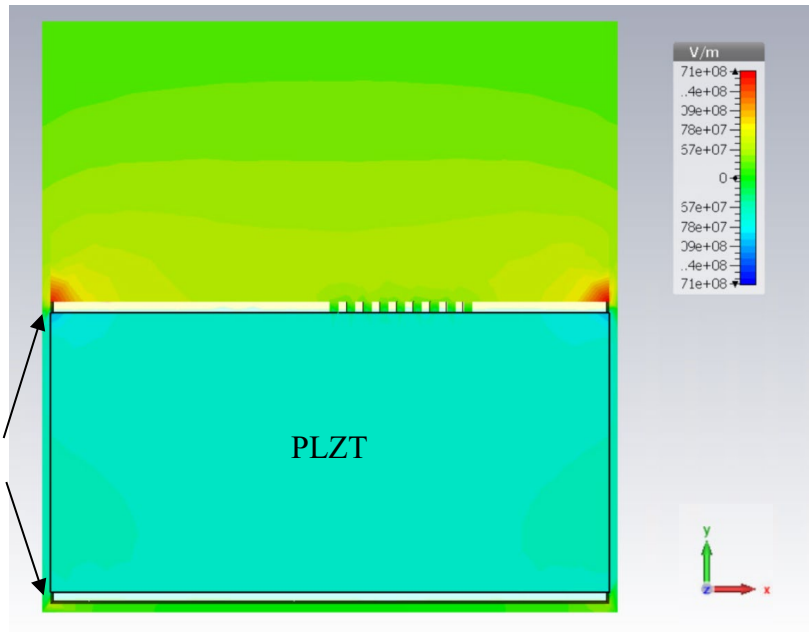

Figure 2.9. Electric Field under Electrode Grating Pattern

To allow the device to operate in visible spectrum within minimal loss and higher efficiency, transparent electro-optic ceramic materials such as PLZT (lead lanthanum zirconium titanate) and PMN-PT are used instead of the EO polymer as the EO material layer.

PLZT and PMN-PT are usually found in electro-optic devices in bulk crystal form [33]. They have relatively high electro-optic coefficient, fast response rate, and it is availability in large quantities [34][35]. Their relative high index and broadband transparency also makes them an excellent candidate as an optical waveguide. To reduce the high voltage requirement of the bulk crystal,

thin-film PLZT and PMN-PT are used instead. Thin-film PLZT can be grown using solid-phase epitaxy, sol-gel method, and sputtering, which are all compatible with existing micromachining process. The resulting thin-films have comparable electro-optic coefficient [36] and it can be fabricated into different EO devices via the specific design of electrode geometries, such as the prism deflector arrays shown in [37]. Thin-film PMN-PT can be grown on quartz using pulse laser deposition [38]. It also displays relatively high linear EO coefficient in the visible spectrum [39][40]. These thin-film are also commercially available [41][42], which simplifies the fabrication process of the device.

A preliminary study is performed to test out the functionality of the electro-grating design with the proposed EO materials. Based on the properties of the proposed materials, a FDTD analysis is performed using the CST Microwave Studio software. The optimal period of the electro-grating is obtained from a parametric study of grating period and applied voltage based on (2.1) and (2.2). It can be observed from Figure 2.10b that the deflection angle is maximized by the maximizing both the parameters. However, for the purpose of out-of-plane coupling, exit angles between 30°-50° is desired. Thus, a grating period of 300nm is selected for the simulation for the output angle of 30° from the vertical axis (y-axis in Figure 2.9) according to Figure 2.10a. The simulation model is shown in Figure 2.11 and the beam coupling of the inactive device is shown in Figure 2.12. It can be observed that the electrode grating is able to deflect the beam out of the EO material with a correctly designed grating period. The simulated exit angle (31°) matches closely with the exit angle predicted by the phase matching condition. Additionally, the output angle can be tuned by changing the refractive index of the EO layer according to the E-Field from Figure 2.9 as shown in Figure 2.13. The device is capable of producing a deflection of 3° from the

applied voltage of 300V, which shows that the electro-grating will have similar performance compared to the polymer grating in the previous design.

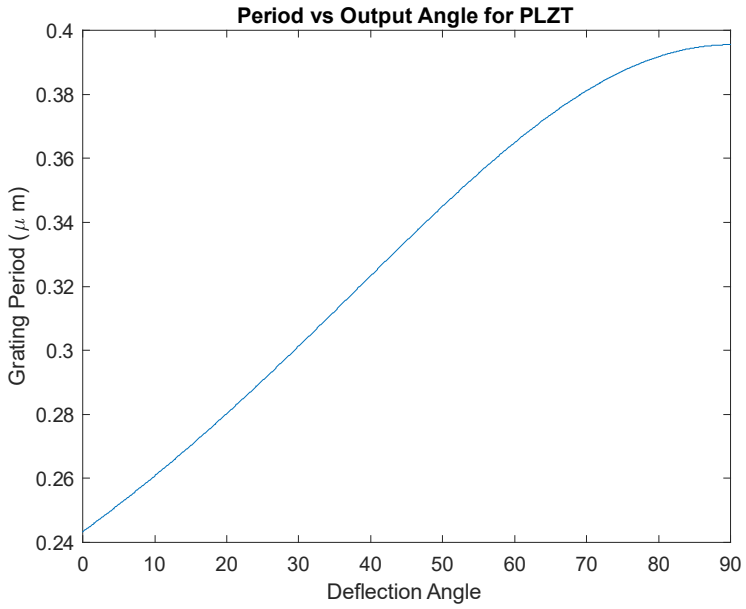

(a)

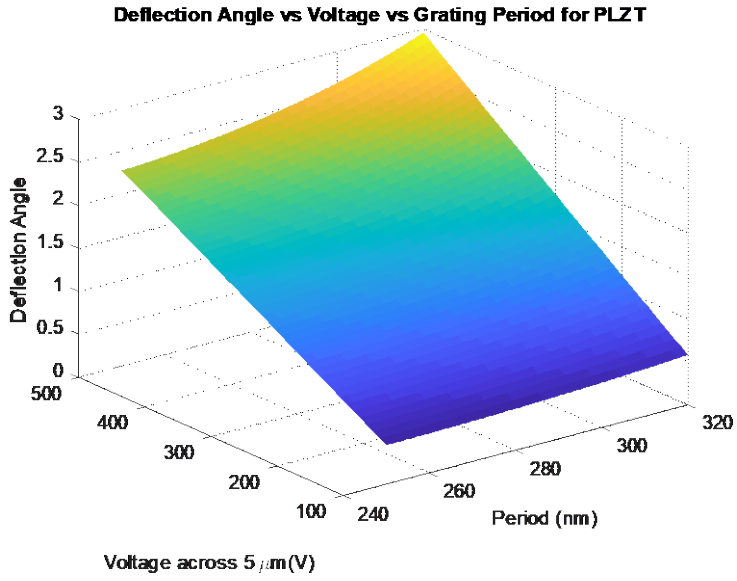

(b)

Figure 2.10. (a) Grating Period vs Output Angle for Electrode Grating over PLZT Waveguide and (b) Deflection Angle vs Voltage vs Grating Period for Electrode Grating over PLZT waveguide

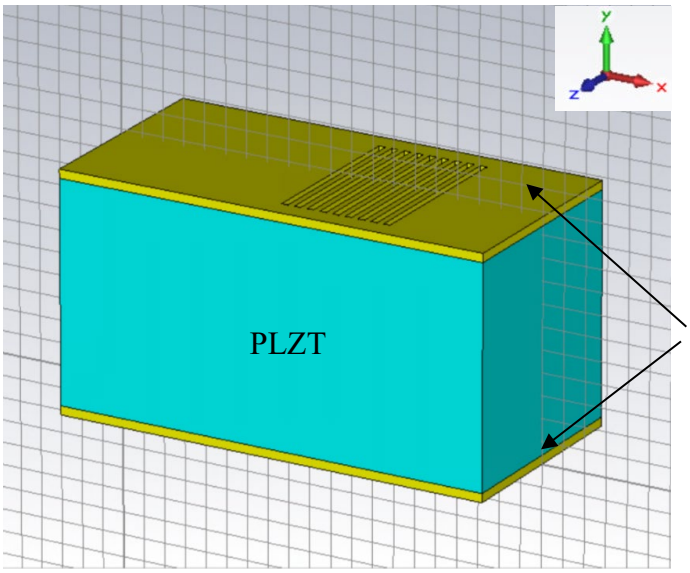

Figure 2.11. Electrode Grating Deflector Simulation Model

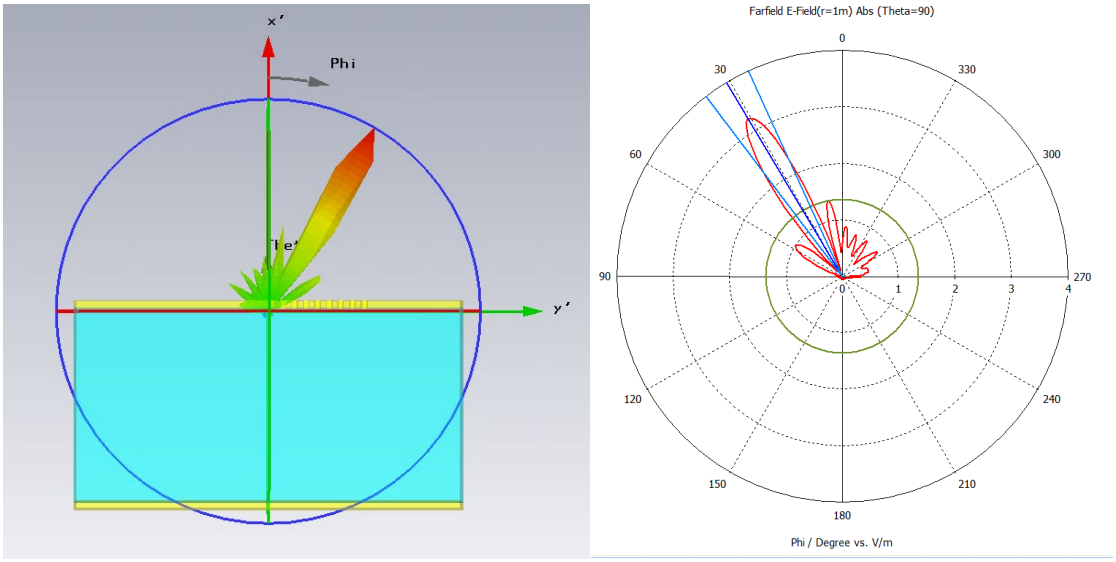

Figure 2.12. Output Coupling Results of the Electrode Grating Pattern (Farfield 3D & Polar)

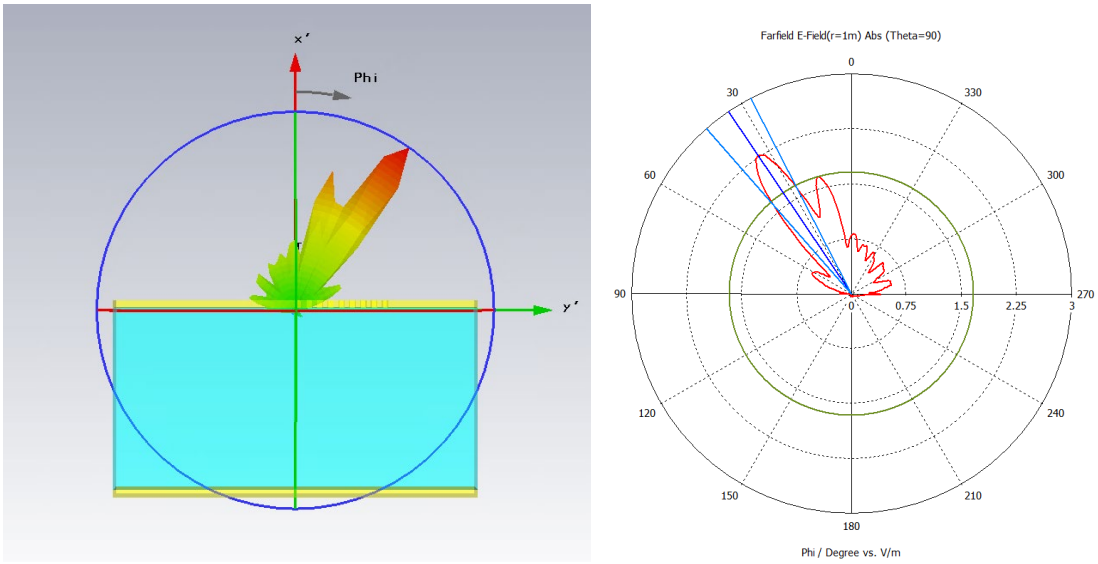

Figure 2.13. Beam Deflection Results due to refractive index change (Farfield 3D & Polar)

Despite successful deflection, it can be observed that the grating pattern of the electrode-grating creates unwanted side lobes in the farfield radiation pattern due to output beam passing through the grating slit pattern geometry, which forms an interference pattern. Thus, the output beam profile needs to be corrected by adjusting the grating geometry or additional optics. Additionally, the operation of the device requires high voltage, thus consuming higher power during operation.

Chapter 3. METHODS

3.1 DESIGN THEORY

The multi-stage EO scanner described in Chapter 2 is able to achieve 2D scanning without the shortcomings of mechanical systems, however, it is not without its own disadvantages. The EO scanner design relies on the precise alignment of the stages, it is not robust against any misalignment in the assembly process and material defects since the geometries are permanently formed on the substrate. These problems can be potentially solved by adding additional optics or stages, however, that will in turn increase the overall system size. The device performance is also somewhat limited by the size of each of the stage, as there needs to be sufficient space for the beam to travel within the system to create sufficiently large deflection angles. To solve these problems, an adaptive device that is able to provide large deflection without requiring large footprint structures based on tunable metamaterial is developed.

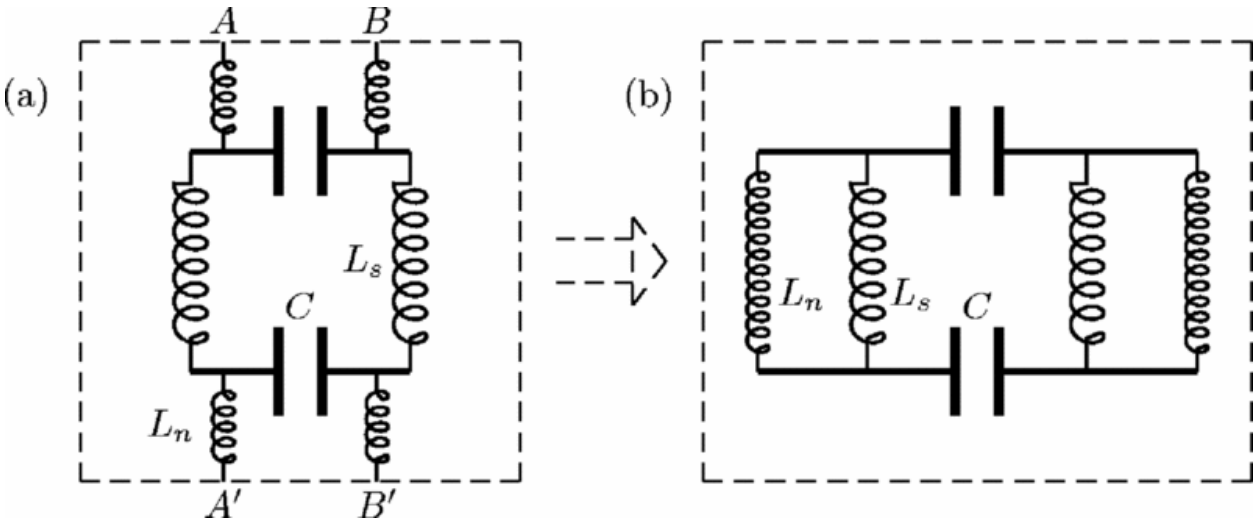

Figure 3.1. Fishnet metamaterial equivalent circuit.

Metamaterials are periodic metal nano-structure designed to drastically modulating the phase of an incident wave near the resonance frequency of the structure. The resonance frequency of the

structure is determined by the geometry of periodic nano structure. In the case of fishnet metamaterials, each metal nano-structure unit cell can be modeled as equivalent LC circuit [43] (Figure 3.1) according to its magnetic resonance:

$$\omega_m^2 = \frac{1}{LC} \tag{3.1}$$

The inductance term L is mainly contributed by the oscillation of current on continuous metal geometry on the cell and the capacitance term C is mainly contributed by gaps between the metal geometry and the space between each layer. To create the change in refractive index in each cell, the resonance peak is shifted by tuning either the effective inductance and capacitance. Since the metal geometry in the design is permanent after manufacturing, it would be difficult to change the inductance term in (3.1). However, the capacitance term in the equation is adjustable. The capacitance between the two electrodes can be modelled as a parallel plate capacitor (3.2):

$$C = \epsilon_r \epsilon_0 A/d \tag{3.2}$$

where ϵ is the permittivity of the dielectric material between the 2 layers, A is the area of the plates, and d is the gap distance between the plates. The A and d parameters are results of design and manufacturing; however, it is possible to tune the permittivity of the dielectric material layer if the material is electro-optic. As mentioned in the previous section, linear electro-optic material displays pockel's effect, in which the refractive index changes proportionally with an applied electric field. The permittivity of a non-magnetic material is related to the refractive index of the material as shown in (3.3)

$$\epsilon^* = n^{*2} = (n + i\kappa)^2 \tag{3.3}$$

where ϵ^* is the complex permittivity of the material, n^* is the complex refractive index, n is the real part of the refractive index and κ is the imaginary part of the refractive index. It can be

observed that permittivity of the material can be tuned by varying the refractive index of an electro-optic material.

In the proposed design, a modified double fishnet electrode design from [43] is used due to its potential as a low loss metamaterial for high frequency waves. The modified fishnet has an isotropic-like geometry that is capable of producing large refractive index change over a wide range of dimension parameters. The double fishnet electrode functions as a resonant structure the as well as the driving electrode for the electro-optic layer. The fishnet electrodes will be deposited on a flexible substrate and the dielectric layer will be sandwiched in between the electrodes and contained using a spacer for controlling its thickness. The cross-section view of the device structure is shown in Figure 3.2. The design of the electro-optic dielectric layer, the substrate, and the electrode geometry will be discussed in Section 3.2, Section 3.3, and Section 3.4, respectively.

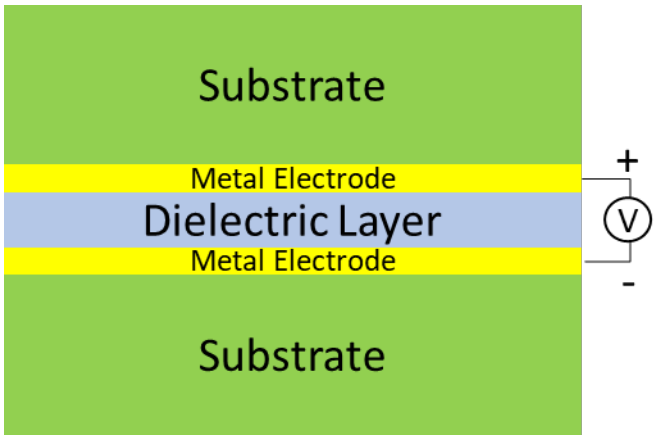

Figure 3.2 Cross-section view of the proposed device structure.

3.2 The Electro-optic Dielectric Layer

The electro-optic layer serves as the tunable component of the device. It will be based on electro-optic materials to allow the voltage tuning of its permittivity. The material needs to show good

performance and low loss for the operating wavelength and it needs to be able to be manufactured as a thin-film using methods compatible with micromachining process.

The characteristics of polymer based electro-optic materials make them a good candidate for the proposed design. They are usually found in high speed optical switches and their fabrication process is less specialized compared to thin-film ceramics. The two types of polymer based of EO materials that are considered are PDLC (Polymer Dispersed Liquid Crystal) and EO polymer with low absorption at the desired wavelengths.

EO Polymer is a polymer-chromophore mixture that will change in refractive index in the presence of an electric field. It is typically found in modulator and switches due to its high EO coefficient and its high response speed. EO polymer is synthesized by mixing a polymer with a chromophore that is compatible with the desired wavelength. After the EO polymer is synthesized, it can be patterned using the hot-embossing process and the structure is poled by applying a high voltage to pre-align the chromophores to enhance its electro-optic effect as shown in Chapter 2. EO polymers are typically used for THz generation such as THz emitters due to their high electro-optic performance in the infrared region. However, they do not provide similar electro-optic performance in the THz region that is necessary for the operation of our proposed device.

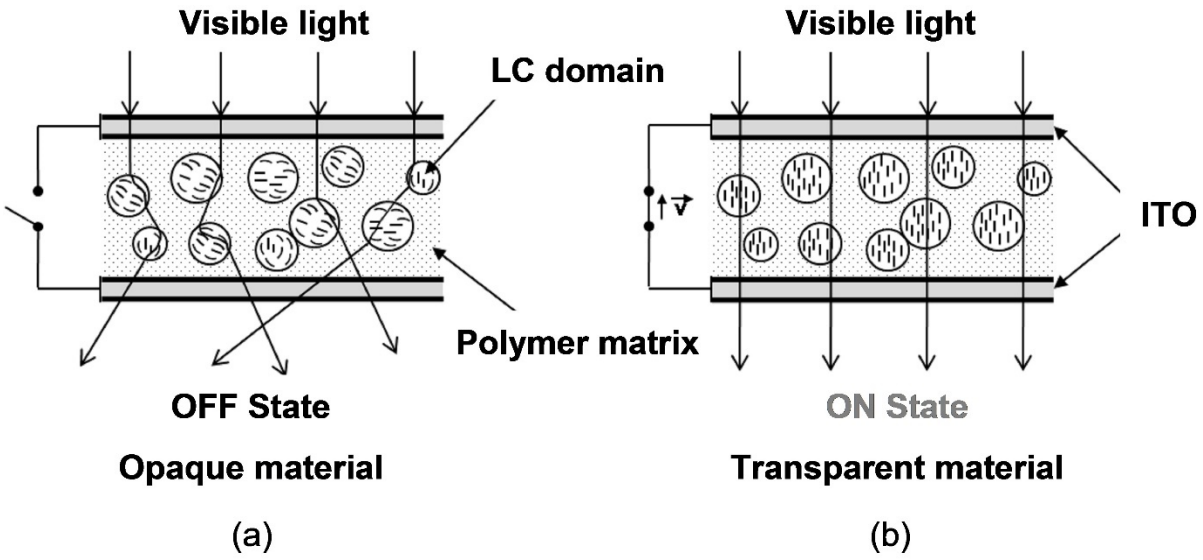

Figure 3.3. PDLC behavior during (a) OFF state (no voltage applied) and (b) ON state (voltage applied) [44]

PDLC (Polymer Dispersed Liquid Crystal) are liquid crystal droplet embedded inside a polymer matrix allowing LC to be encapsulated without an additional cell. The liquid crystal droplets are dispersed inside the polymer in random pattern until an electric field is applied across the PDLC to align the liquid crystals inside the droplet along the direction of the applied electric field (Figure 3.3). Within its operating voltage range, the gradual alignment of the liquid crystals inside the droplet causes the PDLC to become transparent (Figure 3.4), which is suitable for its typical usage in displays, and switchable windows [36]. Aside from transparency modulation, PDLC also displays a change in refractive index when an electric field is applied [46], which makes it a suitable dielectric layer for the proposed device. PDLC can be fabricated using photo polymerization process, which is highly repeatable.

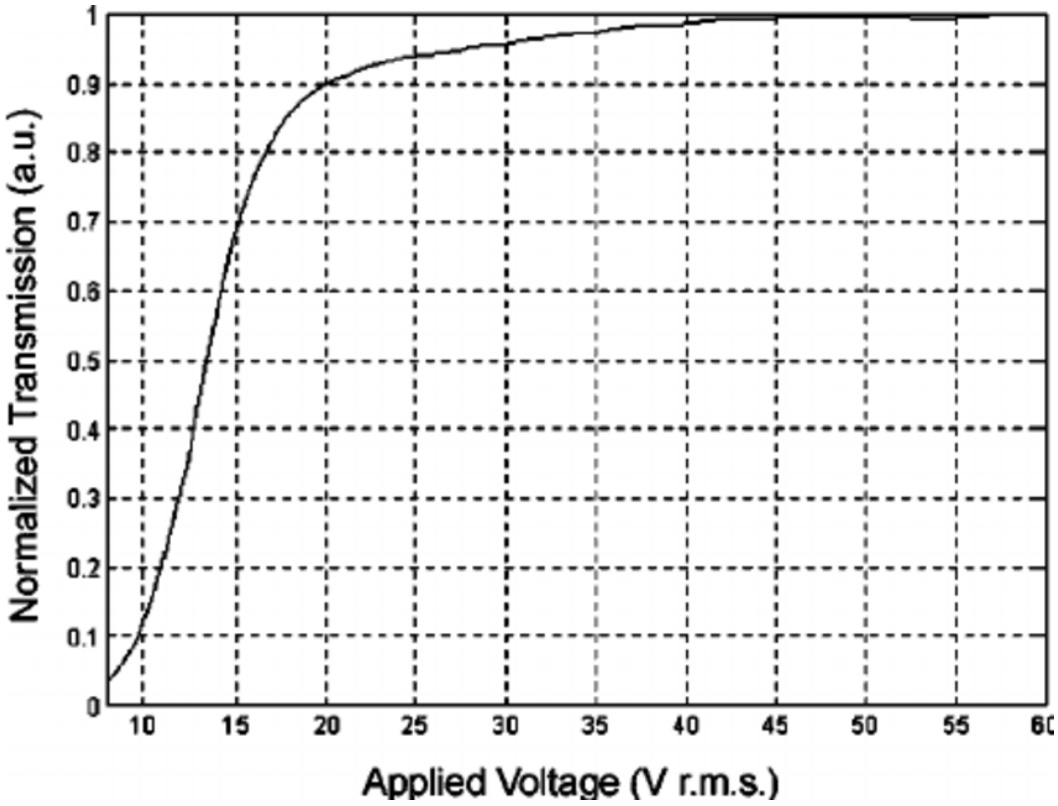

Figure 3.4. PDLC transmission vs voltage [47]

3.3 THE SUBSTRATE

For the proposed design, a flexible substrate is employed instead of a traditional hard substrate. The use of flexible substrate in our new design provided the following advantages: flexibility in integration, elimination of skin layer in the previous tunable fishnet design [20], reduced transmission loss compared to silicon substrate, and eliminated the Fabry-Parrot effect from the spectral measurements. Potential candidates for the substrates are polyimide (PI), Teflon, and Polyethylene terephthalate (PET). PET has a lower absorption loss compared to PI (Figure 3.5) but it has a higher absorption loss compared to Teflon [48]. Compared to Teflon, PET has a higher tensile modulus and lower coefficient of linear thermal expansion (CTE) (Figure 3.6), which

makes it less likely to wrinkle during our fabrication process. Thus, PET is chosen as the material for the substrate in our design.

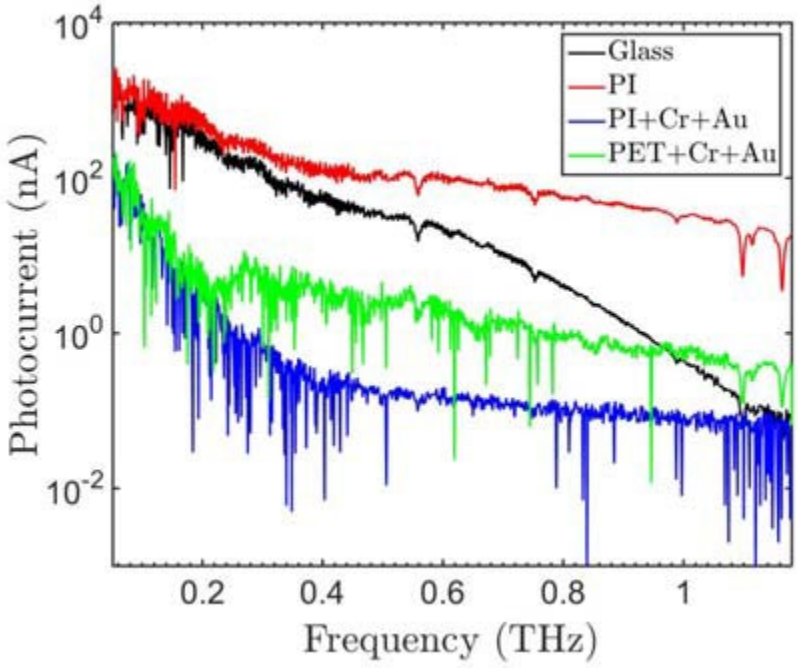

Figure 3.5. THz frequency domain transmission spectra of basic materials such as glass, PI, PI with solid unpatterned Au/Cr are shown here.

		Physical/Mechanical Properties				Electrical Properties		Thermal/Chemical Properties		
Substrate	Model/ Thickness	Density (g/cc)	Tensile Strength X-Direction at 23 °C (Kpsi)	Tensile Modulus X-Direction at 23 °C (Kpsi)	Dielectric Constants 100 Hz to 1 GHz	Dielectric Strength (V/mil)	Dissipation Factor Tan σ at 100 Hz to 1 GHz	CTE-15 °C to 300 °C (ppm/C)	Moisture Absorp-tion (%) at 23 °C	Shrinkage (%) 30 min, 150 °C
PET	Melinex 401 Polyester 70 µm	1.3	25	420	2.07	4000	0.002	19 to 20	0.1 to 0.7	0.5 to 1.1
PTFE	Teflon 100 µm	2.1	3.9	65	2.70	285	0.0002	250 to 275	0 to 0.05	1.5 to 3.0
PVC	Flexible PVC-O 110 µm	1.4	2.2	217	3.70	635	0.04	6 to 7	0.2 to 1	0.2 to 2

Figure 3.6. Mechanical Properties of PET and PTFE [49]

3.4 GEOMETRY OF THE ELECTRODE

The geometry of the metal electrode plays a critical part in the operation of the device because it directly impacts the magnetic resonance of the device, which is the region where the highest phase and refractive index change will occur as shown in [20] and simulations in Chapter 4. As shown in (3.1), the resonance of the device is dependent on the inductance and capacitance of the device. Shen et al has shown that the magnetic resonance frequency of the fishnet structure is related to the key geometric parameters of the fishnet structure. For the fishnet structure, the inductance of the neck and the slab are modeled as parallel inductors from the observation of current and electric field at its magnetic resonance, and (3.1) can be re-written in the following form [52]:

$$\omega_m^2 = \frac{1}{LC} = \frac{1}{L_{slab}C} + \frac{1}{L_{neck}C} \tag{3.4}$$

Here, L_{slab}, L_{neck}, and C can be described qualitatively using the geometric parameters of the fishnet structure [52]:

$$C \sim \frac{l_{slab}w_{slab}}{t}, L_{slab} \sim \frac{l_{slab}t}{w_{slab}}, L_{neck} \sim \frac{l_{neck}t}{w_{neck}} \tag{3.5}$$

where l_{slab} and w_{slab} are the length and the width of the slab, l_{neck} and w_{neck} are the length and the width of the neck or wires connecting the slabs and t is the thickness of the dielectric material. C is the capacitance that is generated by the pair of metal electrode (as described in (3.2)), L_{slab} and L_{neck} are the inductance contributions from the slab and the necks. And finally, the magnetic resonance frequency can be related to the geometry by substituting (3.5) into (3.4):

$$\omega_m \sim \sqrt{\frac{1}{l_{slab}^2} + \frac{1}{l_{neck}l_{slab}}\frac{w_{neck}}{w_{slab}}} \tag{3.6}$$

A preliminary study of various fishnet geometries is performed to investigate the effect of different geometries in: optimal frequency shifts, surface current accumulation, maximizing refractive index and phase changes, maintaining high Q factors, radiation coupling, polarization

independence and incident independence. Multiple shapes are investigated in the preliminary study and the results are summarized in [53]. It is discovered that the solid circle geometry is the most suitable design for our device due to its lower surface current density (Figure 3.7), which makes it less prone to high voltage breakdown during operation (Figure 3.8), and it has higher transmission coefficient compared to other geometries in the study.

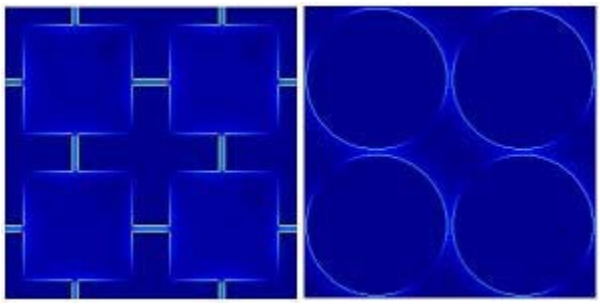

Figure 3.7. Surface currents induced on a square fishnet (left) and a circular aperture TFMM (right).

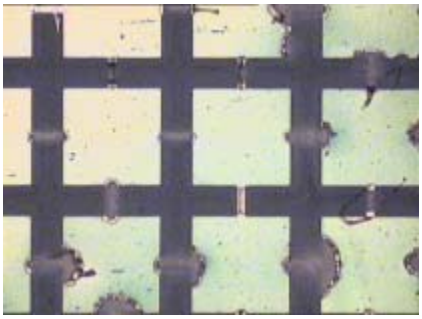

Figure 3.8. Device breakdown due to charge accumulation

Chapter 4. SIMULATIONS

4.1 PHASE INVESTIGATION

The performance of the device as a phase modulator is evaluated by investigating the phase change of the device. In this section, we will investigate our design's phase change performance under different boundary conditions.

4.1.1 *Simulation Model*

A simulation model is set up in CST Microwave Studio to calculate the S-Parameters of the design. The model is consisted of a dielectric layer, sandwiched by the two metal electrode layers and two substrates layer on the outermost of the device (Figure 3.2). As concluded from our preliminary geometry study, we will use a circular geometry for the slab of the electrode in place of the square fishnet geometry. The fishnet geometry is also modified such that each layer of the electrode is only connected in one direction (i.e.: top layer electrodes will be connected in x-direction, while the bottom layer electrode will be connected in the y-direction, Figure 4.1a). This will allow individual "cell" of the fishnet to be controlled discretely similar to a display matrix when different voltages are applied to the connected rows (or columns depending on the electrode layer)[54]. We will be using gold (Au) as the electrode for the device and it will be modeled as a lossy metal with electrical conductivity σ= 4.561e+007S/m and permeability μ=1. For the PDLC dielectric layer, it will be modeled as a composite material by calculating its effective dielectric constant and loss tangent using the methods proposed in [55]. At high frequencies, the model calculates the permittivity of the PDLC using a weighted sum of the permittivity of the polymer host (PMMA)[48] and the embedded liquid crystal (5CB) [56]. The PET substrate layer is modeled as a lossy dielectric layer using parameters from [48]. Unit cell

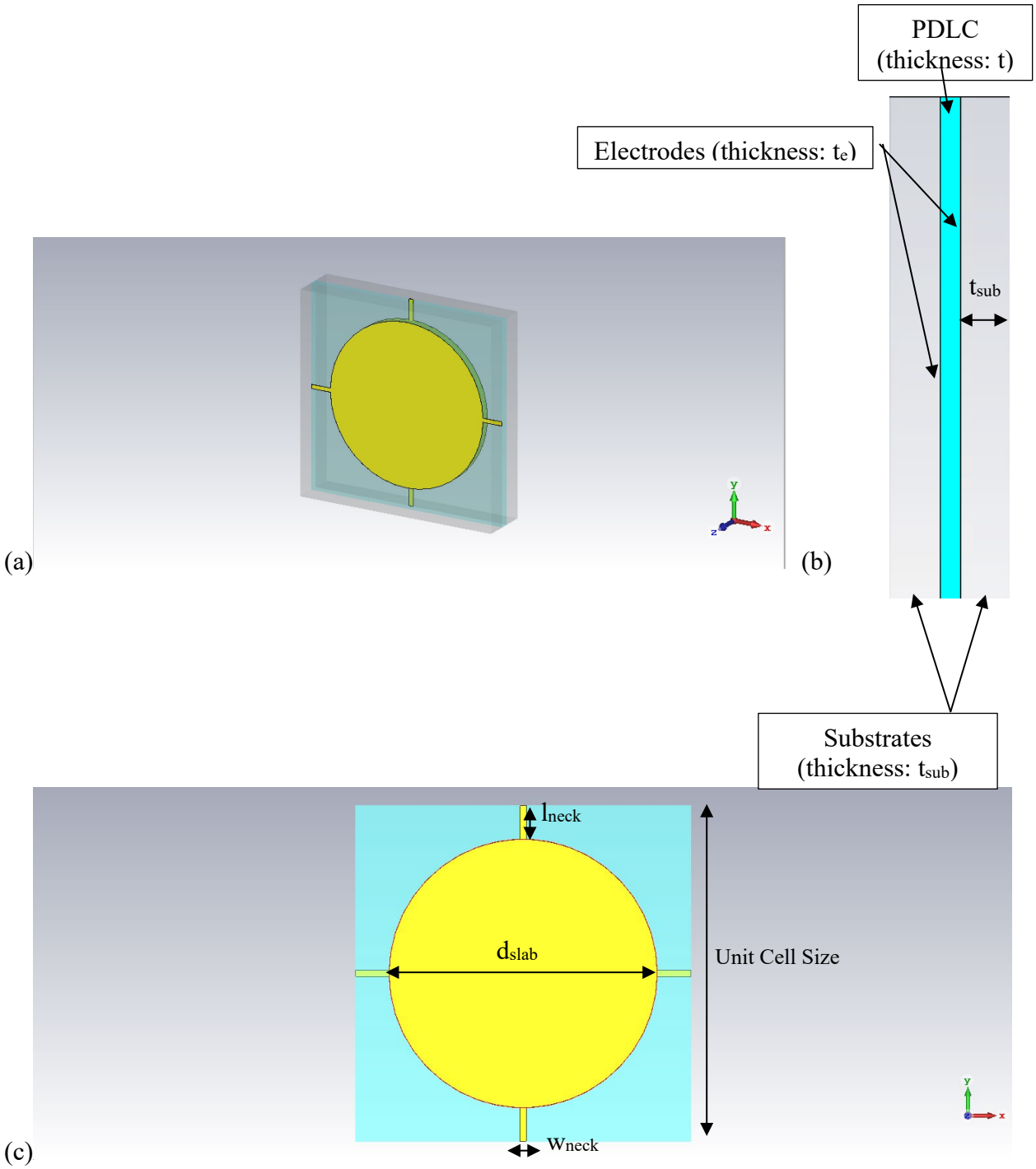

Figure 4.1. a) Isometric View, b) Side View, and c) Front View of the Meta-molecule of Proposed Design

boundary conditions will be used in the simulation to simulate an infinite sheet of the meta-molecule (shown in Figure 4.1) for extracting S-parameters, which includes the transmission phase

S_{21}. The simulation model will be excited by an electromagnetic wave that is polarized in the +x direction (coordinate indicated in Figure 4.1a) since it is observed in our previous studies [53] that higher gain is achieved at resonant frequency when the electric field is polarized parallel to the front electrode's connecting arm.

4.1.2 *Geometry Optimization*

The geometric parameters of the meta-molecule are optimized for the frequency range in which the PDLC on PET is showing the highest transmission response (0.2-0.4THz, Figure 4.2).

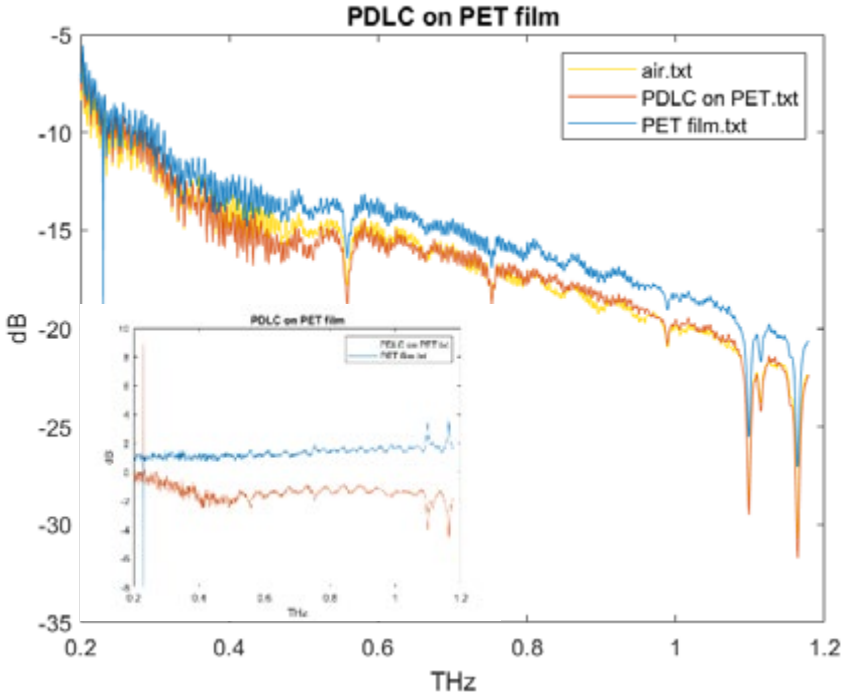

Figure 4.2. S_{21} responses of air, PET, PET with PDLC using Topica THz-TDS system. Small screen showing normalized responses.

The thickness of each layer is constrained by material availability and the fabrication process. The PET substrate layer will be 50µm thick (t_{sub}) in order for it to maintain flat and wrinkle-free during fabrication while keeping transmission loss at the minimum when the 200nm thick (t_e) electrode

is deposited on it. The PDLC dielectric layer will be 10µm thick (t) due to constraints imposed by the fabrication process.

For the electrode geometry, we started out with a 500µm x 500µm area unit cell so that it's compatible with the electrical interconnect that we will be using to control the voltage of the device. The increase in unit cell size compared to the previous designs will also allow us to reduce the resonance frequency, thus the operating frequency, by potentially increasing the size of the slab area in the electrodes, as discussed in Section 3.4. From our previous studies [20][53], the resonance frequency is characterized by a dip in the S_{21} magnitude. The optimization study is conducted by changing the diameter of the slab (d_{slab}) while keeping the unit cell size, wire width (w_{neck}) and thickness of each layer (t, t_e, and t_{sub}) constant.

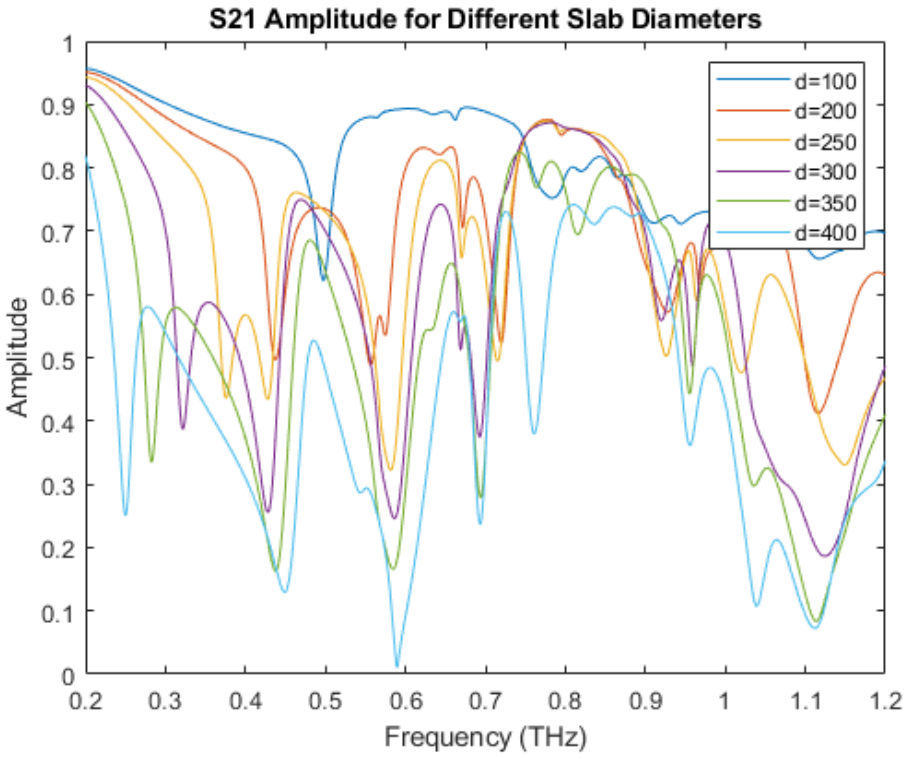

Figure 4.3. S_{21} Amplitude for different slab diameters

Figure 4.3 shows the S_{21} magnitude of the device with different diameters of the slab. It can be observed that as the slab diameter increases, the first resonant peak frequency decreases as predicted by (3.6). In the end, $d_{slab} = 400\mu m$ is chosen as our final design since it has the highest Q-factor in the region (labeled as Device 7 in the subsequent sections).

To further verify our design, we will need to evaluate the phase change effect when different voltage is applied to the PDLC layer. To simulate the effect of different applied voltages, the permittivity of the active dielectric area of the device (area below the slab of the electrodes) is changed correspondingly. For our evaluation purpose, we will compare the phase change between the OFF state and the ON state of the PDLC layer. For the OFF state, there will be no voltage applied to the device, thus there would be no change in permittivity in the PDLC layer. For the ON state, the permittivity of the active PDLC layer is changed by applying the maximum change in the liquid crystal refractive index in the composite material model for the PDLC. Figure 4.4 shows the permittivity for the PDLC layer for its OFF state and ON state, it can be observed that as voltage is applied to the PDLC layer, changing the refractive index of the liquid crystal droplet, the permittivity of PDLC decreases. Figure 4.5 shows the change in magnitudes of the S-Parameters across 0.2-0.9THz when a voltage is applied. It can be observed that the resonant frequency of the device increased due to the decrease in capacitance of the device when the permittivity of the PDLC is reduced due to applied voltage. This behavior agrees with the resonance frequency relation described by (3.4).

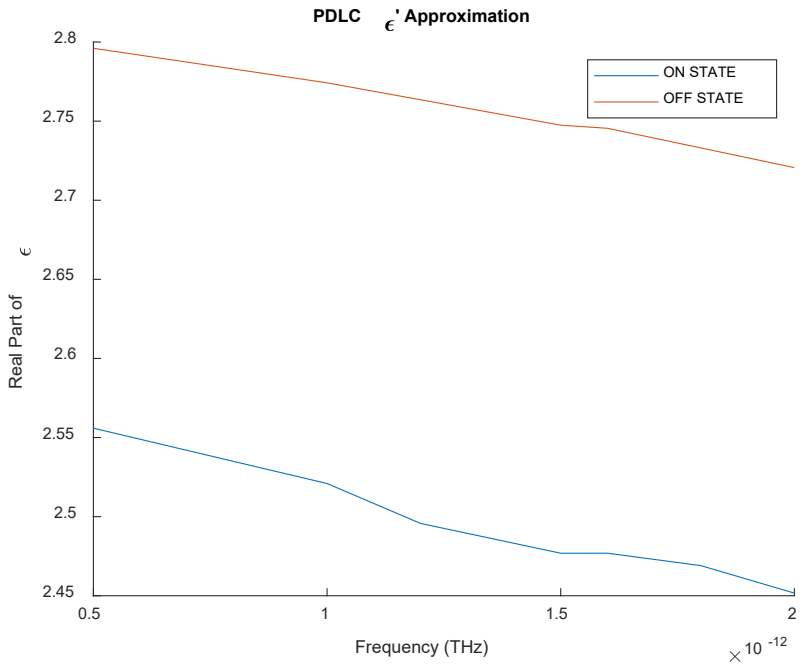

(a)

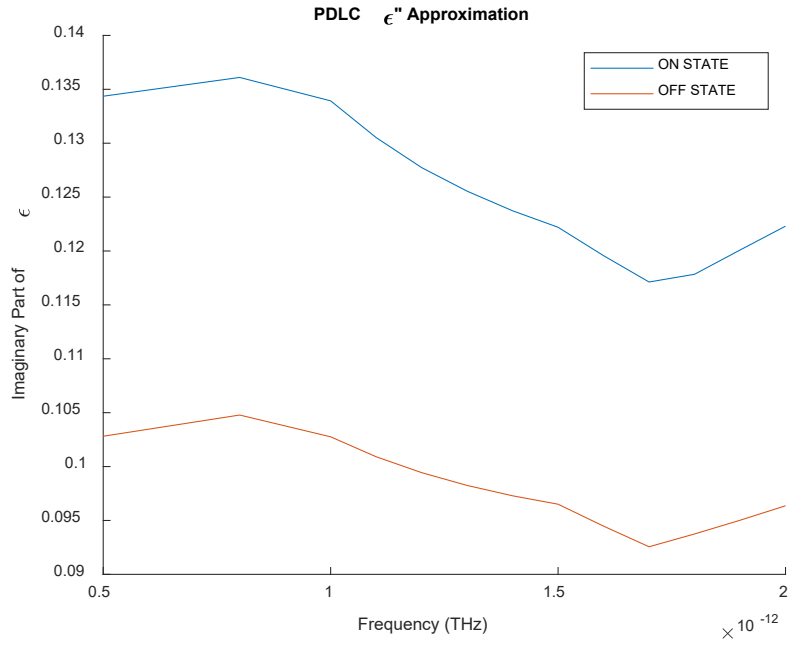

(b)

Figure 4.4. Real part and imaginary part of PDLC layer permittivity based on the composite model from [55]

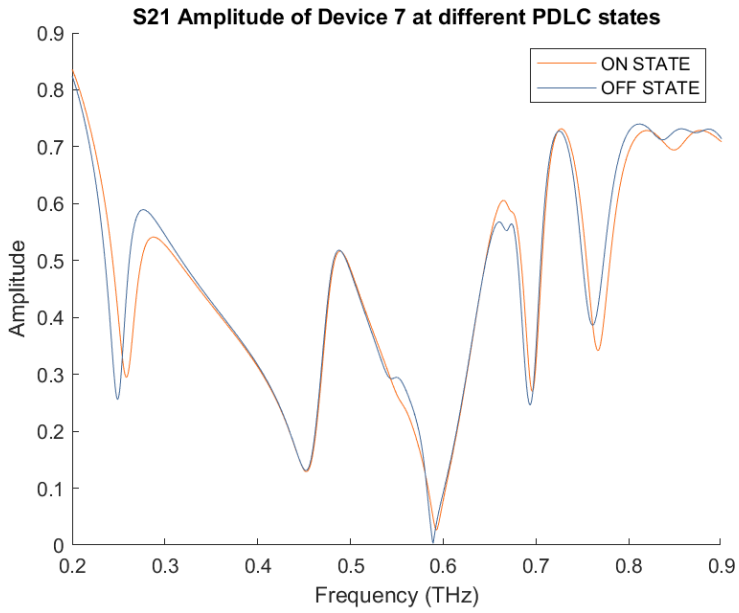

(a)

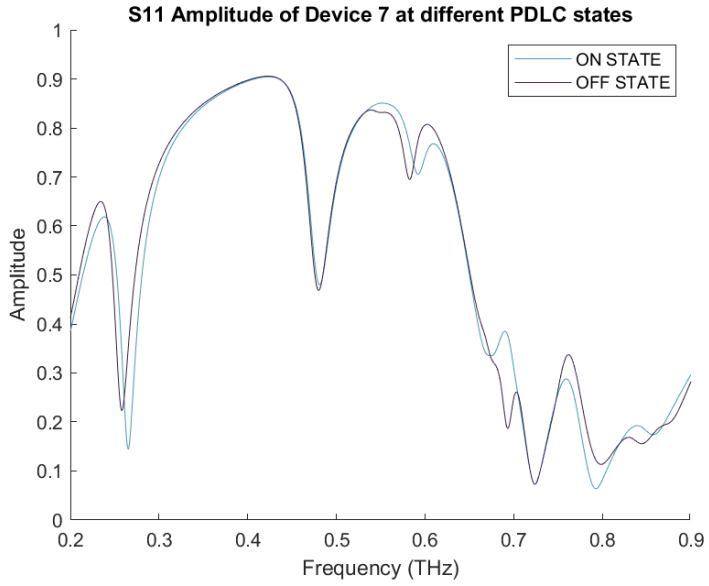

(b)

Figure 4.5. (a) S_{21} and (b) S_{11} Amplitude of the device for the ON and OFF state of PDLC

Figure 4.6 shows the comparison of the transmission phase of the device between the ON and OFF state of PDLC. The first peak phase change occurs at 0.2539THz, which occurs at near the first S_{21} dip. This phenomenon verifies the relation between the resonant frequencies and peak phase change, showing that resonance peaks are good indicators of where the peak phase changes

occur. It can be observed from Figure 4.6 that there is a much larger phase change peak at near 0.6THz, which is expected due to the existence of a larger S_{21} dip at near 0.6THz. However, 0.6THz is not an ideal operating frequency since the transmission in that region is close to 0 and the reflection in that region is much higher compared to that of the first peak at 0.2539THz.

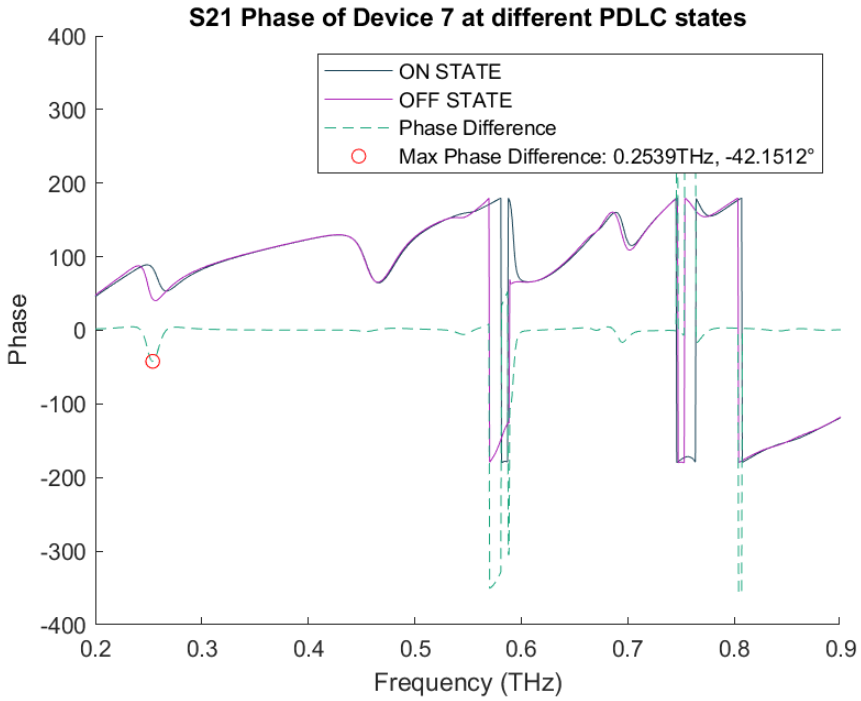

Figure 4.6. S_{21} Phase vs. Frequency comparison between ON and OFF states for Device 7

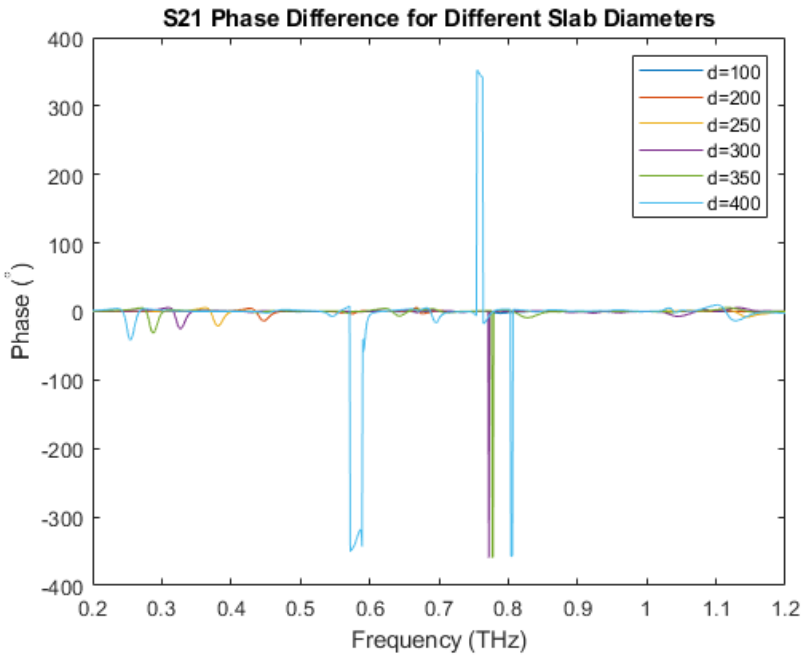

Figure 4.7. S_{21} Phase Difference between ON and OFF states for designs with different slab diameters

Figure 4.7 shows the results of the phase differences between ON and OFF states for designs with different slab diameters, and it can be observed that the d=400 design provides the highest phase change compares to the designs with smaller diameter slabs, showing that Q factor of the S_{21} dip correlates with the amount of phase change.

4.2 Refractive Index Investigation

The effective refractive index of the design is calculated in order to investigated the effectiveness of the design in enhancing refractive index change and verify the results from the phase change simulations. The following section describes how the effective refractive index is extracted S-parameter and compares the effective refractive index with the phase results from the previous section.

4.2.1 *Parameter Extraction via S-Parameters*

The effective refractive index of the device can be extracted from the S-parameters based on a method proposed by Chen [57], which is by solving the following equations:

$$S_{11} = R \tag{4.1}$$

$$S_{21} = Te^{jk_0 d} \tag{4.2}$$

$$Z = \pm\sqrt{\frac{(1+S_{11})^2 - S_{21}^2}{(1-S_{11})^2 - S_{21}^2}} \tag{4.3}$$

$$n = \frac{1}{k_0 d}\{\left[\mathrm{Im}\left[\ln\left(e^{ink_0 d}\right)\right] + 2m\pi\right] - j[\mathrm{Re}\left[\ln\left(e^{ink_0 d}\right)\right]] \tag{4.4}$$

where R is Reflectance, T is Transmittance, k_0 is the wavenumber in free space, d is the effective thickness of the device. Z is the complex impedance of the device, n is the complex refractive index of the device, and m is the branch index of the real part of n. Solving the equation using the relation between n and Z will allow the effective refractive index to be extracted. The ambiguity in n and Z can resolved by applying conditions for passive material and the correct selection of solution branches in (4.4) [57]. For calculating the refractive index in inhomogeneous resonators, it is necessary to set up reference planes in the simulation model to define the effective thickness (d) of the device due to a non-uniform scattering field produced by induced current on the metal electrode. The effect of non-uniform scattering field decreases at a certain distance away from the electrode, so reference planes for resonating inhomogeneous structures are typically beyond the device boundary. The reference plane can be properly determined by finding the distances beyond the metal electrode in which the impedance between single layer and multi-layer devices is minimized. For our current design, the electrode is embedded within a relatively thick PET substrate, thus the reference planes are set up at the device physical boundary in the simulation model (ie: effective thickness d = physical thickness of the device).

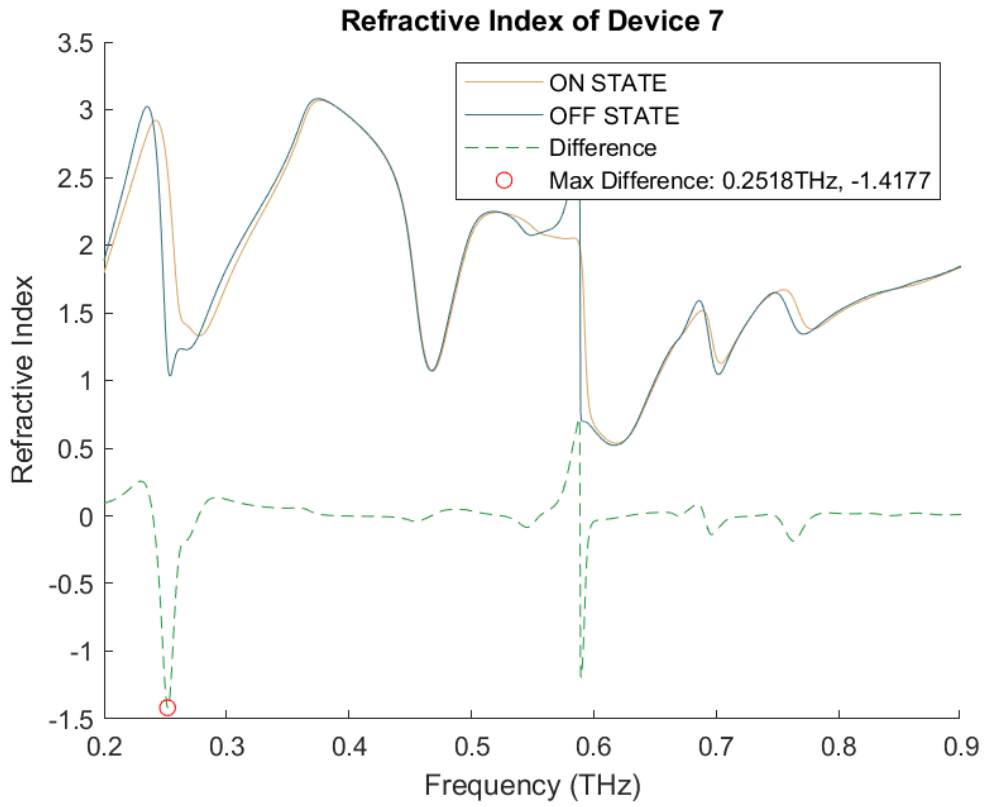

Figure 4.8. Refractive index change between the ON and OFF state of PDLC

Figure 4.8 compares the calculated refractive index of the device between the ON and OFF state of the PDLC. It can be observed that the largest change in refractive index occurs at 0.2518THz, with a change of 1.4177. This shows that the proposed design is capable of amplifying the small refractive index change from the PDLC ($\Delta n=0.2$) at the resonance frequency. Additionally, the frequency (0.2518THz) is close to where the device shows the highest phase change in our previous investigation (0.2539THz) under the same boundary conditions, which validates our method of obtaining the highest refractive index change via s-parameters.

4.2.2 *Refractive Index Using Geometric Analysis*

The refractive index result can also be verified using the geometric analysis method proposed in [58] to ensure that the ambiguity of the branch in the solution are solved correctly. Typically, the ambiguity in the branch solution is determined arbitrarily as found in the studied cases in [58] or using mathematical analysis methods with certain assumptions [59]. However, the physical implication of branch continuity and discontinuity has not been explored. By using a geometric analysis method, the refractive index of metamaterial resonators can be characterized and justified by observing their interaction with an electromagnetic wave under a certain geometrical configuration. The Device 7 meta-molecules at the OFF state are arranged in a prism geometry as shown in Figure 4.9 and the geometry is going to be excited by a +x polarized wave. The refractive index magnitude can be visualized by observing the deflection angle of the output wave at different frequencies: deflection angle to the +x direction indicates that the effective index is more positive, while deflection angle to the -x direction indicates that the effective refractive index is more negative. Figure 4.10 shows the results of the study from 0.2-0.27THz.

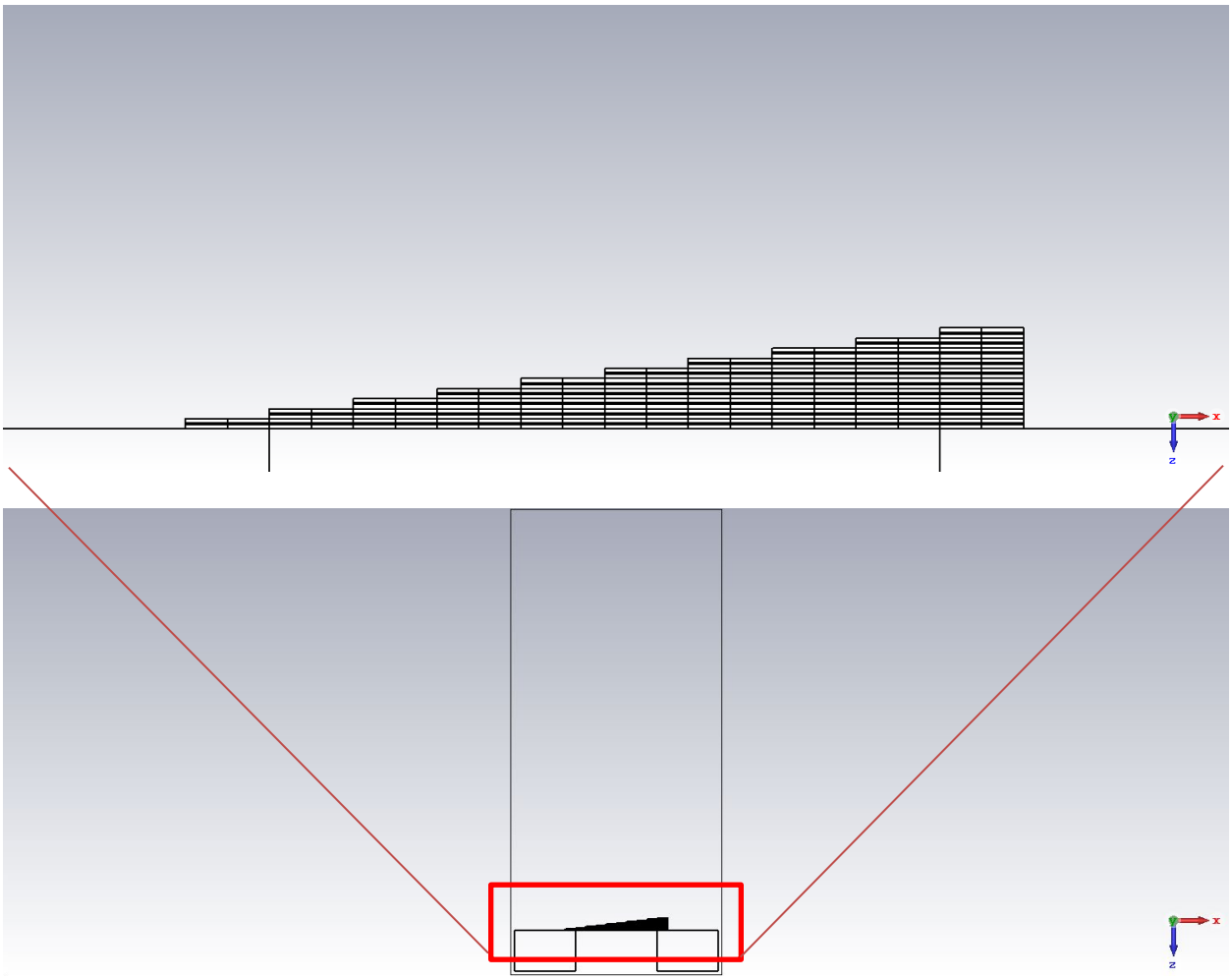

Figure 4.9. Prism simulation model for geometric study of refractive index. Top cross-section shown.

0.2THz

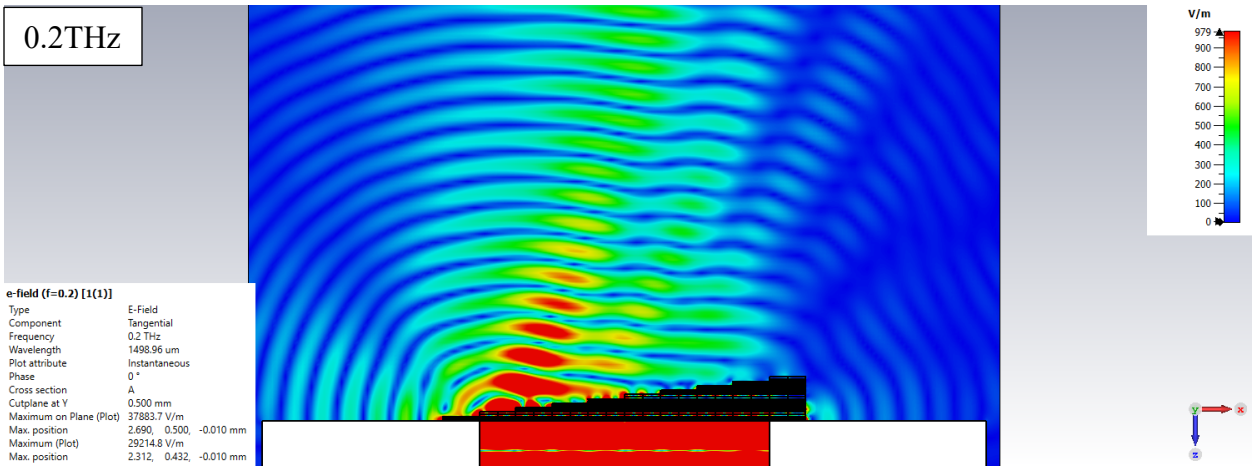

e-field (f=0.2) [1(1)]

Type	E-Field
Component	Tangential
Frequency	0.2 THz
Wavelength	1498.96 um
Plot attribute	Instantaneous
Phase	0 °
Cross section	A
Cutplane at Y	0.500 mm
Maximum on Plane (Plot)	37883.7 V/m
Max. position	2.690, 0.500, -0.010 mm
Maximum (Plot)	29214.8 V/m
Max. position	2.312, 0.432, -0.010 mm

0.22THz

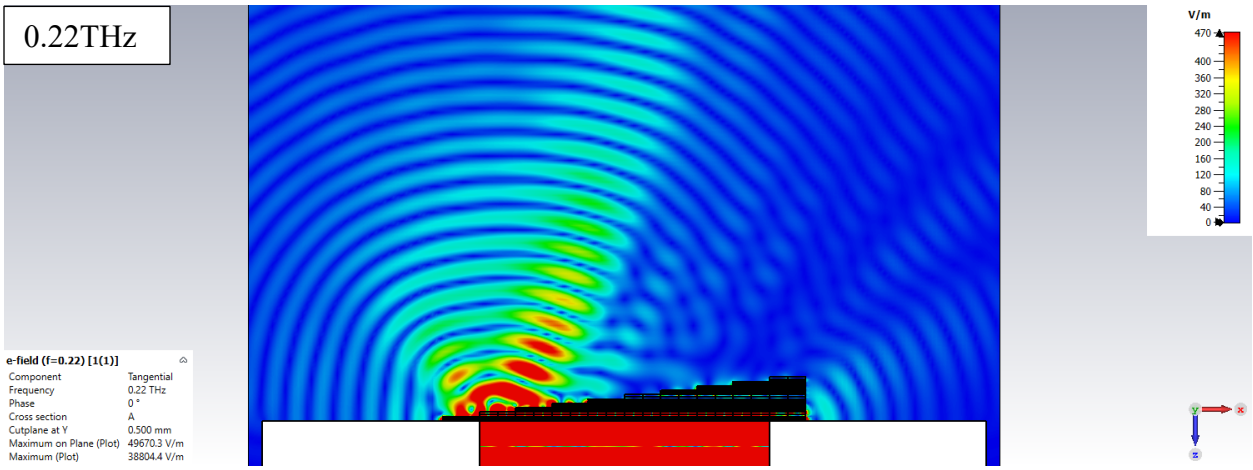

e-field (f=0.22) [1(1)]

Component	Tangential
Frequency	0.22 THz
Phase	0 °
Cross section	A
Cutplane at Y	0.500 mm
Maximum on Plane (Plot)	49670.3 V/m
Maximum (Plot)	38804.4 V/m

0.23THz

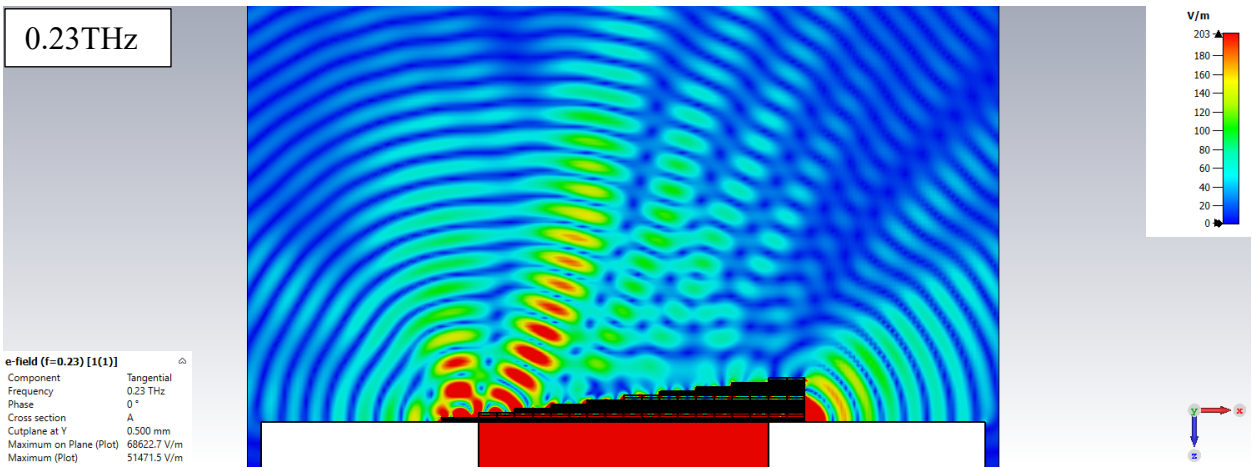

e-field (f=0.23) [1(1)]

Component	Tangential
Frequency	0.23 THz
Phase	0 °
Cross section	A
Cutplane at Y	0.500 mm
Maximum on Plane (Plot)	68622.7 V/m
Maximum (Plot)	51471.5 V/m

0.24THz

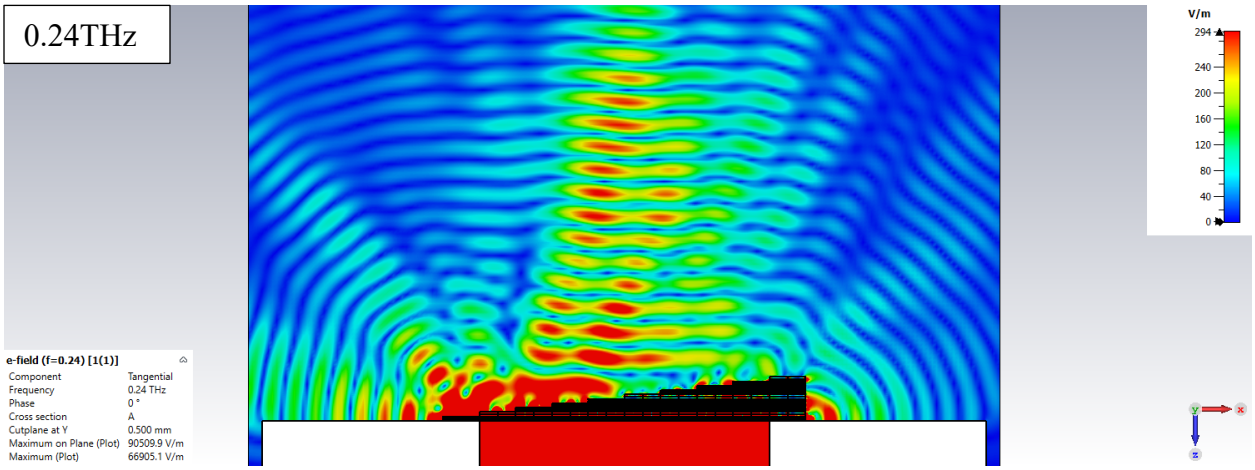

0.25THz

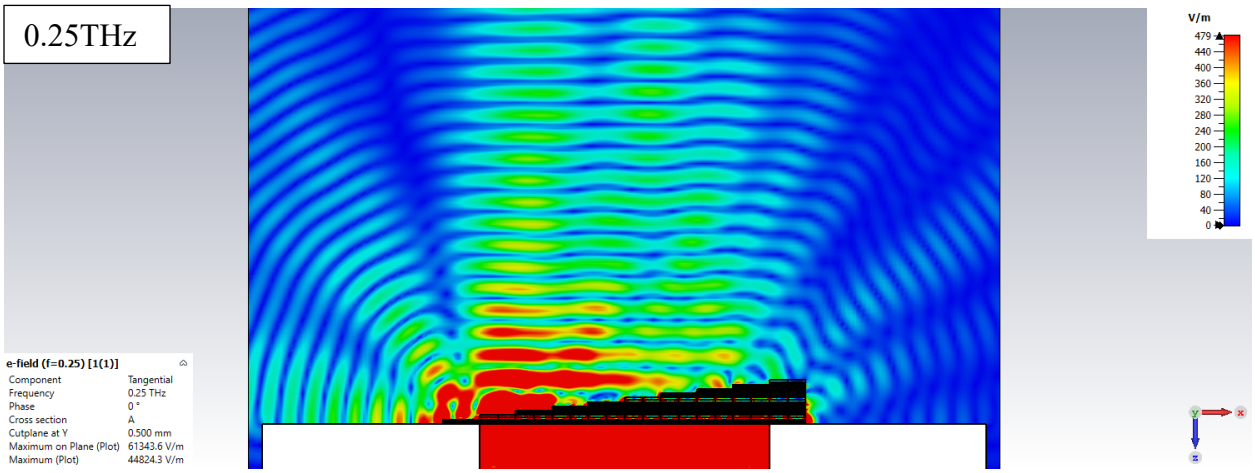

0.26THz

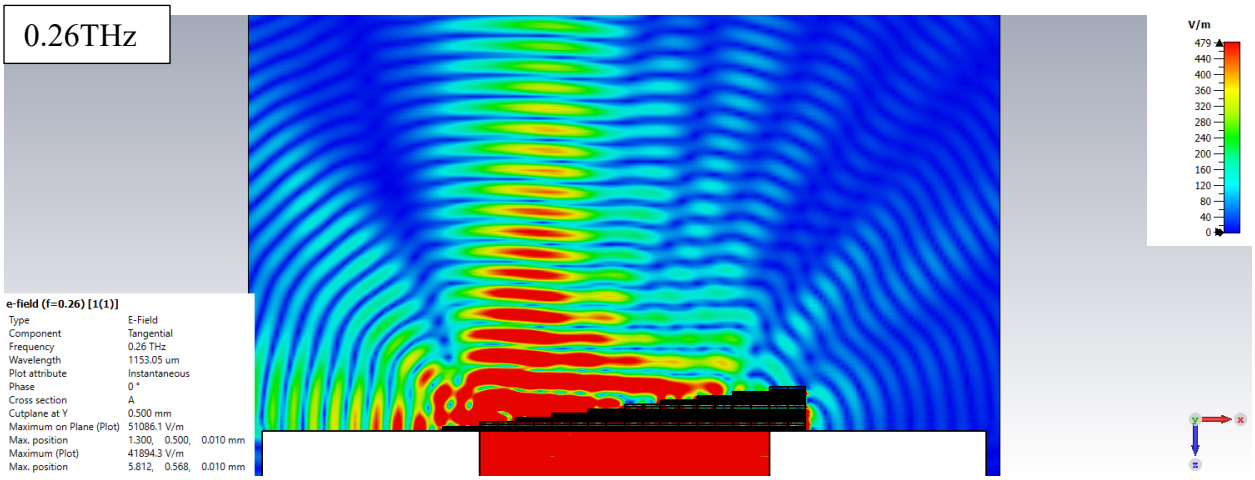

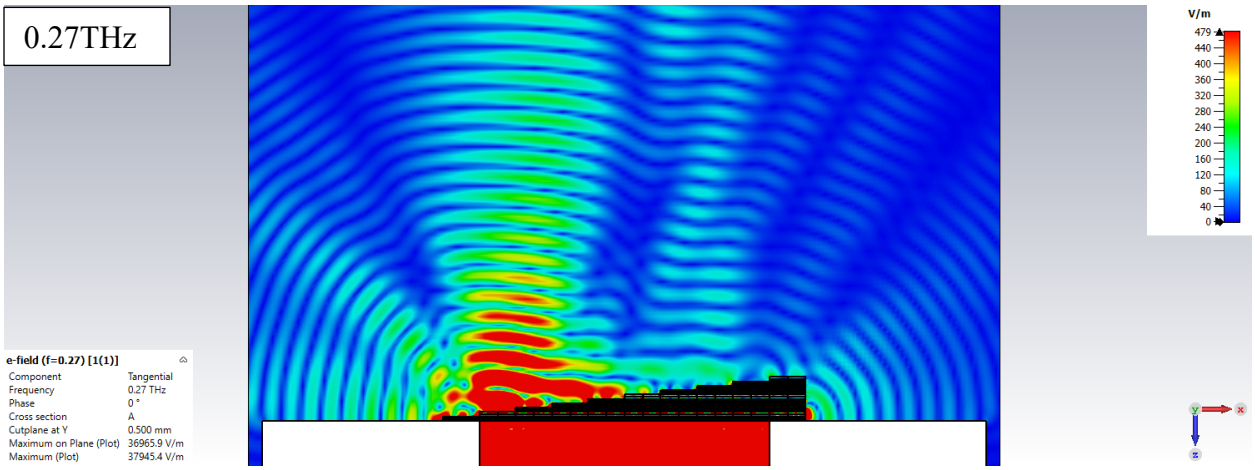

Figure 4.10. Prism geometric study results of Device 7 from 0.2-0.27THz

At 0.2THz, the refractive index is predicted to be positive, thus the output wave is deflected towards the +x direction. As the frequency increases, the refractive index gets more positive until after 0.23THz, thus the output wave deflection is increasingly towards the +x direction. At 0.24THz, the refractive index is on a sharp decrease until after 0.25THz, thus the output wave deflection starts to bend less towards the +x direction. At 0.25THz, it can be observed that the output wave is deflected even further towards the -x direction compared to 0.2THz showing that it has a lower refractive index. The refractive index starts to increase after 0.25THz, thus for 0.26 and 0.27THz, the output wave deflects increasingly towards the +x direction. The geometric method verifies the refractive index characteristics for 0.2THz to 0.27THz, showing that the correct branch is selected for the solution of refractive index for this range. To fully characterize the refractive index of the device, it would require a finer scan step and also a way of quantifying the deflection and relate it to the magnitude of the refractive index. It would also require further optimization of the prism geometry that is used for the analysis, since the prism geometry is prone to errors contributed by the effect of having multi-layer metamaterial, which can introduce frequency shift and additional peaks in the refractive index spectrum.

4.3 Preliminary Beam Manipulation Study

To test the beam manipulation capability of the proposed design. A simulation model has been constructed by arranging the Device 7 meta-molecules in a 10x10 array configuration as shown in Figure 4.11. The device is excited by a +x polarization wave propagating in the -z direction. The boundaries for the simulation model are set to be open in all directions.

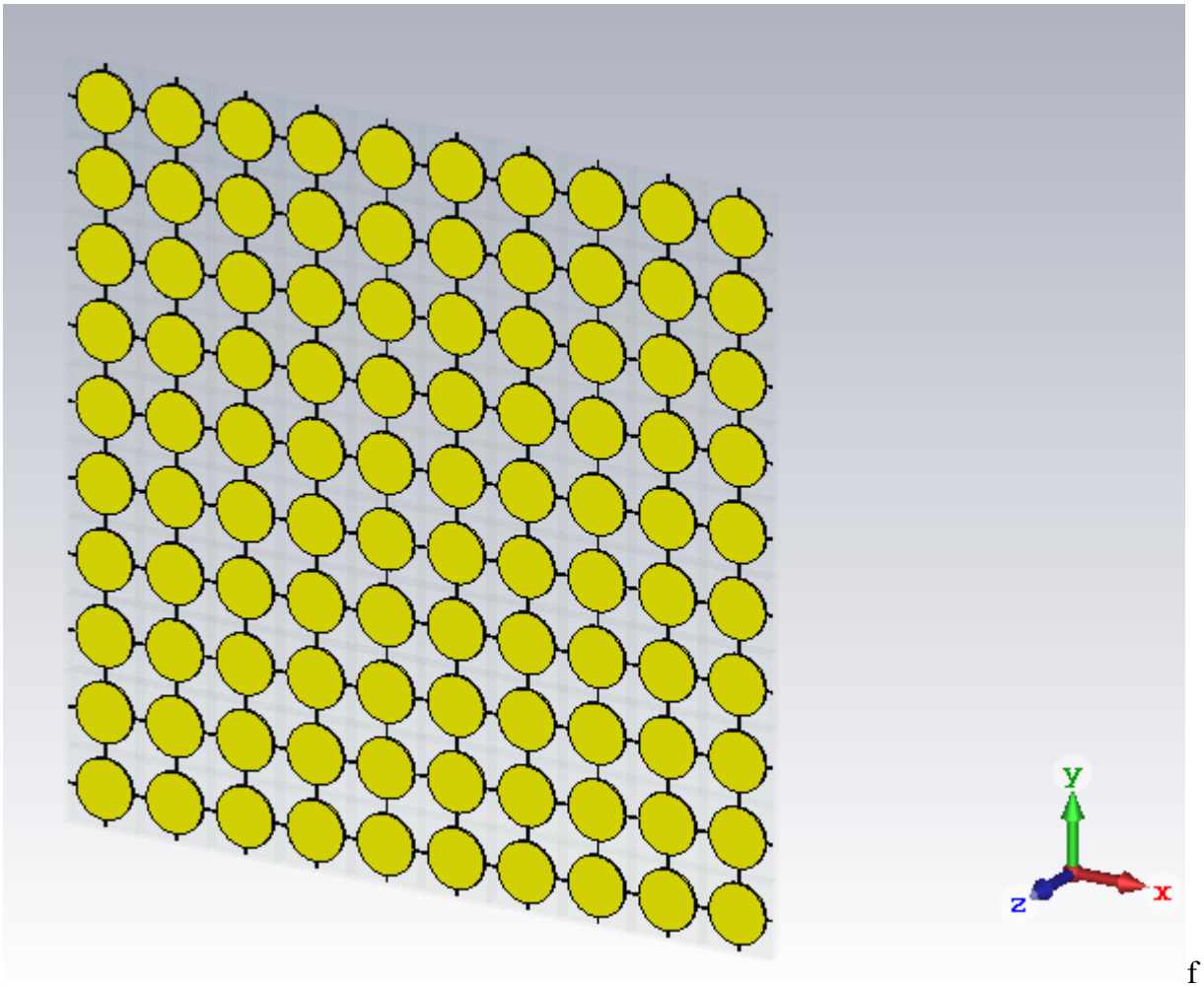

f

Figure 4.11. Top View of Device 7 array simulation model for beam manipulation study

Additional PDLC permittivity states between the OFF and ON state are calculated to allow the finer control of phase delay assignment in the simulation model. The permittivity of these additional states is calculated using interpolated values of the refractive index of the 5CB liquid

crystal between its n_e and n_o. The real part and the imaginary part of the 25 additional PDLC permittivity states between the OFF state (labeled as pdlc26) and ON state (relabeled as pdlc0) are shown in Figure 4.12. The phase delay of Device 7 for different PDLC states is then obtained by applying the corresponding states' permittivity to the active PDLC layer of 10x10 Device 7 array and calculating the S21 phase numerically under the same boundary conditions for the preliminary study. The phase between the OFF and ON state of the device is shown in Figure 4.13a and the phases for 10 different states at frequency where the maximum phase difference occurs are shown in Figure 4.13b. Here, phases with positive value means that it's leading the input phase, with a large positive number meaning that it has the least phase delay compared to the input. It is observed that the maximum phase change occurs at a different frequency (0.2474THz) compared to the previous study (0.2539THz), which is expected due to the change in boundary conditions. However, the frequency at which maximum phase change occurs is within 10% deviation meaning that the study method of our phase investigation is still a good indicator of where the maximum phase change occurs. It is also observed that the phase delay difference is increased by 30% compared to the phase investigation when the Device 7 design is simulated as a finite array. A preliminary test of the Device 7 array is performed by assigning the 10 states shown in Figure 4.13 into each column such that it forms a prism-like gradient profile as shown in Figure 4.14a.

Figure 4.15 shows the top view of electric field propagation for when no phase profile is applied to Device 7 (Figure 4.15a) and when the phase profile in Figure 4.14 is applied to the Device 7 array at 0.2474THz (Figure 4.15b). Additionally, the farfield radiation patterns of the different phase profiles are shown in Figure 4.16. Beam deflection towards to +x direction can be observed when a prism-like phase profile is applied, which agrees with the applied phase delay pattern as the phase delay increases towards the +x side of the. From the far field pattern, it can be

observed that the deflection angle is 1.4°. The relatively small deflection angle is expected since the maximum phase difference is less than 90°. However, from this preliminary study, it is shown that beam deflection can be achieved with an array arrangement of the Device 7 meta-molecules.

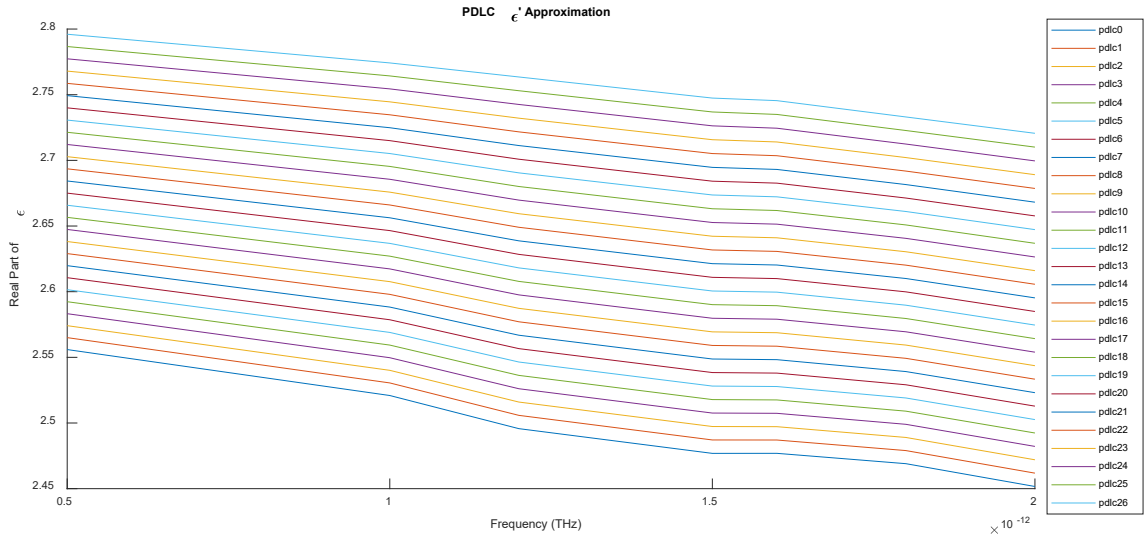

(a)

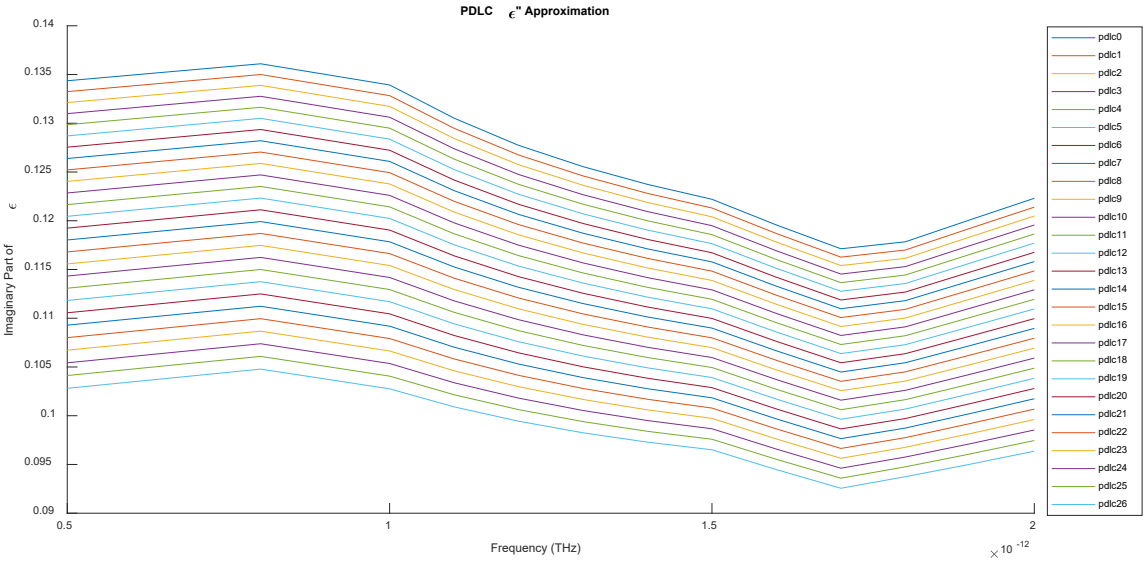

(b)

Figure 4.12. (a) Real part and (b) Imaginary part of permittivity for additional PDLC permittivity state between the OFF state (pdlc26) and ON state (pdlc0).

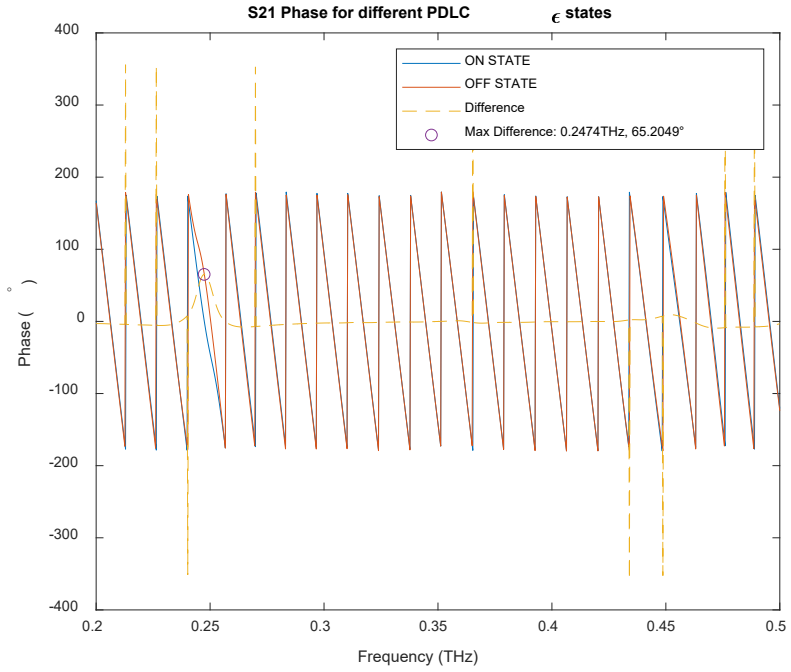

(a)

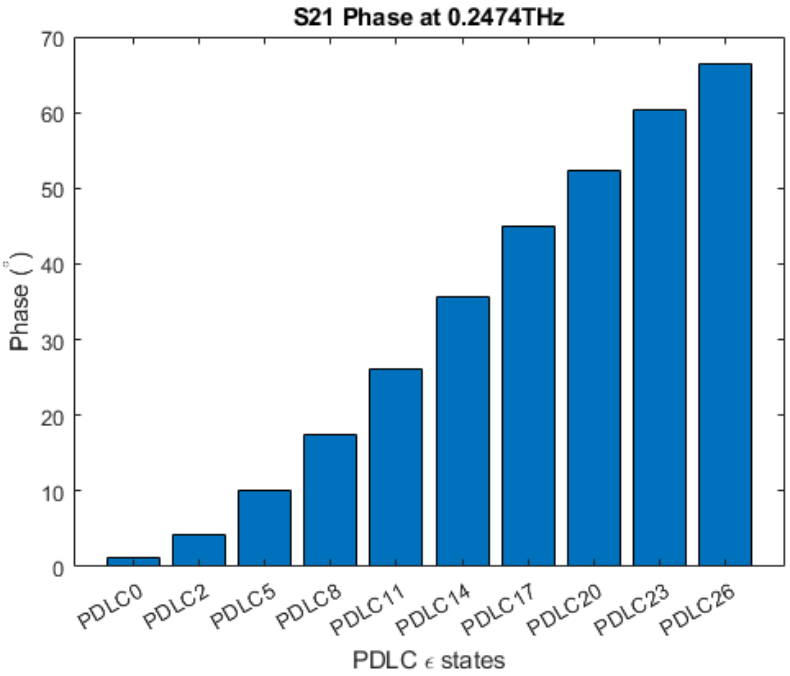

(b)

Figure 4.13. a) Comparison of phase delay of Device 7 array at OFF and ON states. b) Phase delay distribution of 10 permittivity states at 0.2474THz (Maximum phase delay frequency). Positive values shows phase lead.

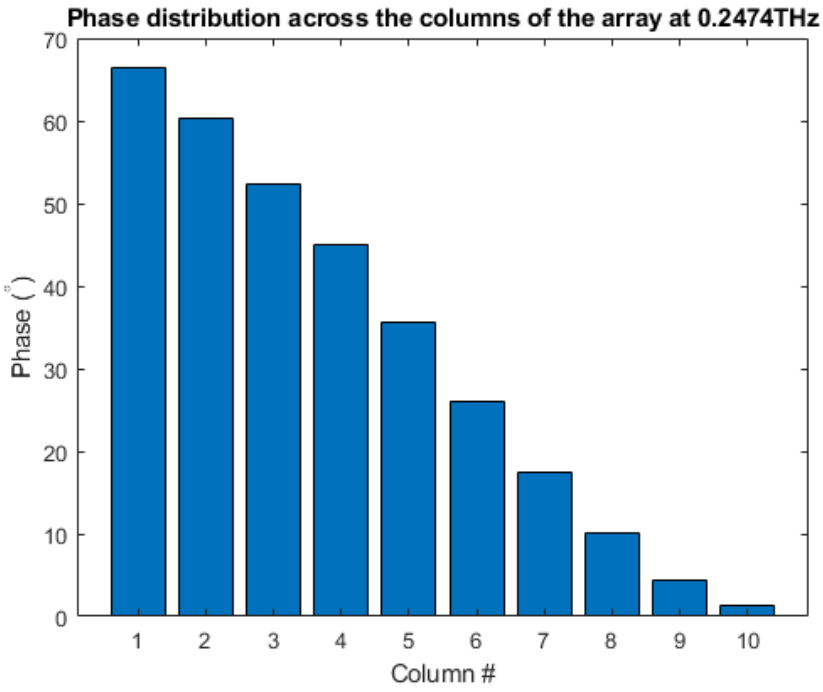
Phase distribution across the columns of the array at 0.2474THz
Phase (°)
Column #
0
10
20
30
40
50
60
70
1
2
3
4
5
6
7
8
9
10

(a)

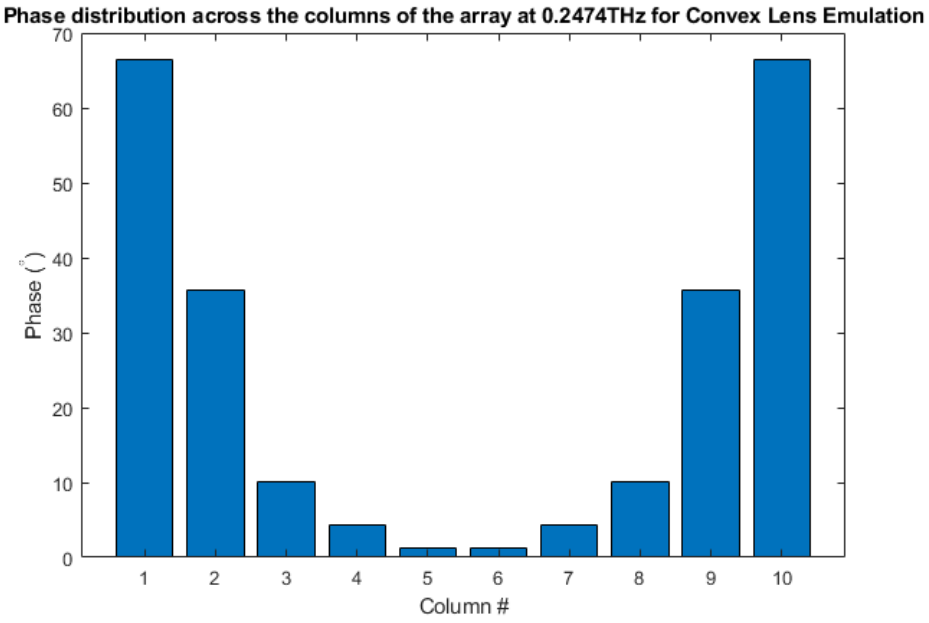
Phase distribution across the columns of the array at 0.2474THz for Convex Lens Emulation
Phase (°)
Column #
0
10
20
30
40
50
60
70
1
2
3
4
5
6
7
8
9
10

(b)

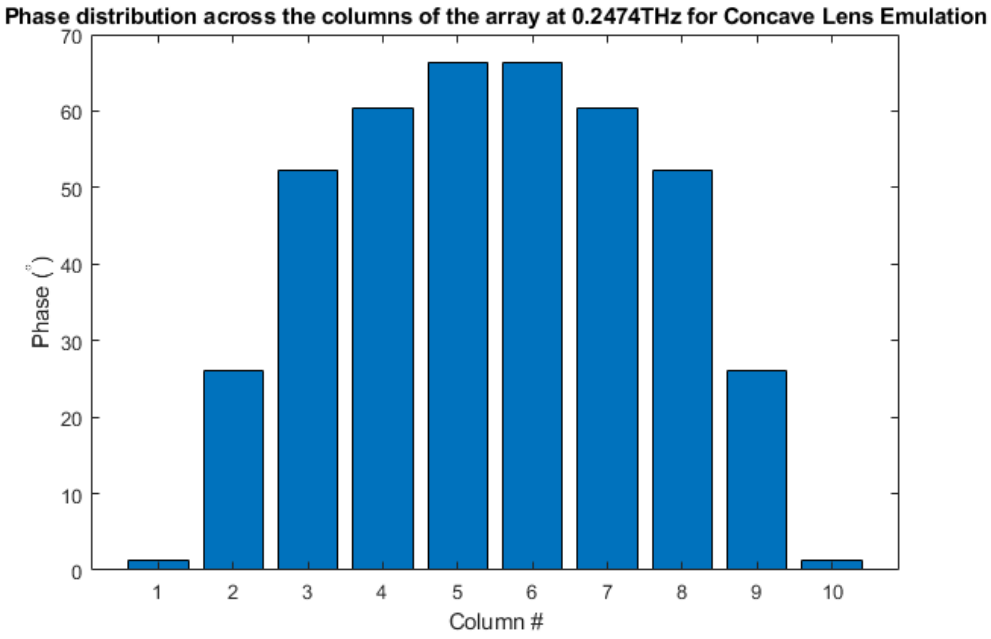

(c)

Figure 4.14. Phase profiles when different PDLC permittivity distribution is applied to the columns of Device 7 array model for preliminary study: a) prism-like phase distribution. b) convex lens emulation, and c) concave lens emulation.. Phases are based on phase results shown in Figure 4.13 obtained from the finite array simulation. Column number increases in the +x direction. Positive values shows phase lead.

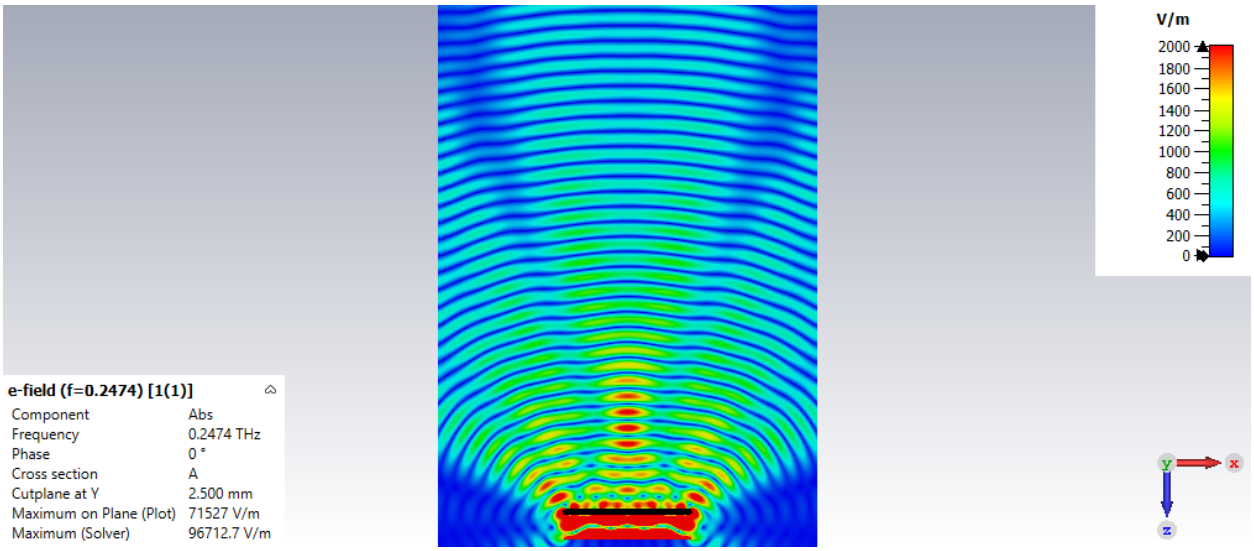
V/m
2000
1800
1600
1400
1200
1000
800
600
400
200
0
e-field (f=0.2474) [1(1)]
Component Abs
Frequency 0.2474 THz
Phase 0 °
Cross section A
Cutplane at Y 2.500 mm
Maximum on Plane (Plot) 71527 V/m
Maximum (Solver) 96712.7 V/m
Y
X
Z

(a)

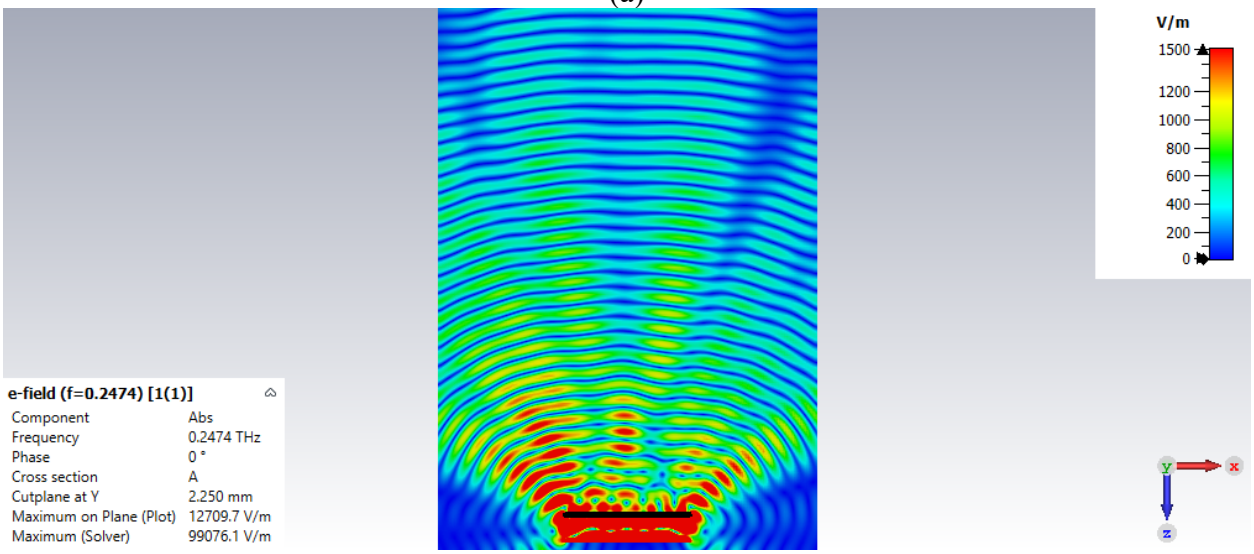
V/m
1500
1200
1000
800
600
400
200
0
e-field (f=0.2474) [1(1)]
Component Abs
Frequency 0.2474 THz
Phase 0 °
Cross section A
Cutplane at Y 2.250 mm
Maximum on Plane (Plot) 12709.7 V/m
Maximum (Solver) 99076.1 V/m
Y
X
Z

(b)

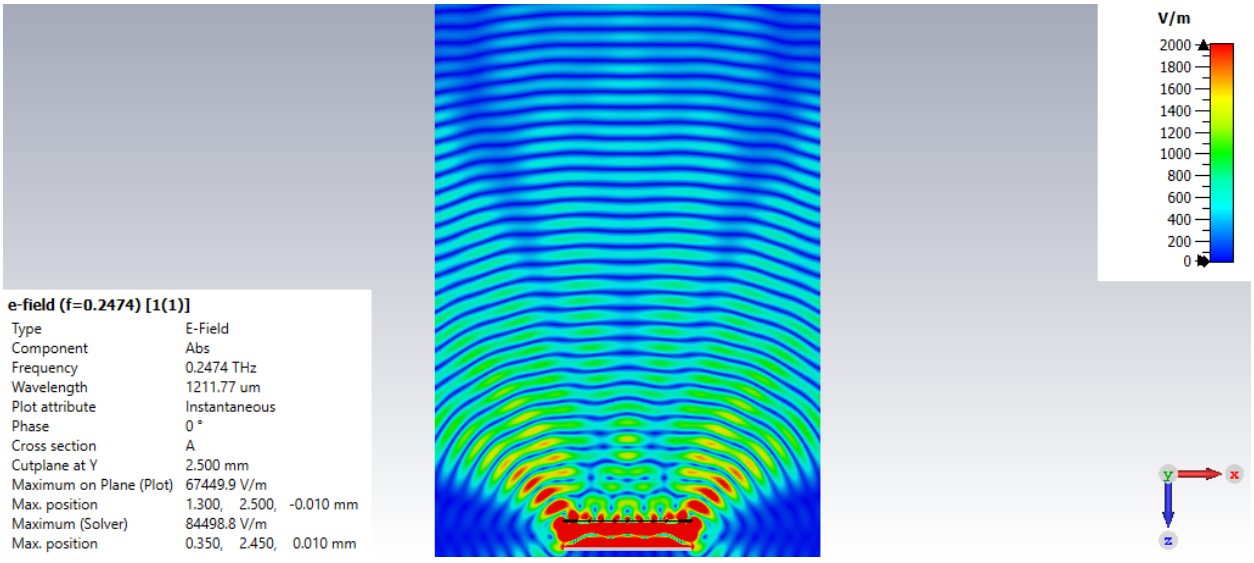

(c)

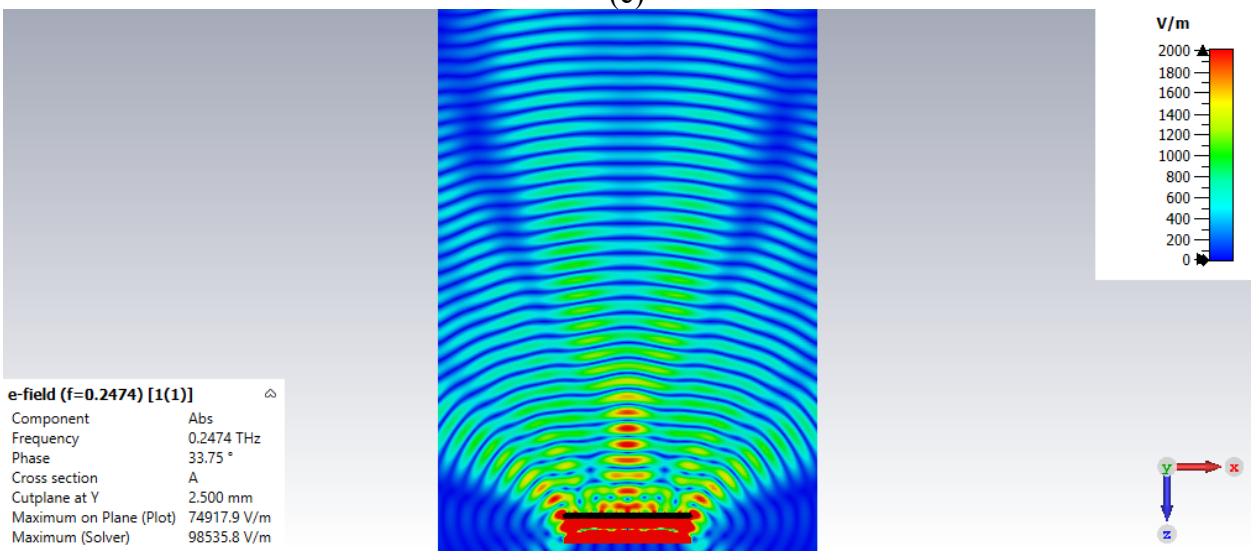

(d)

Figure 4.15. Top view of electric field progation when a) uniform phase profile is applied (OFF state), b) prism-like phase profile from Figure 4.14 is applied, c) convex lens emulation phase profile , and d) concave lens emulation phase profile.

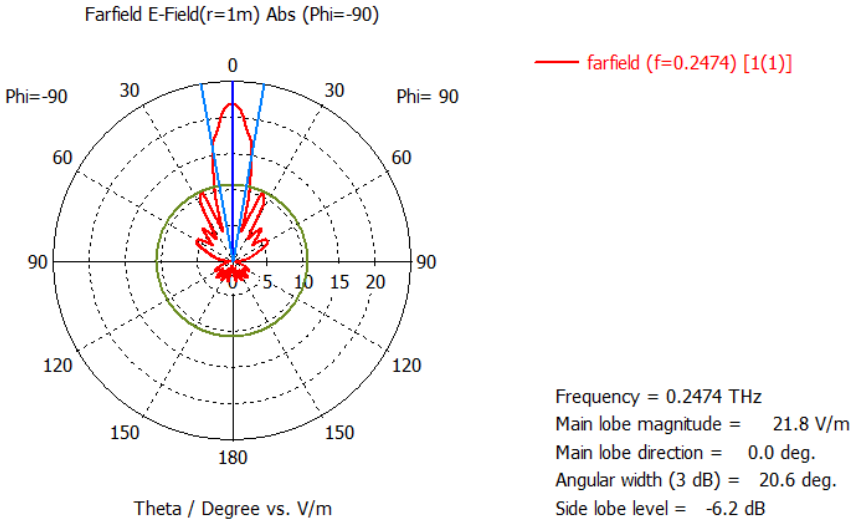
Farfield E-Field(r=1m) Abs (Phi=-90)
farfield (f=0.2474) [1(1)]
0
30
30
Phi=-90
Phi= 90
60
60
90
90
0
5
10
15
20
120
120
150
150
180
Theta / Degree vs. V/m
Frequency = 0.2474 THz
Main lobe magnitude = 21.8 V/m
Main lobe direction = 0.0 deg.
Angular width (3 dB) = 20.6 deg.
Side lobe level = -6.2 dB

(a)

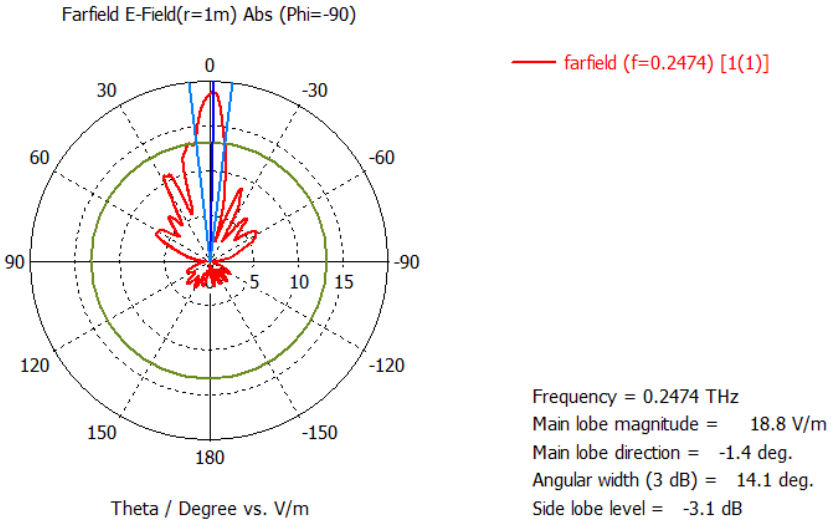
Farfield E-Field(r=1m) Abs (Phi=-90)
farfield (f=0.2474) [1(1)]
0
30
-30
60
-60
90
-90
0
5
10
15
120
-120
150
-150
180
Theta / Degree vs. V/m
Frequency = 0.2474 THz
Main lobe magnitude = 18.8 V/m
Main lobe direction = -1.4 deg.
Angular width (3 dB) = 14.1 deg.
Side lobe level = -3.1 dB

(b)

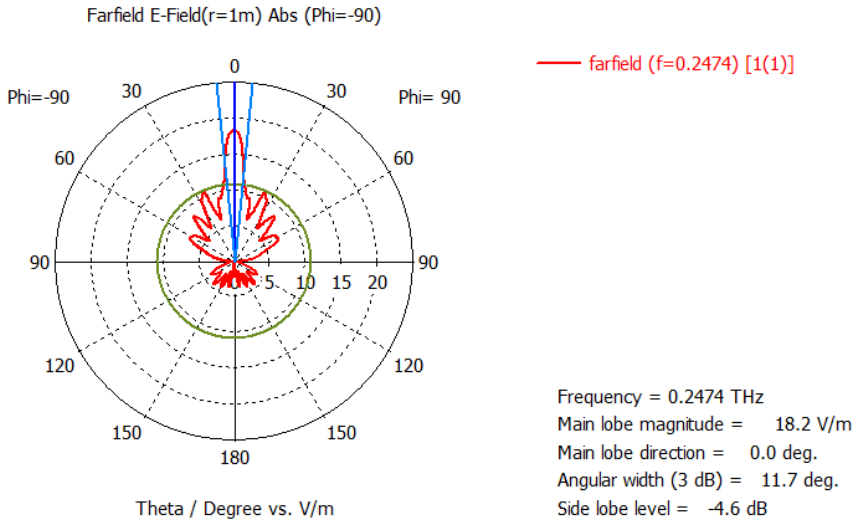

(c)

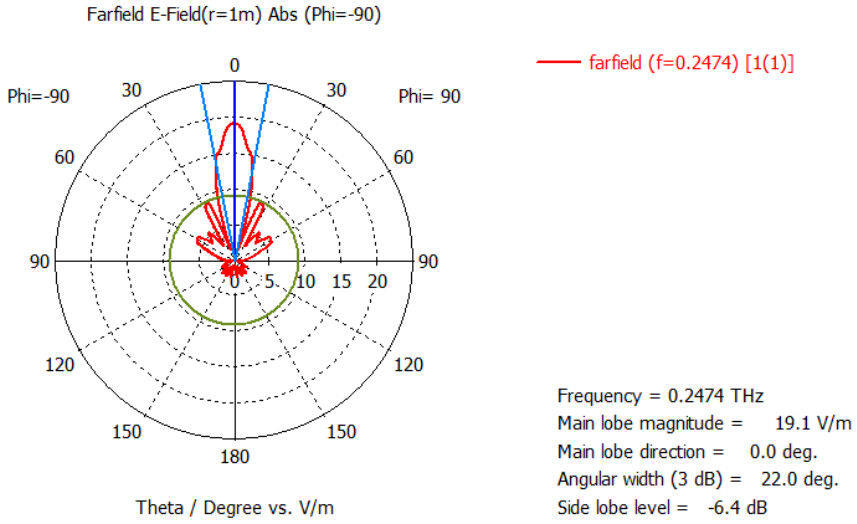

(d)

Figure 4.16. Polar plot of the farfield pattern for a) no voltage profile and b) prism-like phase profile, c) convex lens emulation phase profile, and d) concave lens emulation phase profile.

Additional phase profiles are tested to verify the ability of Device 7 to emulate optical components. The phase profile for emulating convex lens and concave lens are shown in Figure 4.14b and Figure 4.14c, respectively.

For convex lens emulation with the phase profile in Figure 4.14b, it can be observed that when the convex lens phase pattern is applied, the 10x10 Device 7 array diverges the incident wave in the near field electric field pattern (Figure 4.15c). In the far field pattern (Figure 4.16c), the divergence of the incident wave can be observed with decrease of angular width in the main lobe and also the increase in magnitude of the side lobes.

For concave lens emulation with the phase profile shown in Figure 4.14c, it can be observed in the near field electric field pattern (Figure 4.15d) that the convergence of electric field occurs closer to the array compared to when no phase profile is applied (Figure 4.15a). The far field pattern for the concave lens profile (Figure 4.16d) shows similar shape compared to when no phase profile is applied (Figure 4.16a), however, the magnitude of the overall pattern is reduced and the main lobe shows a wider angular width due to the shifting of focal point closer to the Device 7 array.

The results of the preliminary study demonstrated the Device 7's beam manipulation capability when it is arranged in an array. Different permittivity values are set in the PDLC layer to apply custom phase profiles emulating optical components and the effect of beam deflection, divergence, and convergence is observed in the corresponding components. It is noted that the phase-frequency characteristic of the device when it's in a finite array configuration differs from that of the phase investigation study due to the difference in boundary conditions. The deviation in frequency is less than 10%, meaning that phase investigation approach using unit cell boundary condition still provides a good estimate of the operating frequency. To account for this frequency deviation in the experiment, it will be necessary to re-characterize the phase-frequency characteristic of the device prototype to identify the optimal operating frequency and the corresponding phase vs voltage relation for proper and desired device operation.

Chapter 5. FABRICATION

Fabrication process of the device is completed in collaboration with students in National Tsing Hua University Taiwan Institute of Nanoengineering and Microsystems (NTHU iNEMS). In Section 3.3, we have discussed the advantages of using Polyethylene terephthalate (PET) as the substrate of the proposed Tunable Gradient Fishnet Metamaterial (TGFMM) device. However, due to the soft and flexible nature of the material, it is prone to wrinkling and curling during the fabrication process.

In this section, the considerations and measures that are used to prevent deformation on a flexible PET substrate during different parts of the fabrication process are discussed. Figure 5.1 shows the overview of the fabrication steps.

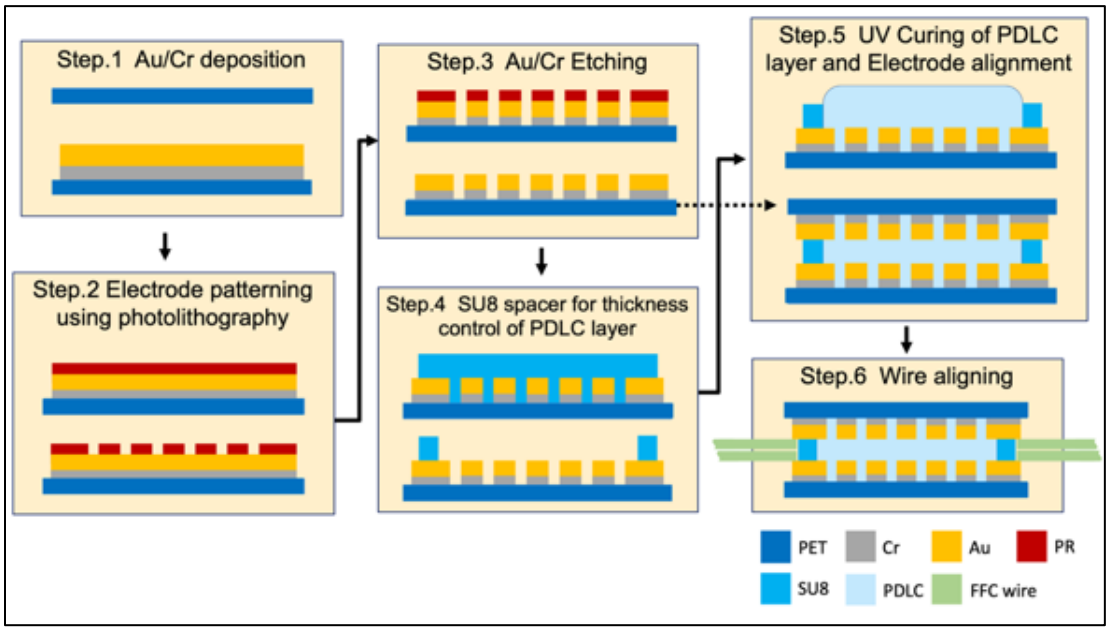

Figure 5.1. Schematic diagram showing the fabrication flow of TGFMM device.

5.1 METAL DEPOSITION CONSIDERATIONS

To create a uniform electrode layer, AST Peva-450I E-Beam Evaporation System (E-gun, Figure 5.2) is used to deposit the gold and chromium onto the PET substrate to form the electrode pattern. Using E-gun allows the metal to be deposited at a lower temperature compared to the other processes, which allows the PET substrate to remain below its glass transition temperature (75°C).

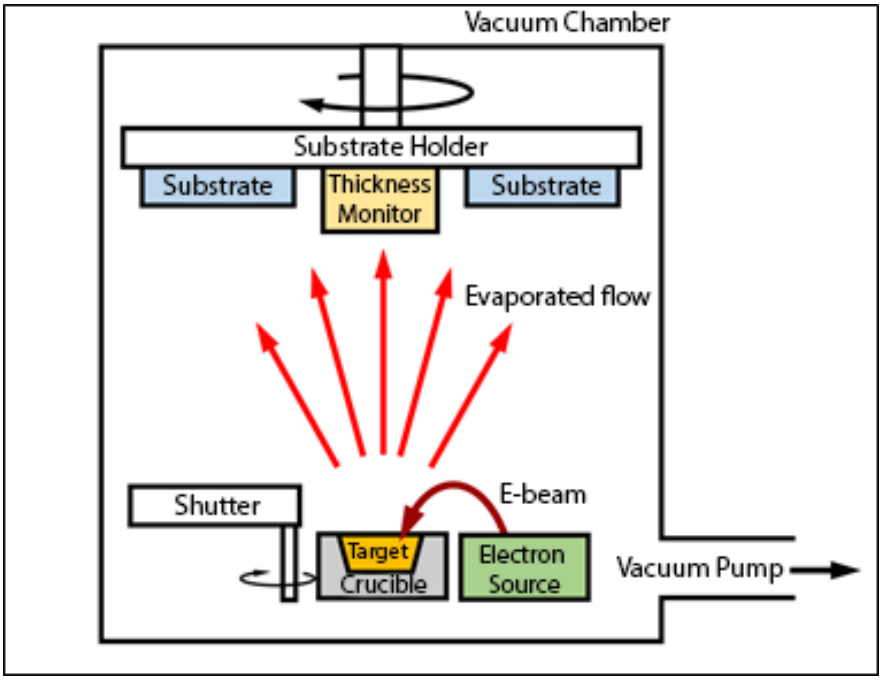

Figure 5.2. Schematic diagram of E-beam evaporation system.

Additional considerations are necessary to avoid curling and wrinkling of the substrate (shown in Figure 5.3). Curls and wrinkles on the substrate negatively impact the flatness and uniformity of the subsequent PDLC layer deposition and creates undesired disconnections in the electrode arms in the TGFMM array. These unwanted deformations can be potentially be caused by the expansion and contraction of the substrate due to the build-up of internal stress in the PET films during the metal deposition process.

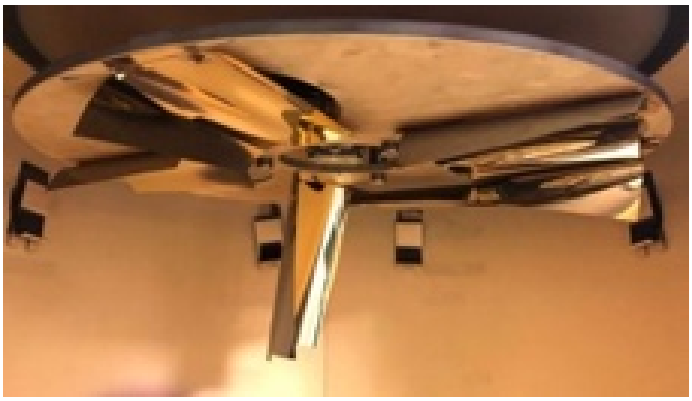

Figure 5.3 PET falls and curls inward after the metal deposition

Since the PET substrate is soft and flexible, it can be easily be deformed by tensile and compressive force exerted by the deposited metal layer. The build-up of the internal stress during the metal deposition process is then investigated to mitigate their effects on the PET substrate. The internal stress experienced by the substrate is affected by the deposition time and deposition rate.

For electron-beam physical vapor deposition (EB-PVD) process, the growth of the metal film can be described by the Volmer-Weber model [60], which describes the internal stress at the 3 different stages of deposition (Figure 5.4a): nucleation (I); coalescence (II); thickening (III) [61]. The internal stress is caused by the different states of metal formation on a substrate at different stages of the deposition as shown in Figure 5.4b. At the nucleation stage, a compressive stress is introduced to the substrate due to the formation of metal “islands” on the surface. At the coalescence stage, a tensile stress is introduced as the metal “islands” grows on the surface of the substrate and form connections with each other. At the thickening stage, a compressive stress is introduced as the connected metal layer grows thicker.

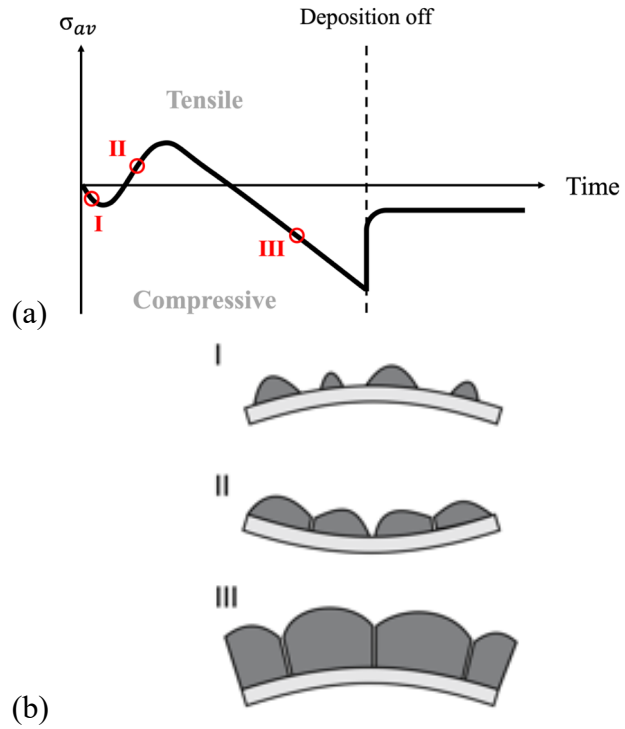

Figure 5.4. For electron-beam physical vapor deposition, the growth model of the metal film follows the Volmer-Weber model. (a) Plot of average stress vs time with constant deposition rate. (Reprinted from [61][62]) b) The schematic graph showing the side view of each stage. Based on the different inner stress of each stage, we can optimize the recipe and prevent unwanted deformation [63].

The internal stress between the metal and the substrate layer is also affected by the metal deposition rate as shown in Figure 5.5. Low deposition rate introduces compressive force to the substrate due to the formation of a higher density metal layer, while high deposition rate introduces aa tensile force on to the substrate.

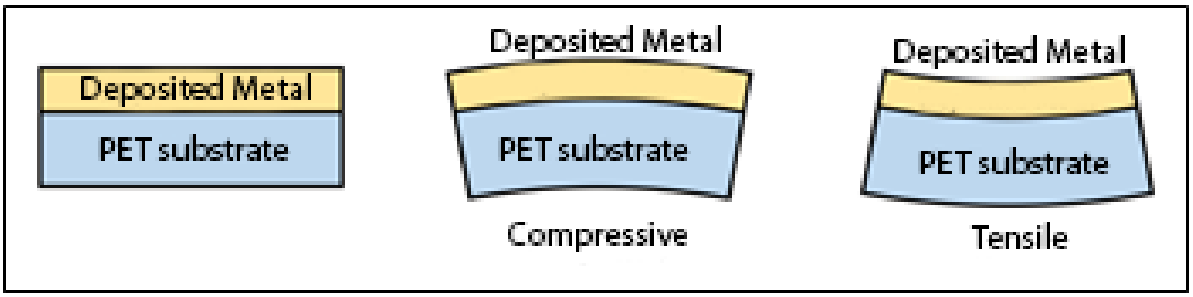

Figure 5.5. Deposited results with no internal stress, compressive stress, and tensile stress. Compressive stress bends the substrate outwardly, while tensile stress bends the substrate inwardly.

The metal deposition recipe is optimized by balancing both of the stress-introducing factors: the deposition time and deposition rate, in order to maintain the flatness of the substrate after deposition. Figure 5.6a. shows the thickness vs time chart of the chromium deposition for the adhesion layer. Figure 5.6b. shows the thickness vs time chart. The gold deposition is divided into 3 stages. At Stage I of the deposition, the deposition rate of 0.1Å per second is used to produce a dense gold layer with good adhesion to the chromium layer to prevent the electrode pattern of TFGMM from easily cracking. The dense layer and also the deposition state of Stage I introduces a compressive force on the substrate, thus the deposition rate is increased 0.2Å per second at Stage II. The increase in deposition rate creates a thinner metal layer which introduces a tensile force to reduce the compressive force introduced in Stage I. Also, the deposition state of the metal at Stage II will introduce additional tension forces. The metal deposition is continued on beyond Stage II at 0.3Å per second with to increase the thickness metal layer with low density metal in order to balance out the tensile stress introduced in Stage II.

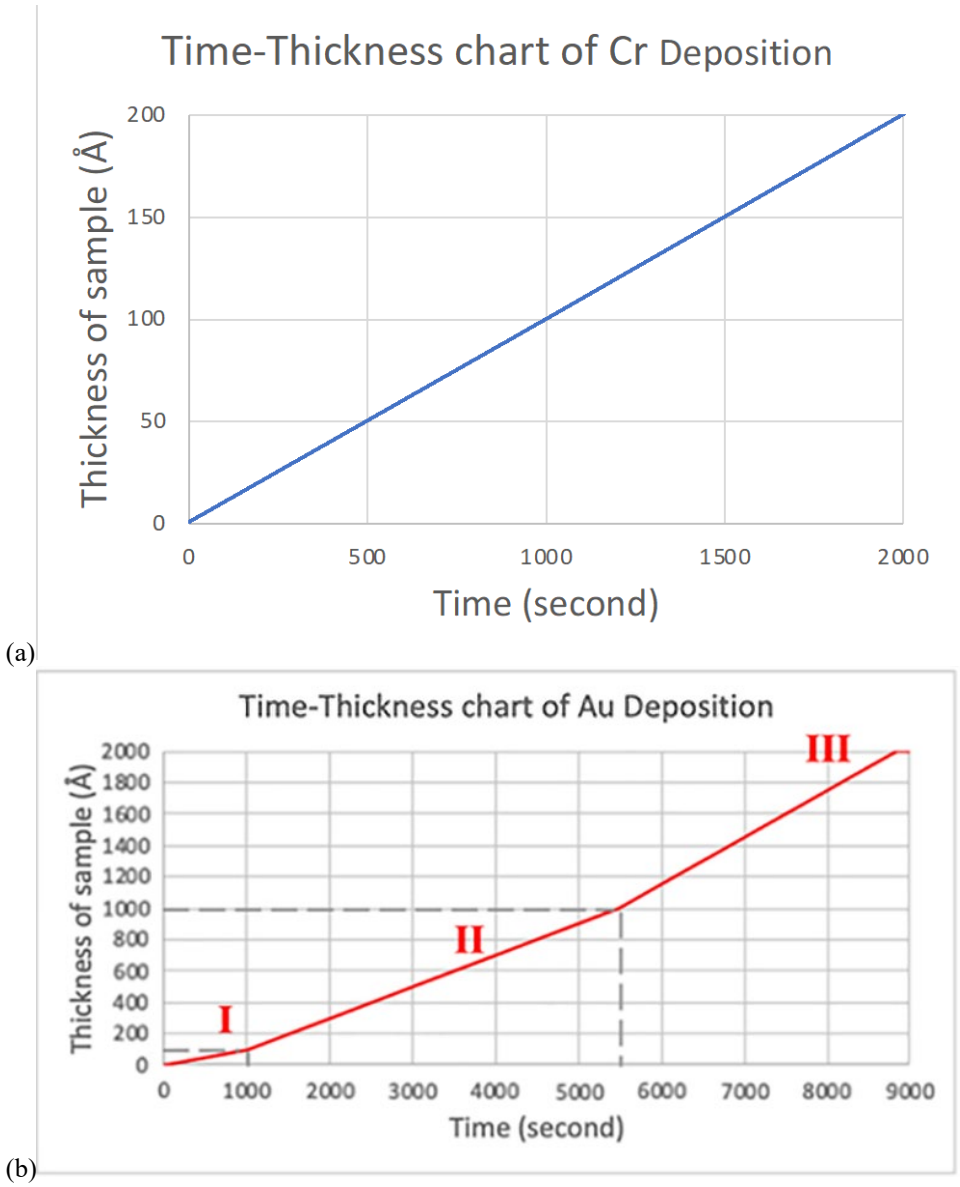

Figure 5.6. (a) The thickness vs. chart of chromium deposition. (b) The thickness vs. time chart of gold deposition.

By optimizing the time ratio and deposition rate of the metal deposition recipe, the deposition results in a nice and uniform layer of metal as shown in Figure 5.7 and it is ready for patterning using photolithography.

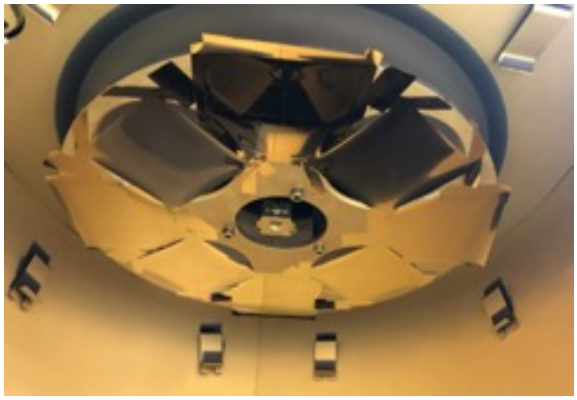

Figure 5.7. Deposition result after solving the attachment problem and the internal tension problem.

5.2 PHOTOLITHOGRAPHY CONSIDERATIONS

For patterning the electrode geometry, Nano Imprint EVG620 is used for photolithography with positive photoresist EPG-512. The following section discusses the necessary considerations during the photolithography process for preventing unwanted deformation and wrinkles on the flexible PET substrate.

Humidity on the substrate during the photolithography process causes bubble-shaped deformations (shown in Figure 5.8a) in the middle of the sample. During the pre-bake process, the water droplets on the surface of the PET substrate becomes steam and bubble-shaped deformations are formed when the steam is captured by the PET substrate. To prevent the creation of the bubble deformations, the PET substrate is thoroughly dried prior to the heating process and the position of the sample is frequently changed during the heating process to prevent the capturing of steam from residual surface water droplets (Figure 5.8b). Additionally, the sample is taped on a glass disk after the bottom side of the sample is dried (Figure 5.8c).

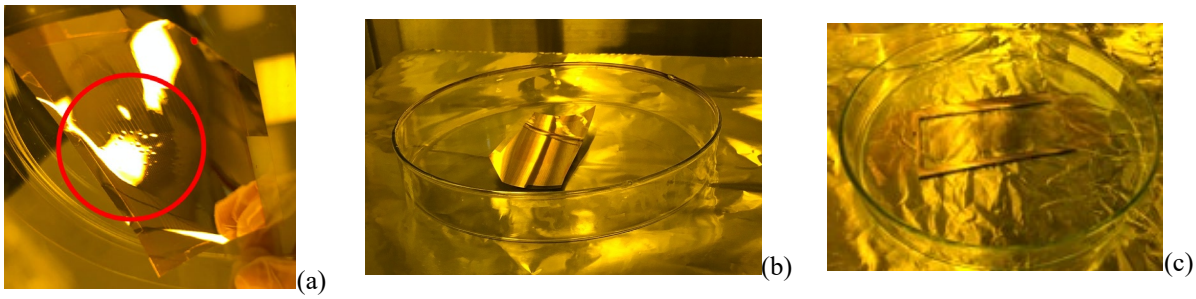

(a) (b) (c)

Figure 5.8. Photolithography problem. (a) Some bubble-shaped deformations occur in the middle of the sample during hot plate heating. (b) Frequently change the position during the heating can prevent steam captured under the sample. (c) Tape the sample on a glass disk after the bottom side of the sample is dry. This can prevent the sample from deformation.

To ensure the uniformity of the photo-resist coating, rocking movement of the substrate during the spin coating process must be minimized. Any rocking movement of the substrate can cause the formation of creases on the surface of the PET (Figure 5.9a). To prevent the unwanted movement of the substrate, the PET substrate must be smaller than 4" for it to be properly secured on the wafer. Additionally, it is critical to carefully check the photoresist for bubbles prior to spin coating and remove them with a dropper to minimize the defects in the photoresist coating. (Figure 5.9b).

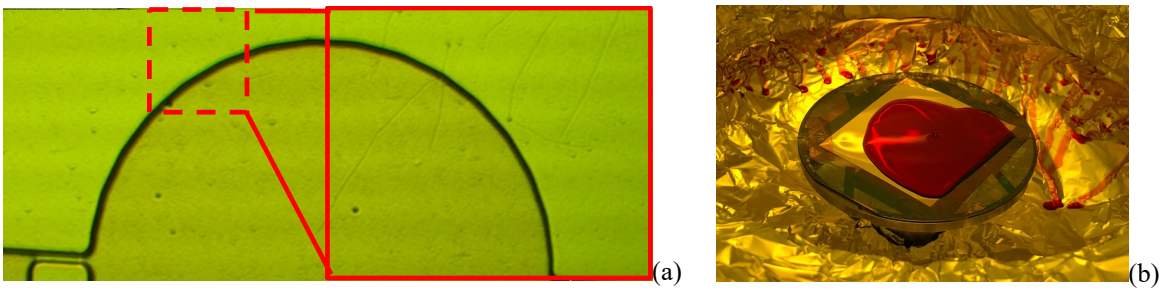

(a) (b)

Figure 5.9. (a) Formation of creases on PET substrate due to rocking movement. (b) PET substrate properly secured to a 4" wafer. Photoresist is checked for bubbles.

5.3 ETCHING

The wires connecting the slabs of the electrodes are critical to the function of the device. On a flexible substrate, the wire geometry is prone to breaking during the etching process if there is excessive vibration due to its significantly smaller feature size (10μm) comparing to the slab (400μm). To minimize the vibration during the etching process, the substrate is immersed gently into the solvent at an angle so that the metal is removed by the force of gravity without agitation of the etchant. The electrode arms are carefully checked under the microscope right after the etching process to ensure that the connection between the electrodes remains intact as shown in Figure 5.10 and the conductivity of the electrode arms is verified using LCR meter.

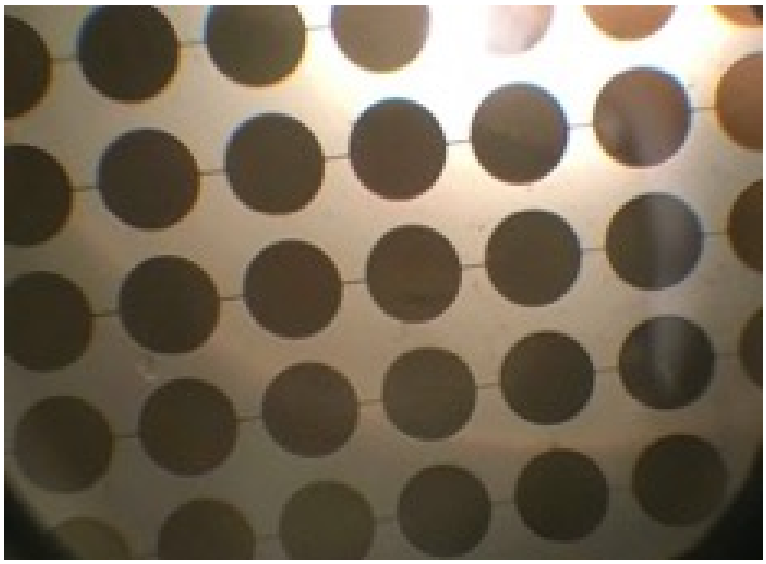

Figure 5.10. The etching result of the sample under the microscope. The connection of electrode arms is carefully checked under the microscope right after the etching.

5.4 SU-8 SPACER

A 10μm thick spacer is created on one of the electrode-deposited substrates to control the thickness of PDLC layer between the top and bottom electrode. To create the spacer, Nano Imprint EVG620 (Figure 5.11a) is used to pattern SU-8 2010. The mask design of the spacer is shown in Figure

5.11b. A 25mm x 25mm cavity serves the purpose of containing the PDLC during the curing process, and channels are created on the sides of the spacer for siphoning the PDLC during the deposition process.

(a)

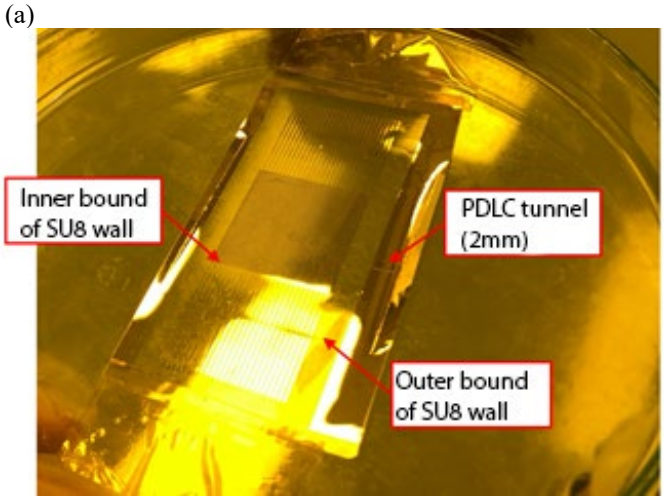

(b)

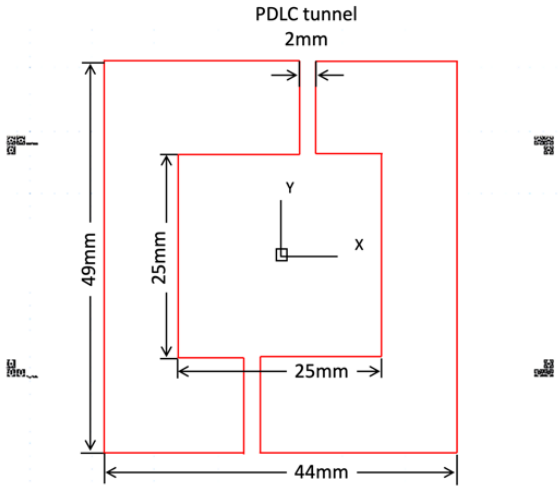

Figure 5.11. (a) The picture of the one-way connected circle with spacer. (b) The optical mask design of the spacer.

Based on the vendor recipe, the dwell speed of the spin coater is set to 3500rpm and the dwell time is set to 35 seconds. This setting produced an SU-8 spacer with the height slightly less than 10μm (Figure 5.12) on the PET substrate. Thus, the dwell speed needs to be lowered or the dwell time needs to be reduced to achieve the target SU-8 thickness.

Based on the Bruker Dektak XT's alpha-step measurement results of trials with lower spin speed (Figure 5.12b) and reduced dwell time (Figure 5.12c), the recipe with lower spin speed is able to achieve the target thickness, while the recipe with lower dwell time is not able to do so. Based on the testing results, the dwell speed is changed from 3500rpm to 3000rpm.

Since the substrate is flexible, device deformation can occur easily during fabrication and measurements. It can be observed from Figure 5.12 (a-c) that the surface profiler results of PET with SU8 spacer are bending outward due to the friction induced by the needle of the profiler. To mitigate this problem, a change in the length and orientation of the measurement path is made. Figure 5.13a shows the original path of measurement and Figure 5.13b shows the new path of measurement. The new path of measurement is shorter and in a different orientation to minimize the bending of the device during measurement. Figure 5.14 shows the profiling result using the new path of measurement. It can be observed that by changing the direction of the measurement path and shorten its distance, the bending of substrate is reduced, giving us a more leveled thickness profile. The thickness of the side wall produced by reducing the spin speed is 9.5μm, which is close to the target thickness of 10μm.

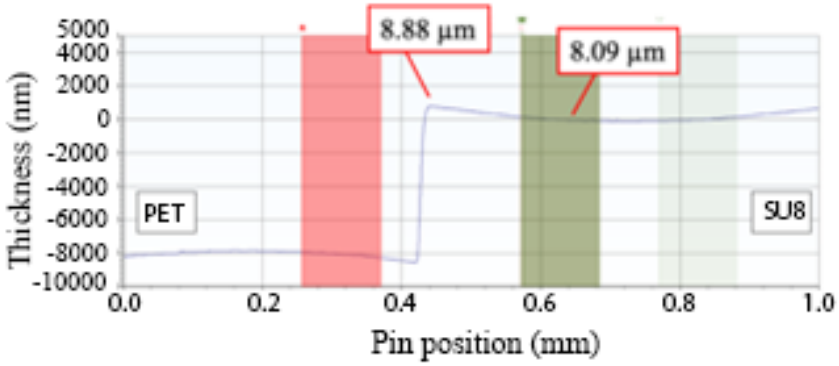

(a)

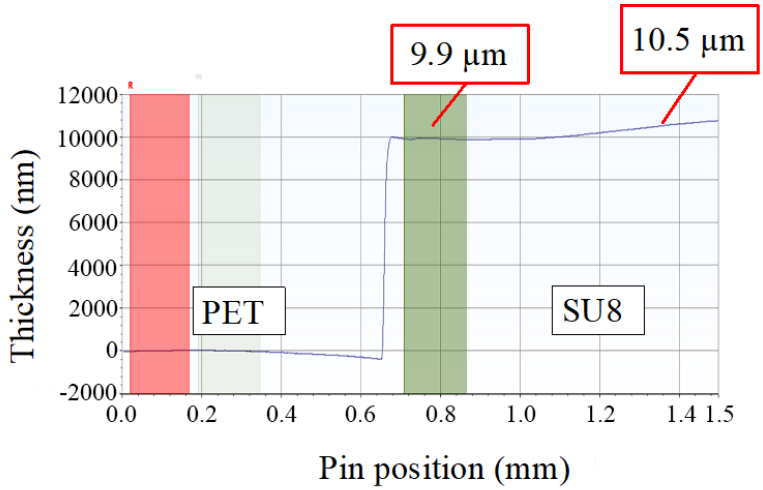

(b)

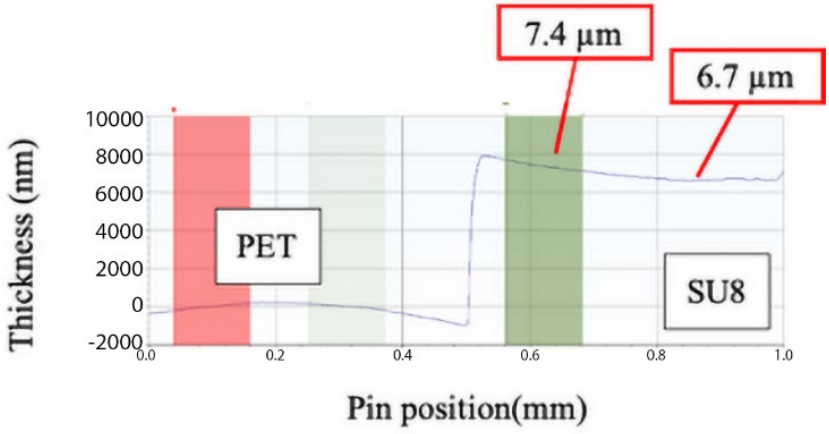

(c)

Figure 5.12. Bruker Dektak XT's α – step for measurement results. (a) Result of the vendor recipe (3500rpm spin coating speed and 35sec dwell time). (b) Result of lower dwell speed. (c) Result of lower dwell time.

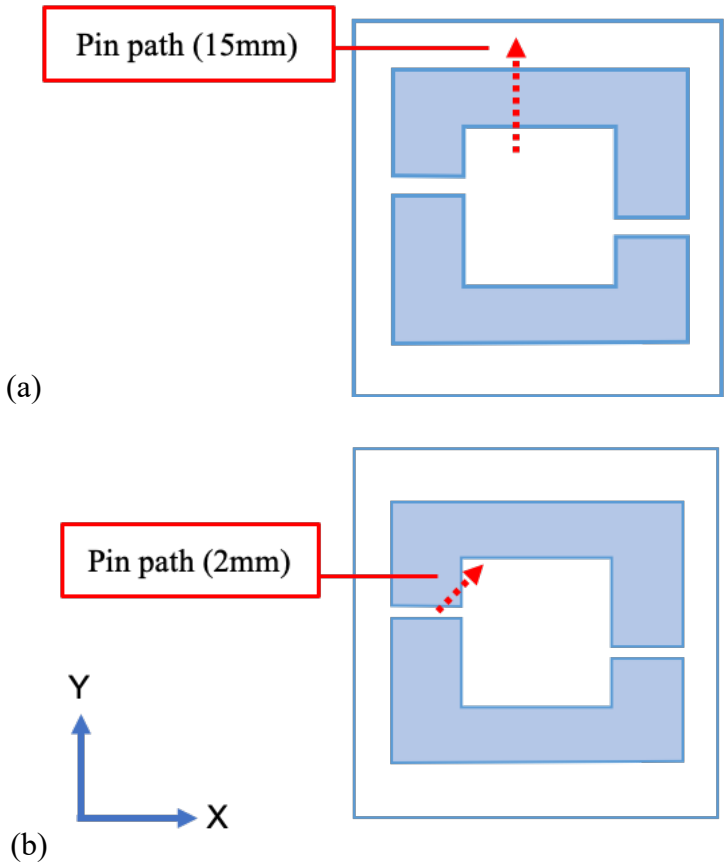

Figure 5.13. a) Original measurement path of the optical profiler. b) Revised measurement path of the optical profiler to reduce bending of the substrate

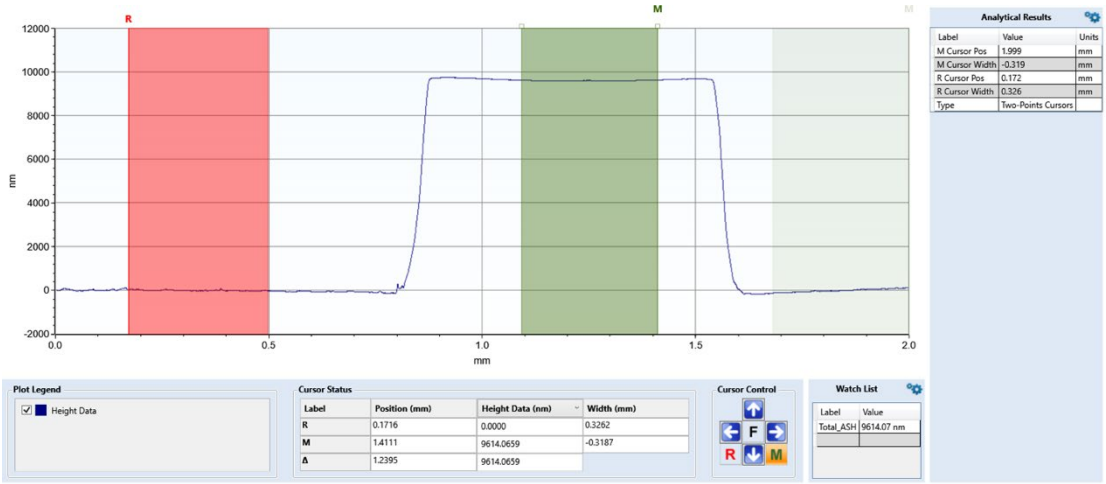

Figure 5.14. SU-8 spacer thickenss profile using revised measurement path

5.5 Electrode Aligning and Curing the PDLC Layer

The alignment of the top and bottom electrodes and the curing of the PDLC layer can be completed as a single step due to the omission of the skin layer in our previous design, which simplifies the fabrication process. Critical requirements for this step are to ensure that an even PDLC layer is created with minimal defect and also the alignment can be completed before the PDLC is complete cured.

Desktop Mask Aligner from Deya Optronic Co. (shown in Figure 5.15) is used for aligning the electrodes while simultaneously curing the PDLC layer via ultraviolet (UV) light exposure. This aligner provides several advantages for the alignment process: the separation gap can be precisely controlled after leveling, and the vacuum system can be controlled during the aligning process, which fits the specific needs of our fabrication process.

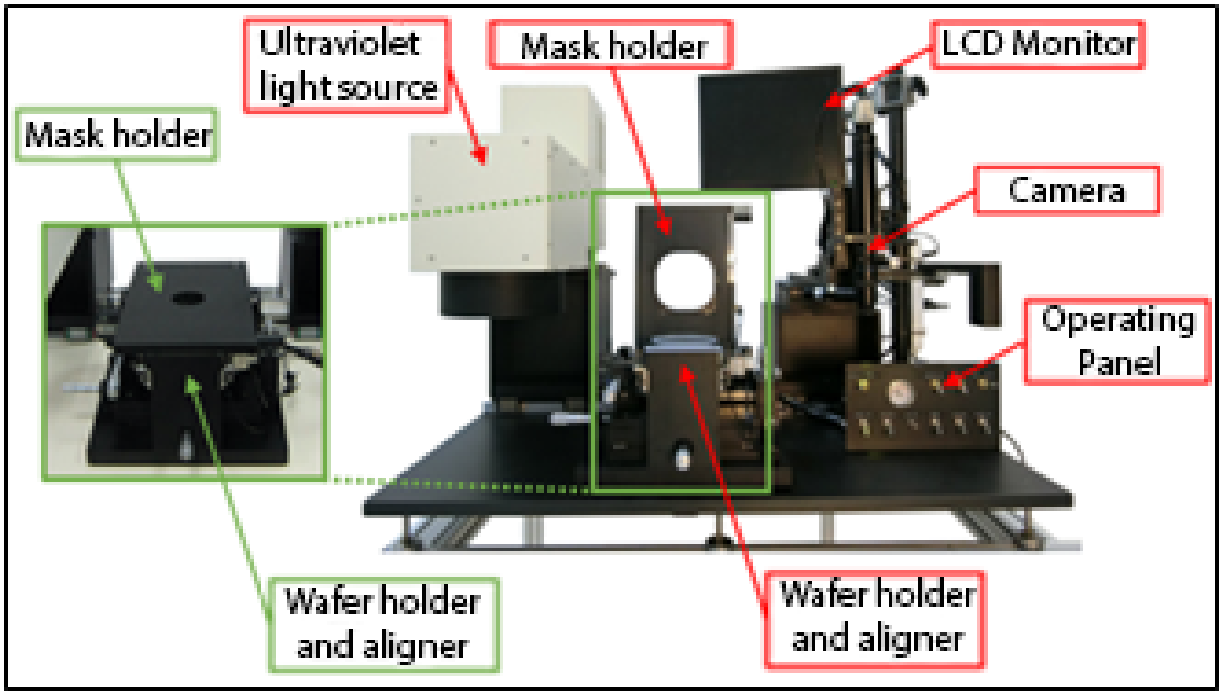

Figure 5.15. The Desktop Mask Aligner from Deya Optronic Co. This aligner allows us to control the separation gap between the mask and the wafer. More importantly, the vacuum system of the mask holder can be controlled during the aligning, which can meet the special needs of our device fabrication process. [64]

To use the aligner with flexible substrates, the metalized substrate with a SU8 spacer (the bottom electrode) is taped onto a 4" wafer and placed on the wafer holder of the aligner (Figure 5.16a) and the metalized substrate without SU8 spacer (the top electrode) is taped on to a photomask blank and placed on the mask holder of the aligner. (Figure 5.16b). After leveling the photomask blank and the wafer, the separation gap between the mask blank and the wafer is carefully adjusted. Figure 5.17a shows the measurement of the separation gap.

(a) 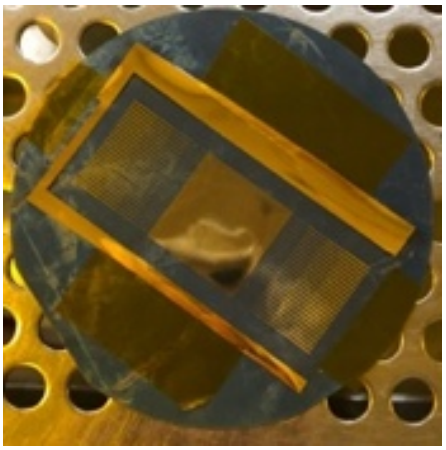 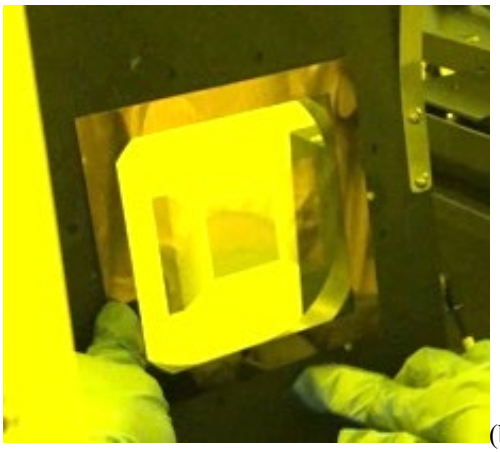 (b)

Figure 5.16. The setup for electrode alignment and the PDLC layer curing process. (a) A substrate with SU8 spacer is attached to a 4" wafer, and the wafer is set on the aligner. (b) A substrate without SU8 spacer is taped on a photomask blank and put on the mask holder of the aligner.

A volume of 0.00625ml of PDLC is required to fill the 25mm x 25mm cavity in the spacer to create a 10μm thick layer. To get the accurate volume of PDLC, the PDLC is steadily dropped in the cavity between the SU8 sidewall using a micropipette to avoid creating bubbles within the PDLC.

After dropping the PDLC, the electrode patterns on the top and bottom substrates of the device are aligned by adjusting the 4" wafer on the aligner. This step needs to be completed in a timely manner to ensure that the PDLC layer is uniform before it solidifies to minimize possible deviation in the device's geometric parameters.

During the alignment, the separation gap (Figure 5.17a) is set at 40μm, so that the surface of PDLC does not come in contact with the upper electrode. After aligning the electrode patterns, the separation gap is slowly adjusted from 40μm to 0μm (Figure 5.17b) and then the vacuum system of the mask holder is turned off to allow the photomask blank to rest directly on top of the SU-8 spacer of the bottom electrode substrate. The full weight of the photomask blank provides extra pressure to the device during the UV light exposure to maintain the flatness and improve the uniformity of the PDLC layer during the curing process (Figure 5.17c).

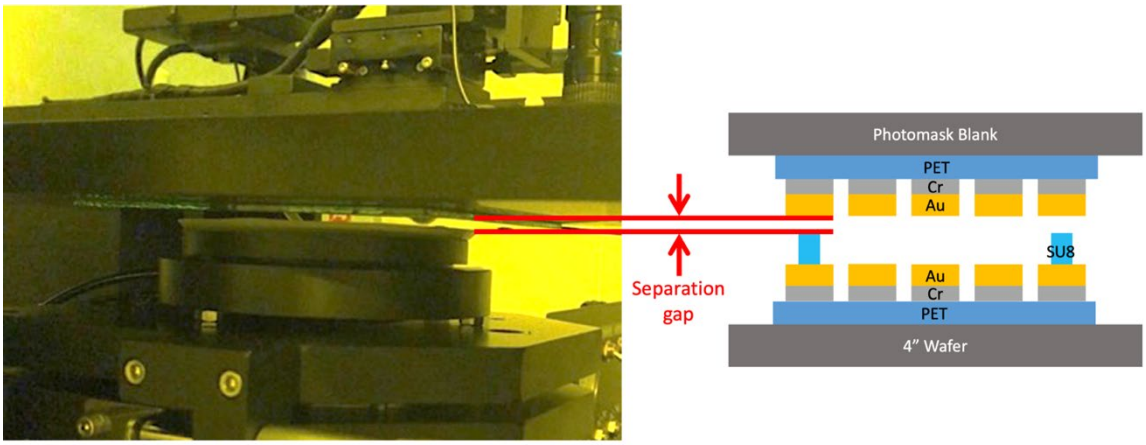

(a)

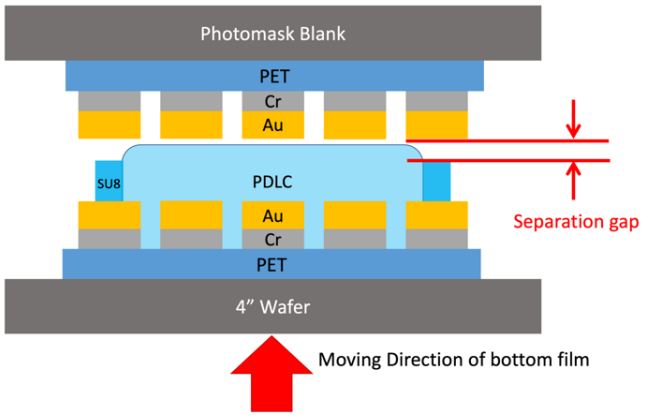

(b)

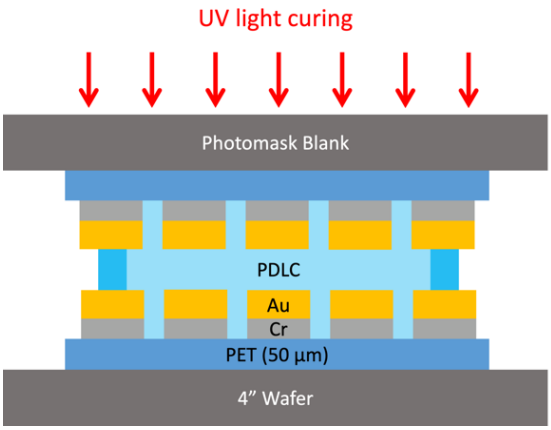

(c)

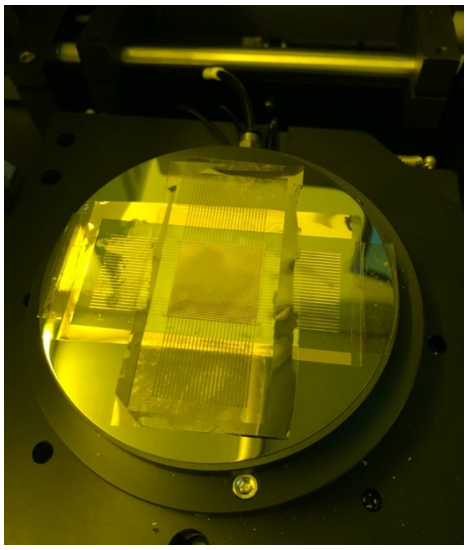

(d)

Figure 5.17. (a) Separation gap measured between to electrode and SU-8 spacer (b) Reduction of separation gap toward 0µm by raising the bottom 4” wafer in the aligner (c) Photomask rested directly on top of the SU-8 spacer after turning off the mask holder vacuum during UV curing process (d) Device after UV light curing.

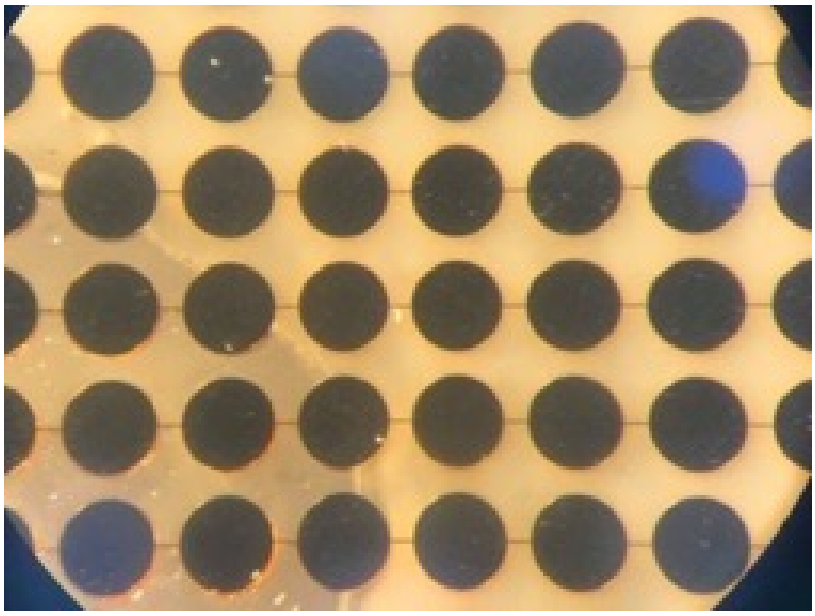

Figure 5.18. Microscope picture of the devices after UV light curing.

After the curing process is completed (Figure 5.17d), the TGFMM device is inspected under the microscope for defects and misalignments. With the considerations discussed in this section; the geometry of the resulting device matches closely with the Device 7 design. The electrodes are properly aligned and a large area of uniform PDLC layer is created (Figure 5.18).

Chapter 6. EXPERIMENT AND RESULTS

6.1 DEVICE CHARACTERIZATION

Experiments are completed in collaboration with students in National Tsing Hua University Taiwan Institute of Nanoengineering and Microsystems (NTHU iNEMS).

The fabricated TGFMM device is characterized by its S_{21} magnitude and phase change when voltage is applied. It is critical to determine the operating voltage and phase change characteristic of the device to ensure that the device is operating at optimal performance. The operating voltage of the device is largely dependent on the turn on voltage and also the saturation voltage of PDLC, as PDLC will only show significant transmission changes (thus, the change in permittivity due to rotation of liquid crystal molecules) between the turn on voltage and the saturation voltage as shown in Figure 3.4. As shown in the simulation results, the resonance dips of S_{21} magnitudes will change whenever the PDLC permittivity changes. Thus, by observing the behavior of the resonance peak while applying voltages to the device will allow us to figure out the optimal operating voltage of the device. This will also allow us to determine the operating frequency of the device as the peak phase change frequency will lie between these two peaks as shown in the simulations.

For determining the optimal frequency, the S_{21} phase change will be measures for frequencies between the two S_{21} dips (OFF State and ON state) to find out where the maximum phase change occurs.

6.1.1 *S_{21} Magnitude Characterization*

The S_{21} magnitude of the TGFMM device will be measured using TeraScan 1550 continuous wave THz system and the setup is shown in Figure 6.1. The TGFMM device will be placed between the

emitter and receiver of TeraScan 1550 system. An acrylic holder (Figure 6.2) is used to mount the device in the set up securely and to provide a secure interconnect for the flat ribbon cables that connects the electrodes of the device to the driving circuit (Figure 6.1a). A 11mm diameter shutter is introduced in front of the emitter to reduce the beam to the size of the active area of the TGFMM device (Figure 6.1b).

For device characterization, voltages will be applied uniformly across the entire array using the driving circuit and the S_{21} magnitude is measured using TeraScan 1550.

To ensure the consistency of the measurement, the device needs to be reset to the same initial state between each measurement. Since liquid crystal is a ferroelectric and ferromagnetic material, it can be actuated by electric field or magnetic field. Thus, it is possible to reset the device by applying strong uniform electric field or magnetic field to rotate the liquid crystal molecules into a desired orientation. To avoid exposing the device to high voltage, which can lead to its break down, magnets are used as the method of resetting the liquid crystals orientation. For maximum performance, it is ideal to have the liquid crystals molecules oriented in a way that extraordinary direction of its optical axis is parallel to the electrodes (z-direction in Figure 6.3). To accomplish that, a magnetic array is configured in a way such that it forms a uniform magnetic field in the direction parallel to the electrodes (Figure 6.3). The exposure of the device to the uniform magnetic field resets the liquid crystals droplets in the PDLC layer of the device to a consistent starting orientation before each of the measurement.

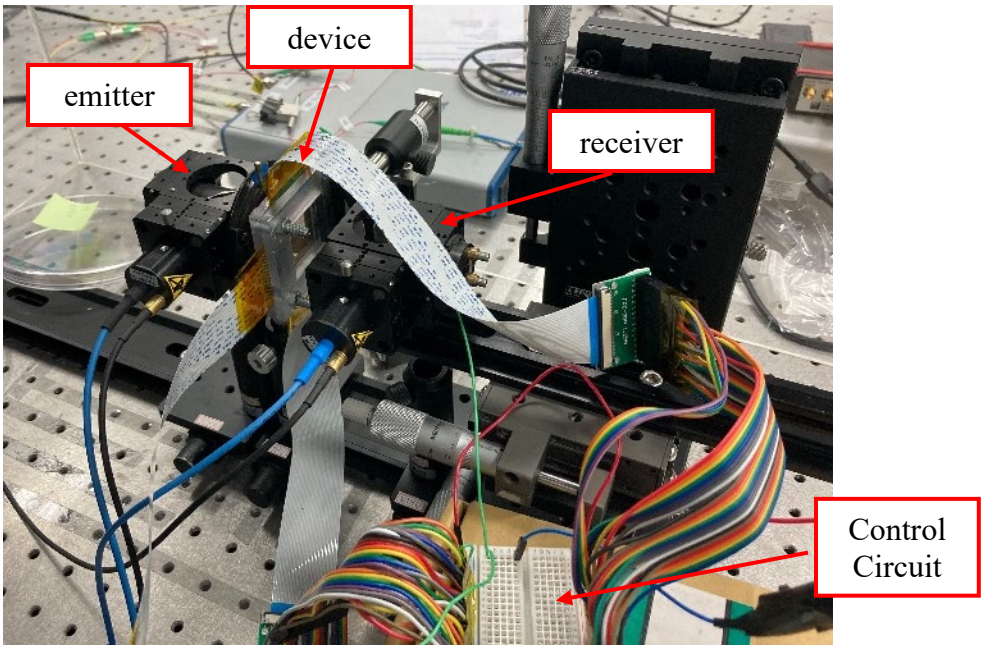

(a)

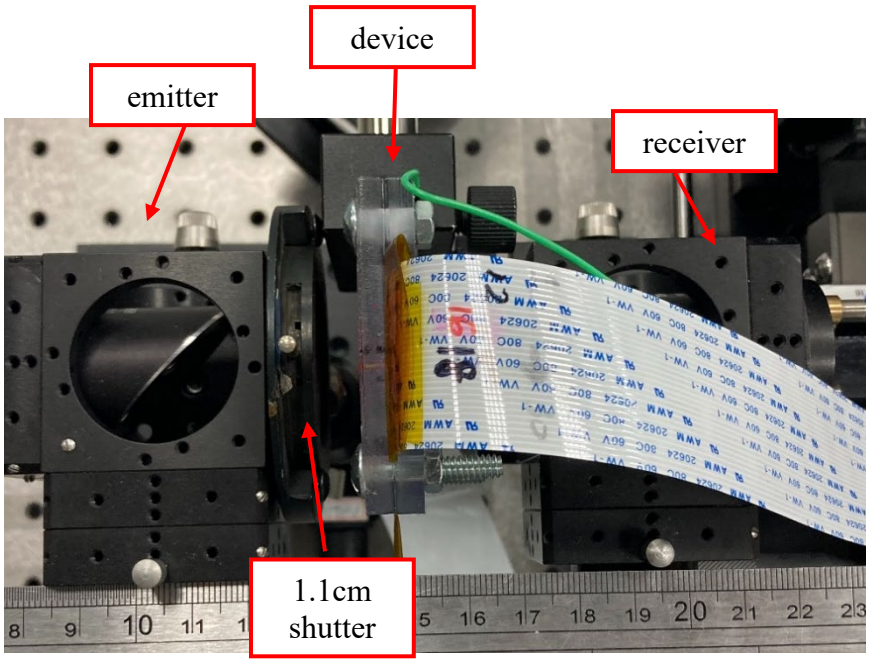

(b)

Figure 6.1. TeraScan 1550 setup for device characterization: a) overall view showing the control circuit b) top view showing the 1.1cm shutter

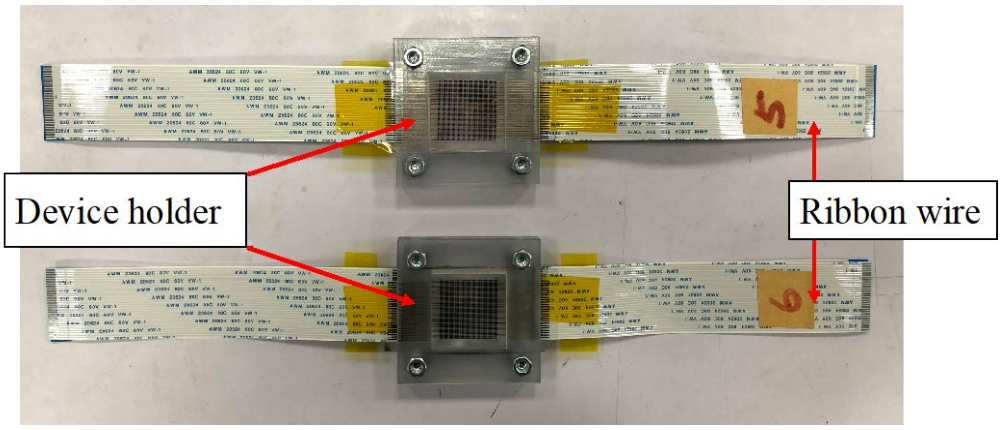

Figure 6.2. Device holder for mounting the device in our experiment setup and also providing a secure interconnect for the flat ribbon wires.

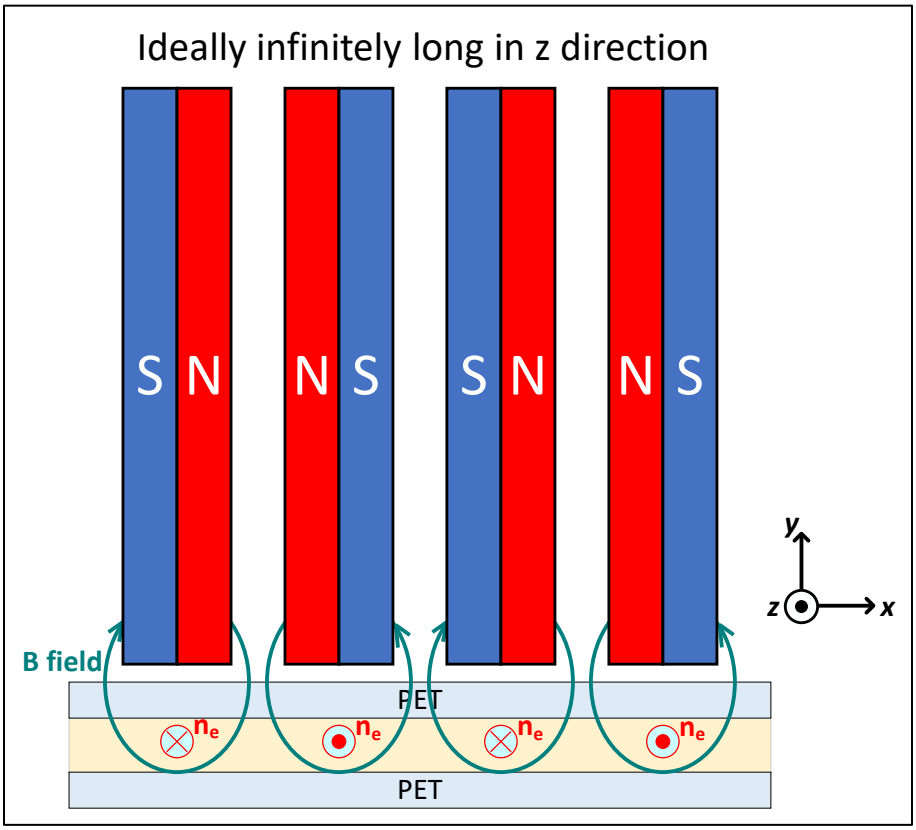

Figure 6.3. Resetting the PDLC layer of the device using magnet array

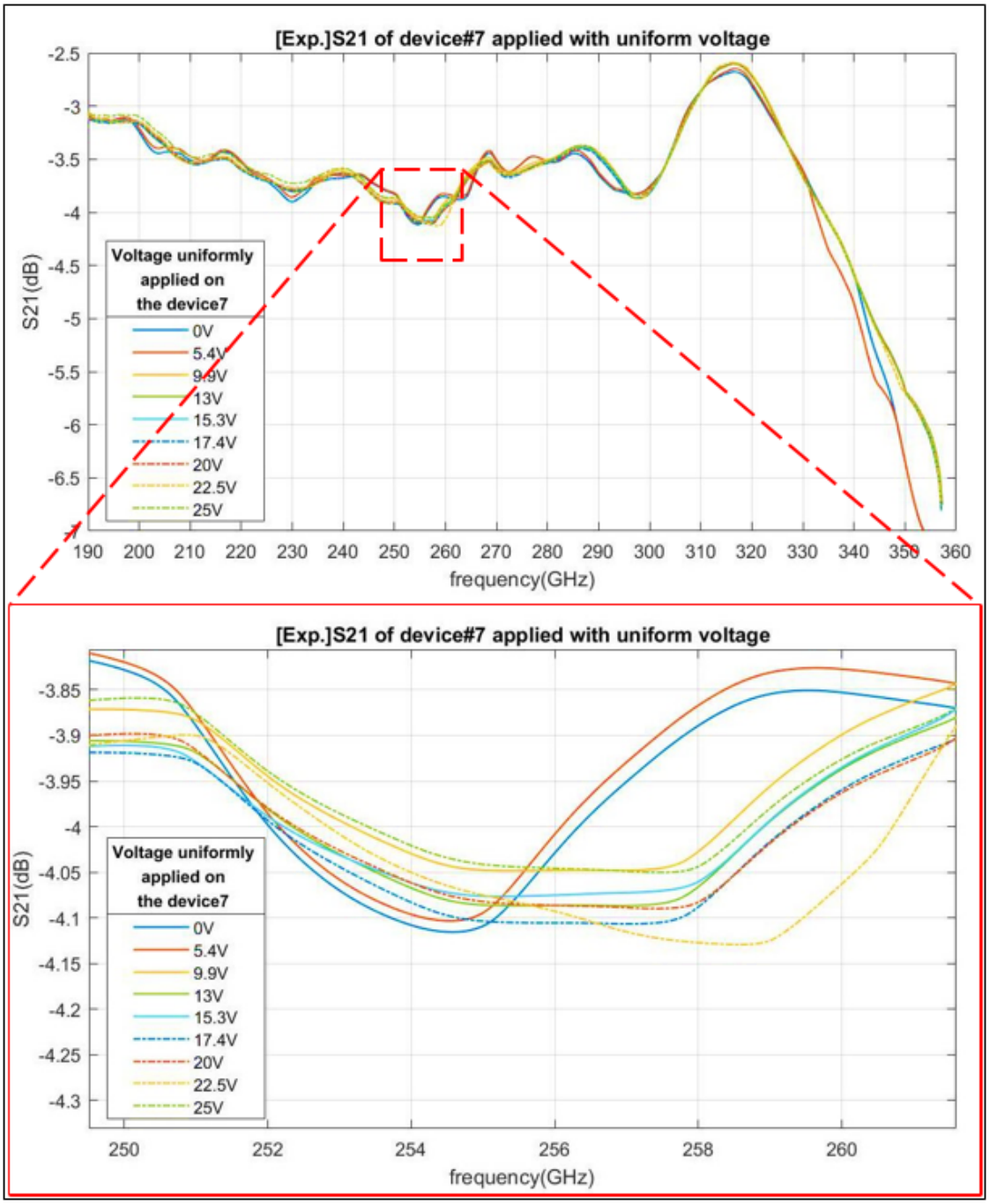

Figure 6.4. S_{21} spectrum measured using TeraScan 1550

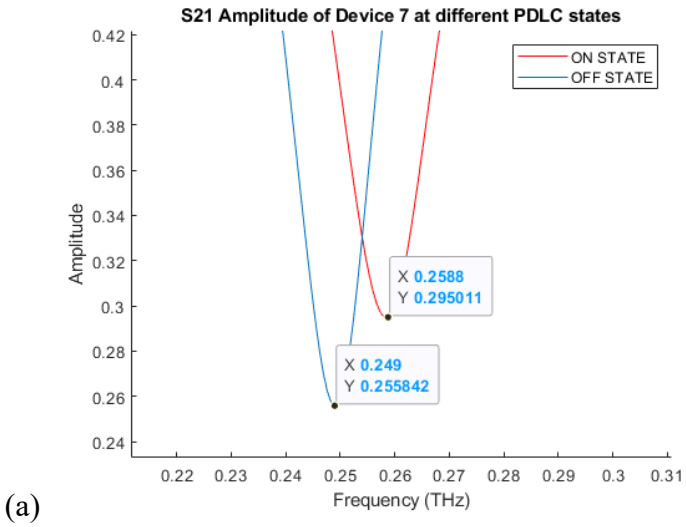

(a)

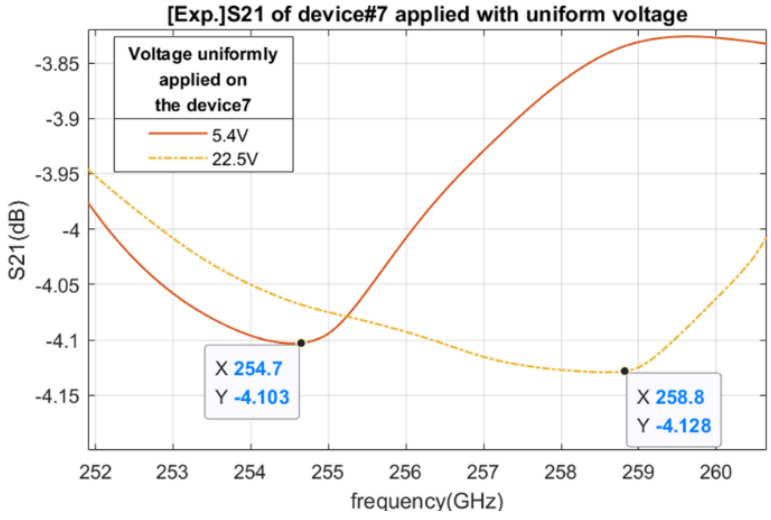

(b)

Figure 6.5. Comprison of S_{21} dip frequency shift between Device 7 (Simulation) and TGFMM (Experiment)

Figure 6.4 shows the measured S_{21} magnitude spectrum for different uniformly applied voltages across the array with 0.03GHz frequency steps. It can be observed that the resonance dip graduately shifts to higher frequency starting at 5.4V up until 22.5V. At 25V, the peak shifts back to lower frequency. Based on shifting pattern of the S_{21} dips, it can be concluded that the operating voltage of the device ranges from 5.4V up to 22.5V. Figure 6.5 shows the comparison of S_{21} dip

frequency shifts between the simulation and experiment. It can be observed that the S_{21} dip shifts from 0.249THz to 0.2588THz in the simulation between the OFF-state and ON-state, while the S21 dip shifts from 0.2547THz to 0.2588THz between the turn on voltage (5.4V) and the saturation voltage (22.5V) in the experiment. The similarity in S_{21} dip frequency shift between the simulation and the experiments indicates that the frequency characteristic of the TGFMM device matches closely with the Device 7 design, where the permittvity of the PDLC layer decreases as increasing voltages are applied. The mismatch on the lower frequency shows that the permittivity of the PDLC in the experiment at 5.4V is not the same as the permittivity of the PDLC in the simulation at its OFF state. The variation in permittivity is due to the liquid crystal molecules in the PDLC are typically in random scattered orientation before a voltage is applied to it. While the magnetic pre-alignment process is able to reset the the starting orientation of the liquid crystal droplet consistently, it might not reset them to the exact permittivity state defined in the simulation.

6.1.2 *S_{21} Phase Characterization*

The S_{21} phase cannot be measured directly using the TeraScan 1550 system, however it can be retrieved from the measured photocurrent. The relationship between the photocurrent and the phase is described by (6.1) according to the TeraScan 1550 user manual:

$$I_{ph}(\omega) = E_{THz}(\omega)\cos(\phi) = E_{THz}(\omega)\cos(2\pi L\omega/c) \tag{6.1}$$

where ω is the terahertz frequency being operated at; I_{ph} is the photocurrent measured by the receiver; E_{THz} is the amplitude of the terahertz electric field; ϕ is the S_{21} phase; L is the length difference between the receiver arm and the emitter arm with the terahertz path; and c is the speed of light. Since I_{ph} can be measured, the phase ϕ can be calculated using an arc-cosine function if E_{THz} is known. E_{THz} can be determined by observing the extrema and zero crossings of I_{ph} and

the characteristics of the cosine function. The relations between I_{ph} and E_{THz} is shown in Figure 6.6. Based on the characteristic of the cosine function, the zero crossing points of I_{ph} corresponds to ϕ = -90º and +90º phase, while the extrema of I_{ph} represents ϕ = 0º and 180º. Therefore, E_{THz} is determined to the value of the I_{ph} extrema and it remains constant between two zero crossings to fit the cosine characteristic of the function ($I_{ph} <= E_{THz}$), allowing the successful retrieval of ϕ using arc-cosine.

By analyzing the photocurrent data for different applied voltages between 0.2547THz to 0.2588THz, the phase vs voltage relation of the TGFMM device is successfully characterized. Figure 6.7a shows the phase vs voltage relation across the frequency range of interest, which shows that there is significant phase change at 0.25735THz with a maximum phase change of 65.2257°. This result deviates from the optimal frequency of 0.2539THz predicted by the simulation with unitcell bounary and it has maximum phase change is higher than the predicted phase change of 42.1512º. This variation is possibly contributed by 1) boundary condition change as discussed in Section 4.3 and 2) the geometry deviations of device (thickness and uniformity of PDLC layer and PET substrate) introduced in the fabrication process.

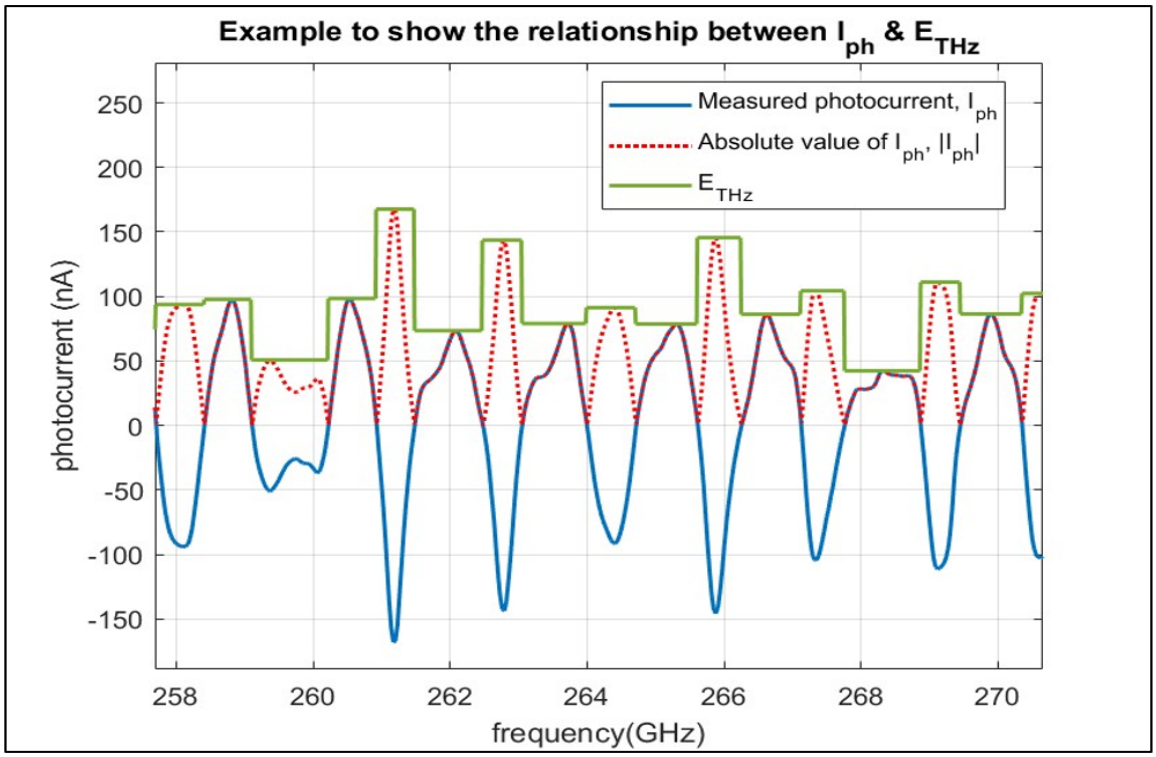

Figure 6.6. Visualization of the relationship between I_{ph} and E_{THz}

Figure 6.7b gives us a better view at the relative phase change vs voltage characteristic of the device at the optimal frequency. . It can be observed that the relative phase change and voltage is not linearly correlated. The phase will show minimal changes at near the turn on voltage and saturation voltage, while it will show drastic changes in the operating region. This matches closely with the voltage characteristic of the PDLC and agrees with the frequency shift pattern of S21 dips discussed in Section 6.1.1.

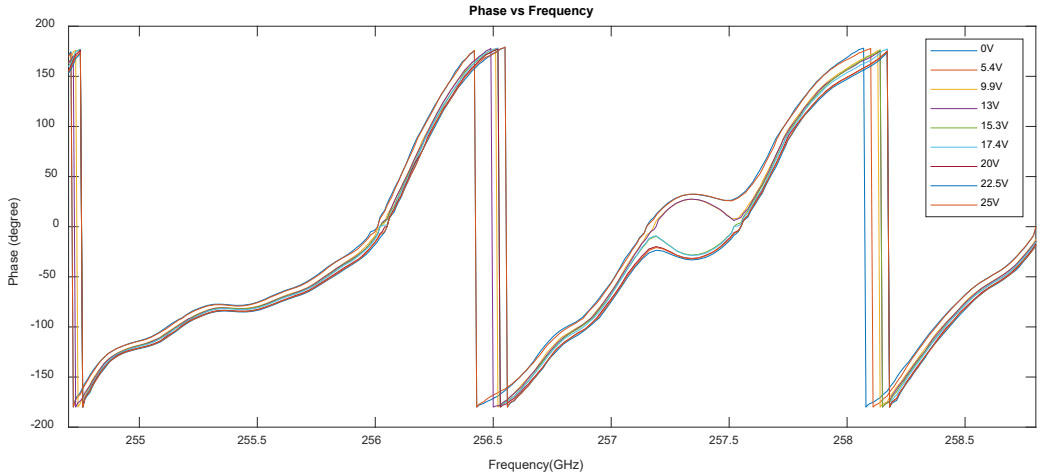
Phase vs Frequency
Phase (degree)
Frequency(GHz)
0V
5.4V
9.9V
13V
15.3V
17.4V
20V
22.5V
25V

(a)

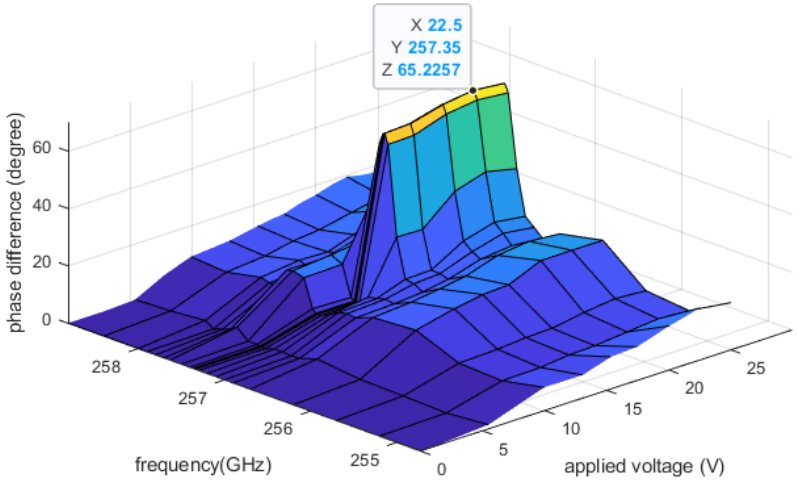
X 22.5
Y 257.35
Z 65.2257
phase difference (degree)
frequency(GHz)
applied voltage (V)

(b)

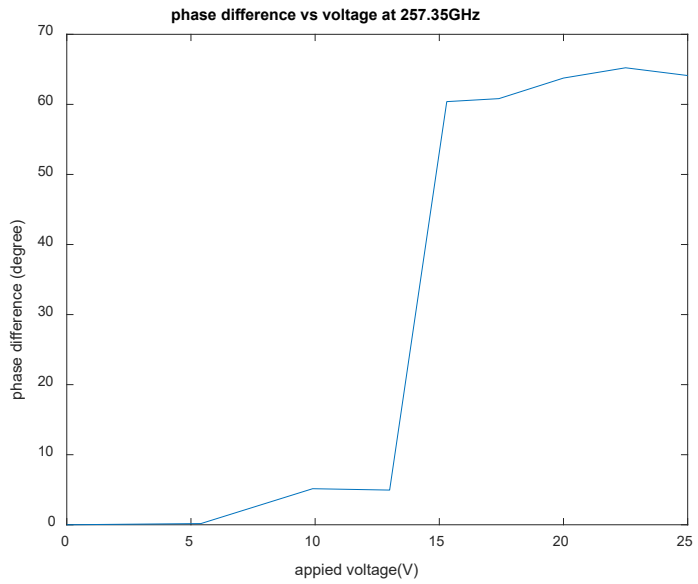

(c)

Figure 6.7. a) Phase vs frequency chacteristic of the TGFMM device at different applied voltages b) 3D visulaization of absolute phase difference vs voltage vs frequency characteristic for TGFMM device. c) absolute phase difference vs voltage for frequency with maximum phase shift

6.2 BEAM MANIPULATION

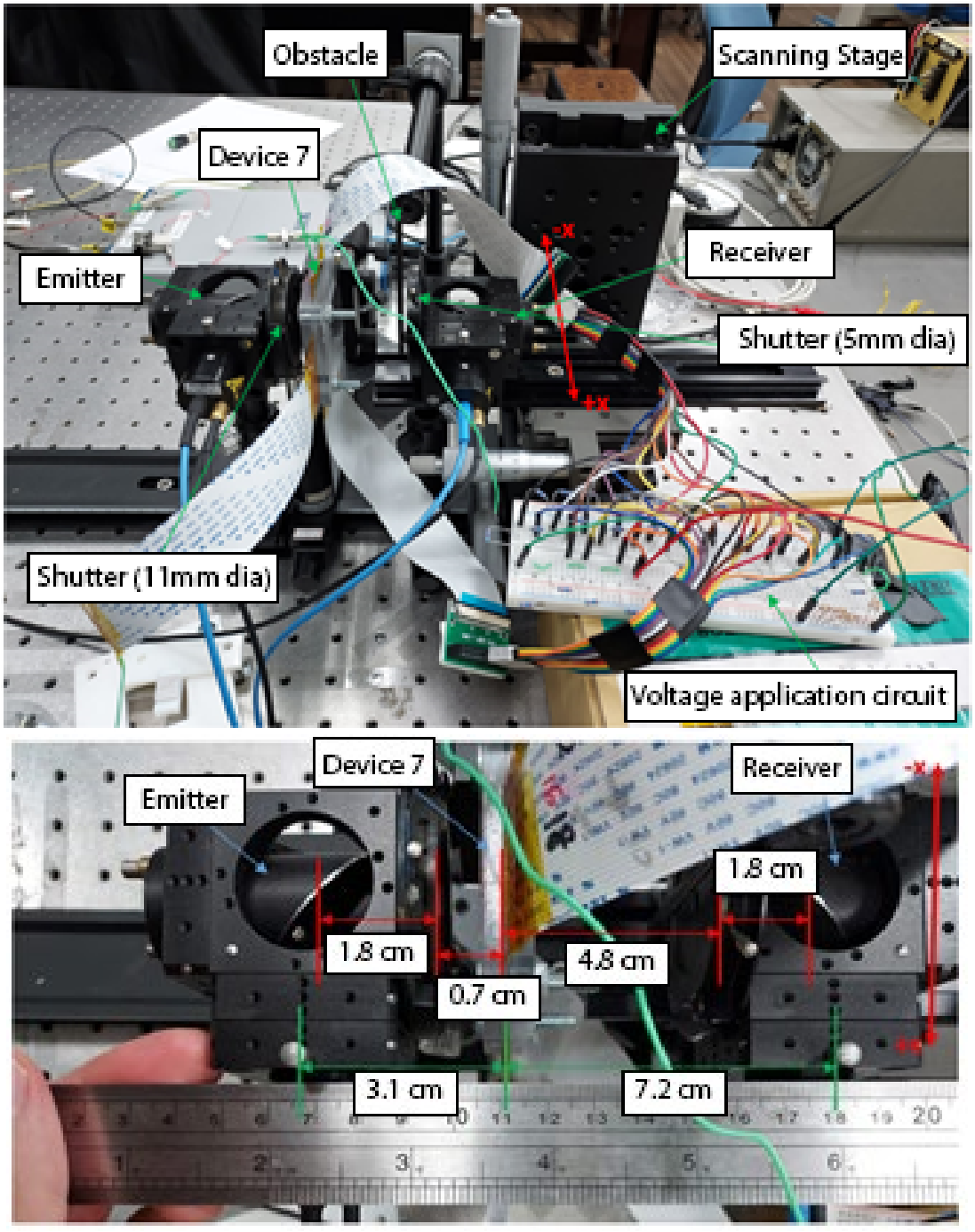

Figure 6.8. System setup to acquire one dimensional beam profile with the receiver of TeraScan1550 mounted on a mechanical stage.

Conventional beam profiling often involves the use a CCD camera, which is an array of photoelectric or bolometric sensors. However, current commercially available cameras, such as Rigi S2 from Swiss Terahertz, Tzcam from i2S, and Tera 256 from TeraSense are not able to capture a THz beam profile transmitted through our fabricated TGFMM device due to the weak intensity of the transmitted THz beam. To improve the sensitivity of the beam profiling setup, the receiver from the TeraScan 1550 system is used in place of cameras and sensor arrays due to its extremely high sensitivity to its own emitter pair. A scanning system to acquire THz beam profile is shown in Figure 6.8. The overall system setup is similar to the system characterization experimental setup with 3 changes: 1) The receiver from TeraScan 1550 system is mounted on a three-dimensional mechanical stage to perform linear scanning of the output beam profile. 2) The voltage driving circuit is redesigned to allow the application of non-uniform voltage profiles. 3) An additional shutter is place in front of the receiver to allow the adjustment of detection pixel size. to the TGFMM device. The aperture of the additional shutter serves as the "pixel" of our scanning detection; therefore, it is ideal to have the aperture size as small as possible to maximize the resolution of our scan. Thus, the output aperture is set to its minimum possible opening at 1.5mm diameter.

For testing the TGFMM device's ability in beam manipulation, the driving circuit has been reconfigured so that it can apply voltages to the desire columns of the array to form a 6-element phased array pattern. The phase pattern from the preliminary study is not used for its shortcomings described in Section 4.3. As described in Chapter 1, phased array functions by introducing different phase delay to different parts of an incident wave its array elements. The phase delay difference between consecutive array elements must be constant in order to create the desired constructive interference, which forms an output wave front deflected at an angle. The relation between the

output deflection angle θ and the phase difference between consecutive array elements Δφ in a phased array is described by (6.1):

$$\theta = \sin^{-1}\left(\frac{\lambda\Delta\varphi}{2\pi d}\right) \tag{6.1}$$

where d is the center-to-center distance of each element and λ is the wavelength of the input wave. Columns of the array has been divided into 6 groups, each representing an element of the phase array and a voltage divider is set up using potentiometers. The voltage for the corresponding phase difference is obtained from the phase difference vs voltage curve shown in Figure 6.7c. Potentiometers are used instead of conventional resistors to account for the different voltage-phase relation at different voltages and ensure that the correct voltages and the phase delay is set for each group.

Table 6.1, and Table 6.2 shows the voltage and phase distribution for phase array configuration with 10.62°, and 12.75° phase difference between each element, respectively. It can be observed that the resistance needs to be adjusted for Group 1 and Group 2 element in order to obtain the desired phase delay due to the different voltage-phase relation at lower voltages.

Table 6.1. Voltage and phase distribution for 6-element phase array with 10.62° phase difference

Group	Phase change assigned (degrees)	Calculated voltage (V)	Resistance (k Ohm)	Actual voltage (V)
1	-0.21	5.4	163.23	5.37
2	-8.69733	13.23	236.62	13.26
3	-17.1847	13.67	13.3	13.71
4	-25.672	14.11	13.3	14.16
5	-34.1593	14.55	13.3	14.62
6	-42.6467	15.00	13.3	15.08

Table 6.2. Voltage and phase distribution for 6-element phase array with 12.75° phase difference

Group	Phase change assigned (degrees)	Calculated voltage (V)	Resistance (k Ohm)	Actual voltage (V)
1	-0.21	5.4	135.51	5.38
2	-12.962	13.32	198.6694	13.21
3	-25.714	13.85	13.3	13.74
4	-38.466	14.38	13.3	14.27
5	-51.218	14.91	13.3	14.8
6	-63.97	20	13.3	20.04

Figure 6.10a shows the normalized photocurrent intensity for beam profiles for the 0V voltage profile and the 2 different voltage profiles shown in Figure 6.9a (corresponding phase profile is shown in Figure 6.9b). It can be observed that beam profiles do not show a symmetrical gaussian pattern, but instead, they are asymmetrical profiles with multiple peaks. To effectively observe the beam manipulation effect of the applied phase profiles, it is best observed by comparing similar peak features of the captured beam profiles between different voltage profiles. Markers (up-side-down triangles) are placed on the captured beam profiles for identifying and comparing similar peak feature between each of the voltage profiles. For the voltage profiles from Figure 6.9a, it can be observed that the peak marker gradually moves towards the -x directions as the $\Delta\varphi$ between the elements increases with different applied voltage profiles. This is the expected result as the phase delay of the elements increases in the -x direction with increasing applied voltage, which causes the output wave front to angles towards the -x direction. The angle of the deflections for each of the beam profile are calculated using the x-displacements between the similar peaks (Δx) and also the distance of the receiver from the TGFMM device (d=72mm) using the following equation:

$$\theta = \tan^{-1}\left(\frac{\Delta x}{d}\right) \tag{6.2}$$

The results are shown in Table 6.3. The theocratical deflection angles are calculated using (6.1).

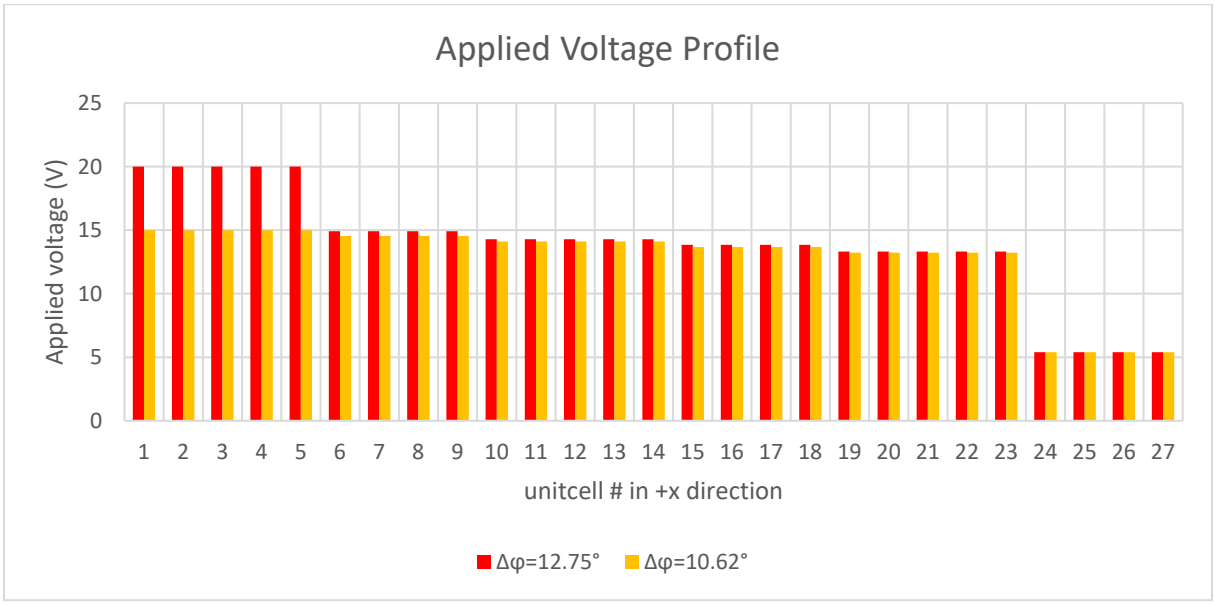

(a)

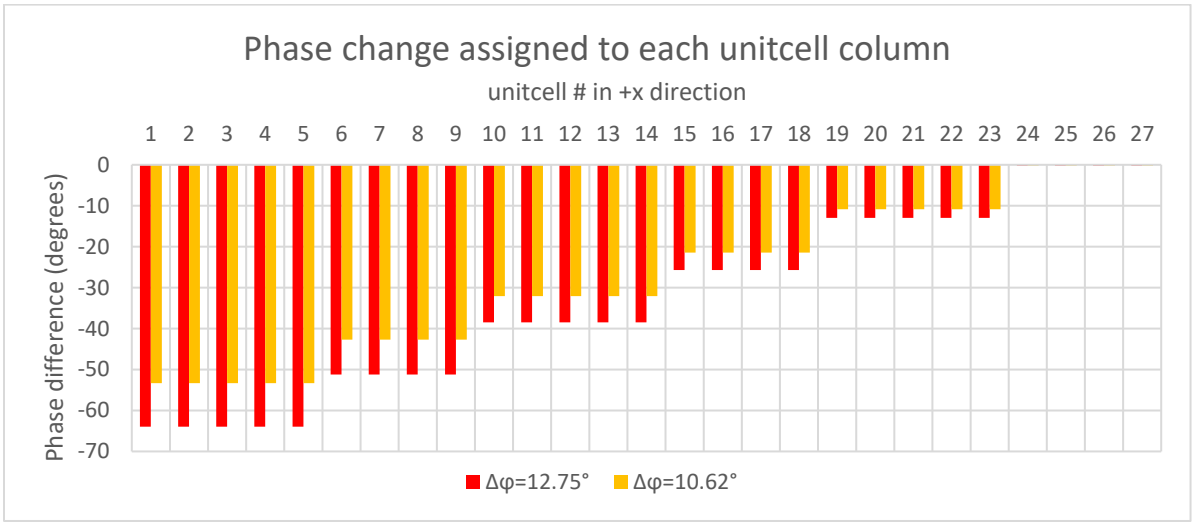

(b)

Figure 6.9. a) Voltages applied to each column of the TGFMM Device and b) the corresponding phase profile for -x direction shifting (negative phase value indicating phase lag)

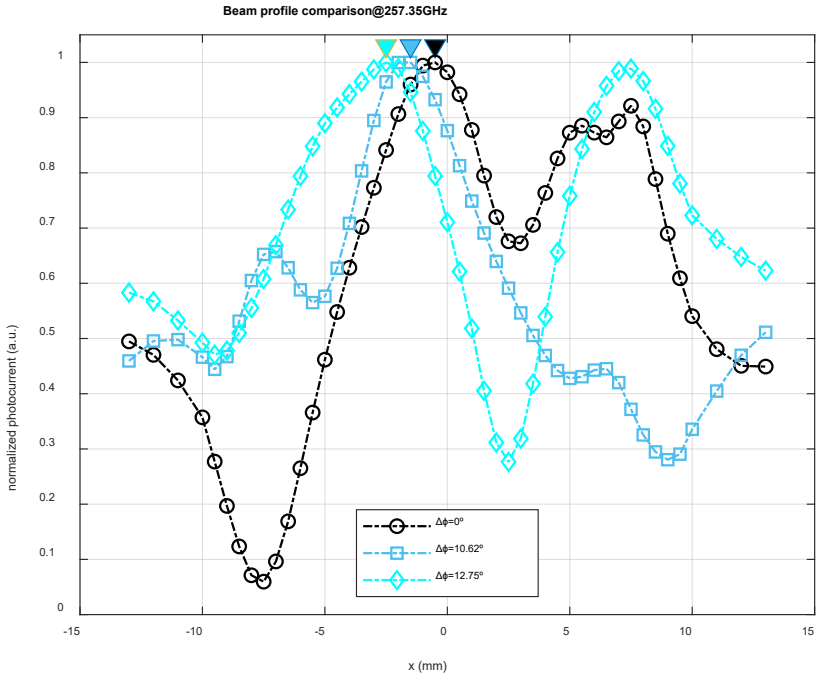

Figure 6.10. Measured beam intensity profiles for voltage and phase profiles from Figure 6.9, higher voltage in the -x direction.

Table 6.3. Deflection angle of the experimental result vs theocratical calculation using phase array equation.

$\Delta\varphi_{elements}$	Theoretical deflection angle	Experimental peak displacement	Deflection angle from experimental peak
10.62°	0.7882°	-1mm	0.7957°
12.75°	0.9463°	-2mm	1.5911°

The calculated deflection angle based on experimental peak displacements are generally larger than the theoretical angle predicted by (6.1), with the angle for $\Delta\varphi$=10.62° voltage profile being very close the theocratical calculation. Despite the deviation, the results demonstrated the TGFMM device's capability for controlled beam manipulation via the adjustment of phases of discrete elements in the array. The deviations from the theoretical calculations are likely due to the fact that the TGFMM device is a continuous array structure, as opposed to the discrete light source

elements found in phased array structure. Additionally, the measurements of the beam deflections are based on the comparison asymmetric multi-peak beam profiles, which can introduce additional errors when quantifying the deflections. The asymmetric multi-peak beam profiles are possibly the result of the following factors: 1) non-uniformity of the TGFMM device mounted in the acrylic holder due to the flexible nature of the materials, 2) scattering of the beam from the TGFMM array and the output aperture, and 3) distortion from the scanning aperture capturing method.

As discussed in Chapter 5, the fabrication of the TGFMM device on a flexible substrate is challenging. Despite of our efforts of mitigation during the fabrication process, the resulting device can still have variations in thickness and uniformity. With these variations, the surface profile of the device is not flat and even, which contributes to the distortion of the incident wavefront and the asymmetric characteristics of the results.

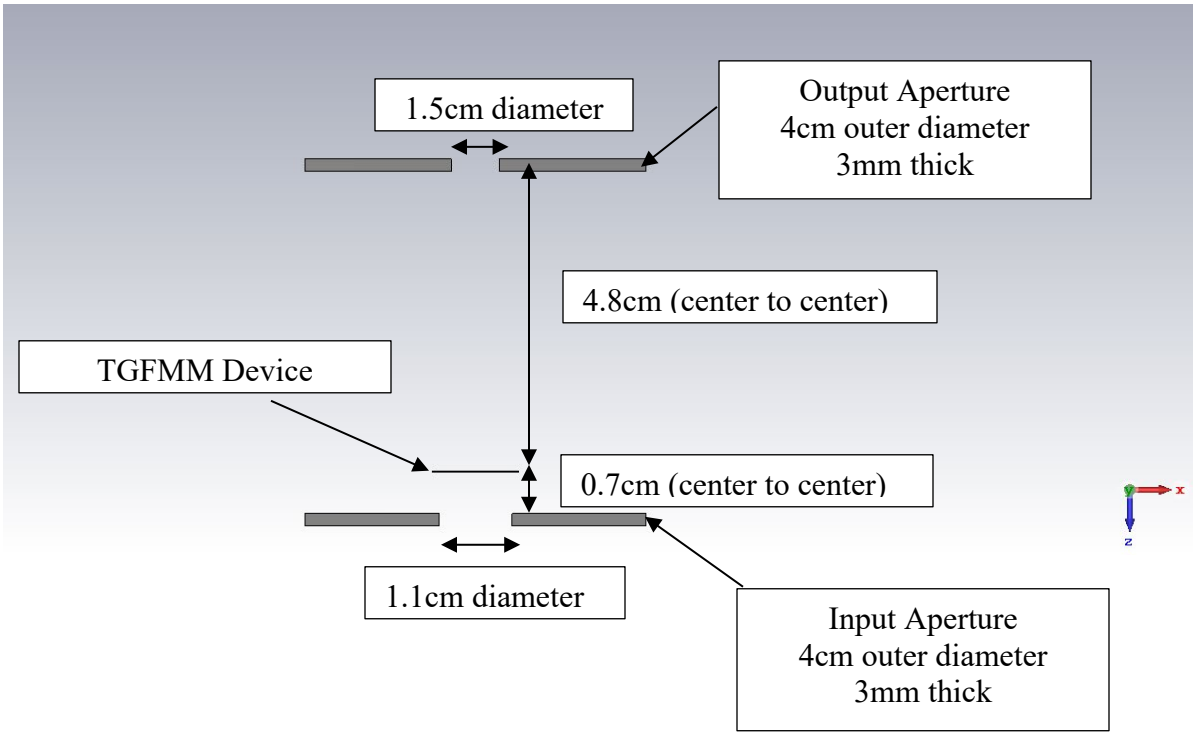

Figure 6.11. Top view of the simulation model for TGFMM device showing relative locations of the aperture, the TFGMM device and size of the apertures

To investigate the effects of the TGFMM array and the scanning aperture on the distortion captured beam profile, a numerical study will be performed using a simulation model that matches closely to the condition the experimental setup. The simulation model (shown in Figure 6.11) consists of the 27x27 TGFMM array placed between a 11mm input aperture and 1.5mm output aperture. The apertures and the TGFMM device are placed at the same locations as the experiment. The apertures will be modeled with Platinum (lossy metal). The boundary condition of the model will be open in all directions, matching the conditions of the experiment. First, the array is simulated with no phase difference between the columns of the array to check the effect of the 2nd aperture. Figure 6.12 shows the top cross-section view of the electric field propagation for the simulation model with 1 aperture and 2 apertures. It can be observed that adding in a 2nd aperture at the output of the device introduces modifications to the side peaks of the propagating electric field due to the introduction of additional reflections and interferences. The main peak of the beam is slightly distorted when it is near the opening of the aperture, which will certainly affect the shape of the overall beam profile.

To fully explore the distortion of the beam, the 2nd aperture is scanned linearly in the x-direction and the intensity of the electric field behind the 2nd aperture is recorded to emulate the scanning of the sensor during the experiment. As shown in Figure 6.13, the x-direction scanning of the 2nd aperture does not add significant distortions to the beam profile and the intensity of the main lobe and side lobe remains consistent, besides when the opening of the aperture is positioned near the main lobe. It can also be observed that when the aperture is shifted to extreme positions, there will be beam leaking from the side of the aperture, causing additional disturbance in intensity. Figure 6.14 shows the total electric field intensity captured over the sensor area when the 2nd aperture is shifted to different x-positions and also the 3D plot of the beam intensity profile at the

same position for the model without the 2nd aperture. The peaks shown in the sensor's profile are wider and closer to the center compared to beam profile without the 2nd aperture and it does not have the lower peak at the center. This is due to 1) additional distortion and interferences introduced by the 2nd aperture, 2) capturing a 2D image with 1D scanning, and 3) significantly lowered intensity due to the small opening of the aperture. Despite these effects, the major characteristics of the beam profile and the position of the beam profile is successfully captured by the scanning aperture and it will be sufficient when used as a reference for observing the beam manipulation capability of the TGFMM array.

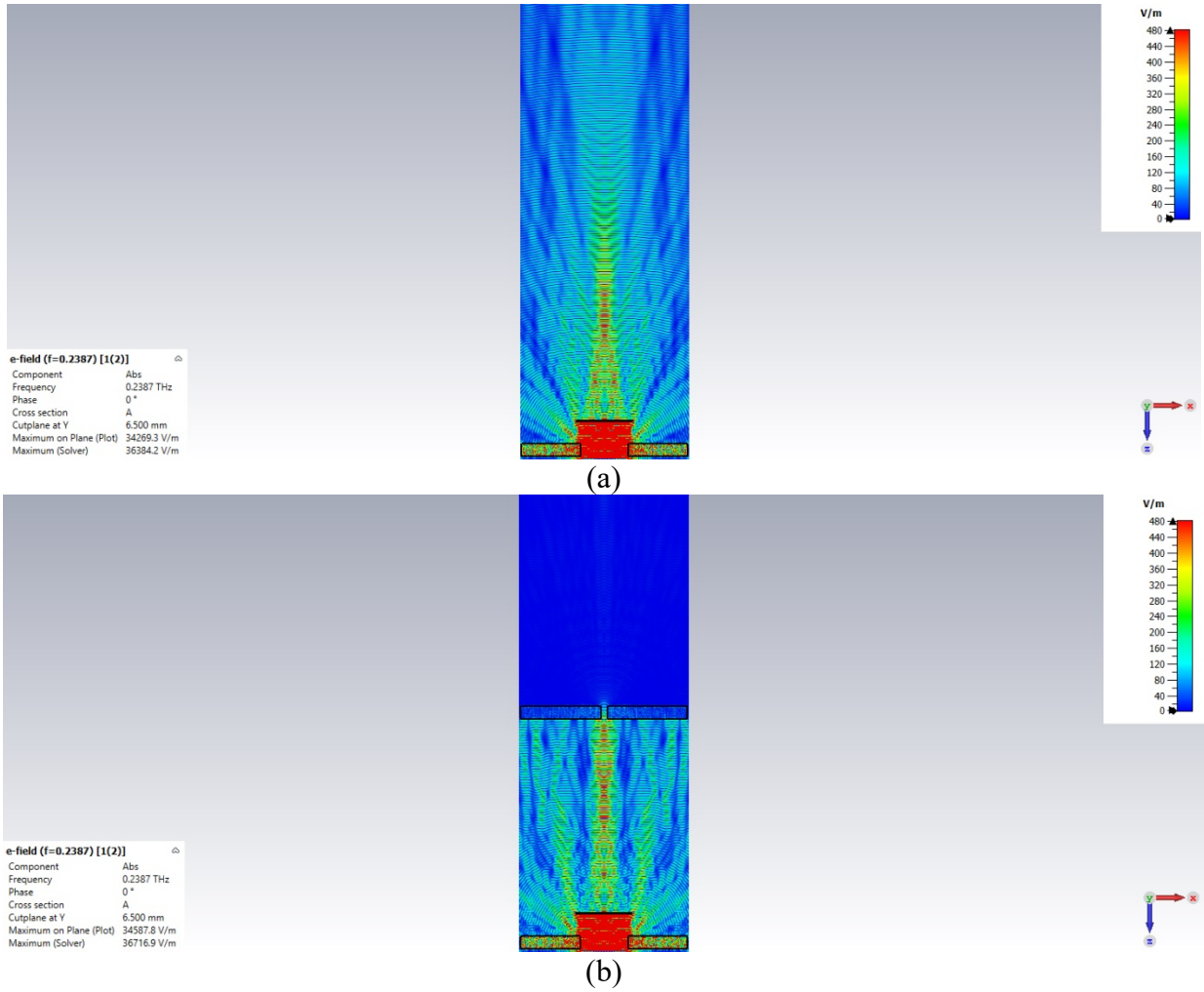

Figure 6.12. Top cross-section view of the electric field propagation for TGFMM device model (no voltage applied) with a) 1 aperture and b) 2 apertures.

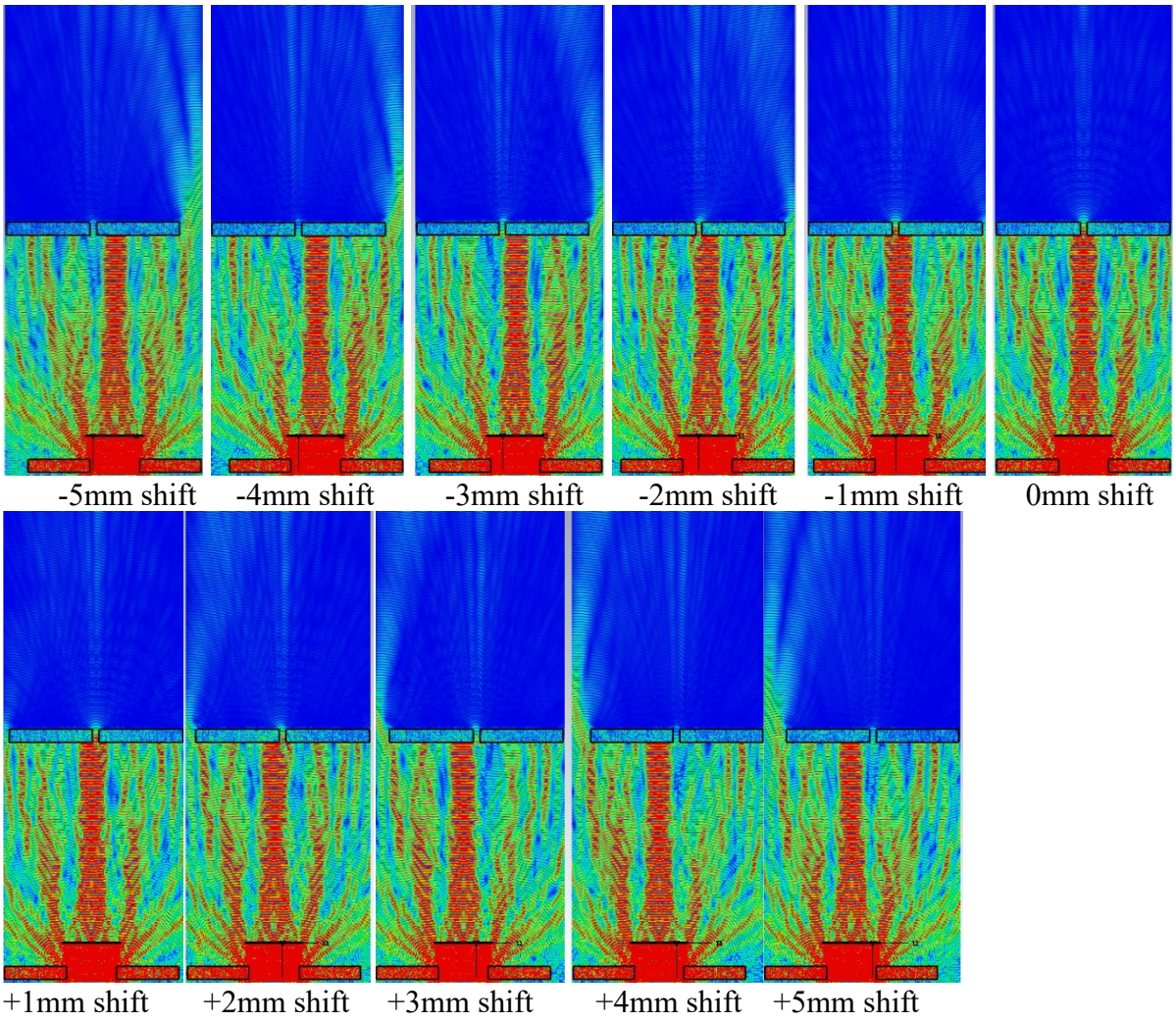

Figure 6.13. Top cross-section view of the electric field propagation for TGFMM device model with no voltage applied at different 2nd aperture x-positions.

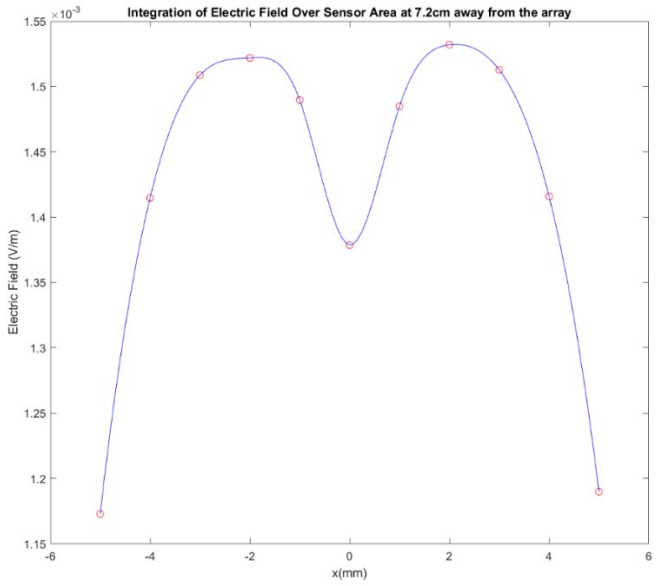

(a)

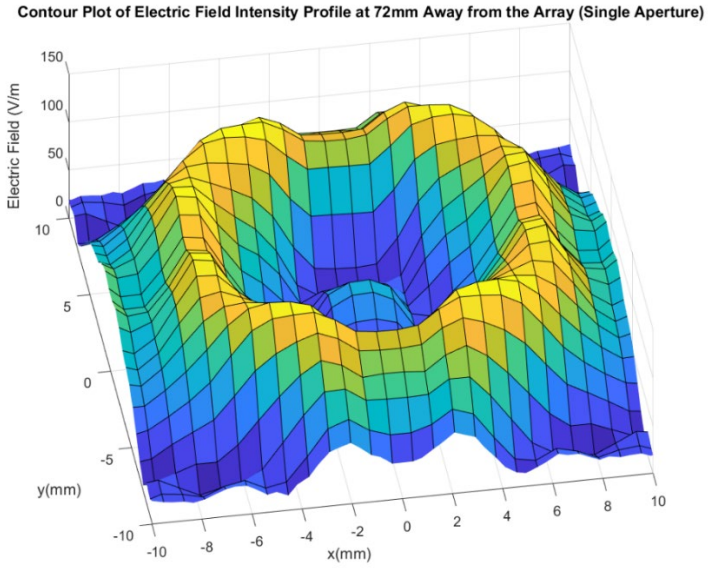

(b)

Figure 6.14. a) Electric field intensity integration over the area of the sensor at different 2nd aperture x-positions and b) Electric field intensity plot at the sensor location for TGFMM device model with no voltage applied.

Next, the array is simulated by applying a phased array-like phase profile to the elements of the array similar to the experiment. The phase delay of the array is first characterized to ensure the application of the desired phase profile is applied in the numerical study. Figure 6.15 shows the phase delay characteristic of the simulated 27x27 TGFMM array for PDLC permittivity states at different applied voltages. It can be observed that the maximum phase delay occurs at a different frequency compared to the 10x10 array from the preliminary study and also the array from the experiment. The deviation in the frequency and phase characteristic expected due to the deviations in the preliminary study and the experiment, thus it shows the necessity to characterize the phase delay behavior in order for a proper comparison of the results between the simulation and the experiment.

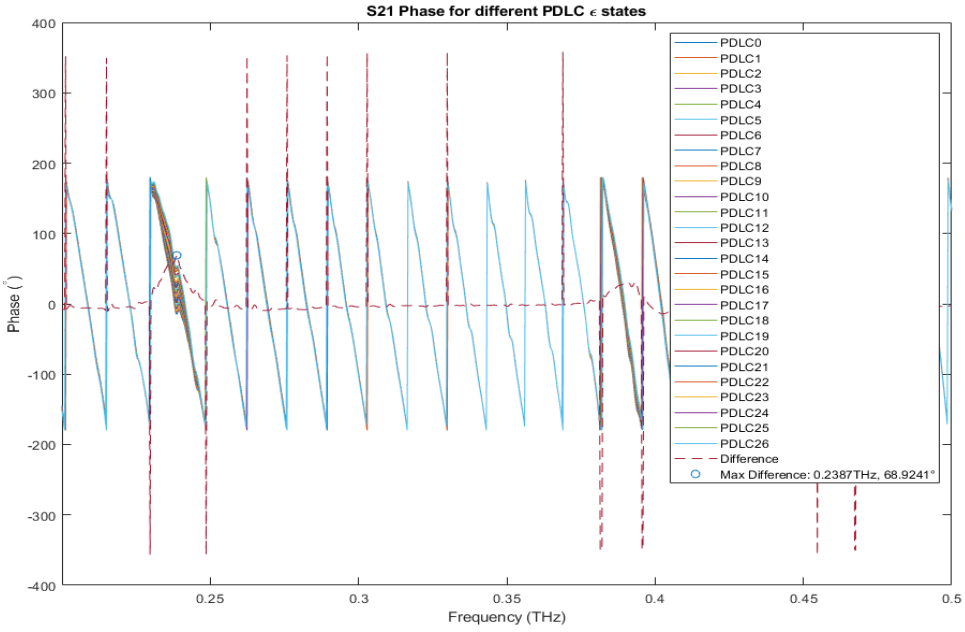

Figure 6.15. Phase delay characteristic of the 27x27 TGFMM array simulation model for different PDLC permittivity states.

With the phase delay characteristic obtained, a phase delay profile similar to the experiment is applied accordingly. The phased array-like phase profile shown in Figure 6.16 is applied to the columns of the 27x27 array in the simulation model with a single aperture and 2 apertures, and the results are shown in Figure 6.17 and Figure 6.18, respectively.

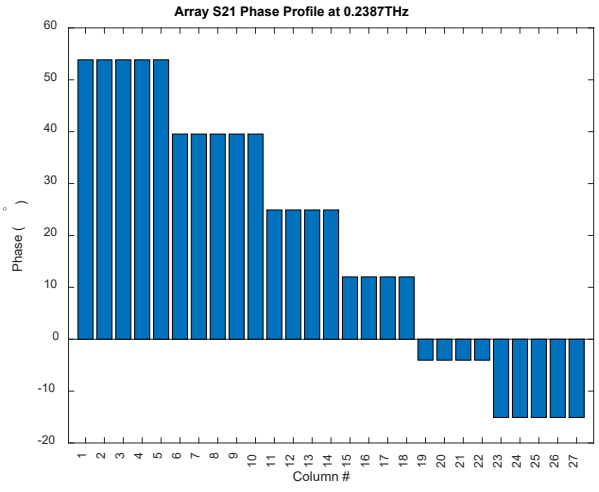

Figure 6.16. Phased array-like phase delay profile for steering the beam in the +x direction in the simulation (negative value indicates phase lag)

When the Phased array-like phase profile is applied to TGFMM array with a single aperture (Figure 6.17(a) and (b)), it can be observed that the TGFMM array is able to steer the beam in the +x direction, where the array has the higher phase delay. The far-field deflection of the main lobe is calculated to be 1.6°, which is matches closely with the angle (1.4°) predicted by applying the geometric parameters of the simulated array to (1). Figure 6.18 shows the electric field propagation for the TGFMM array with 2 apertures when the phased array-like phase profile is applied.

It can be observed that the 2nd aperture introduces a minor distortion to the main peak and additional side peaks similar to the results of the no-voltage TGFMM array simulation due to the reflection of side peaks from the 2nd aperture. It can be observed from Figure 6.19 that the

distortion remains consistent when the 2nd aperture shifts linearly in the x-direction, which means that the shifting of the aperture produces minor additional distortion to the beam profile.

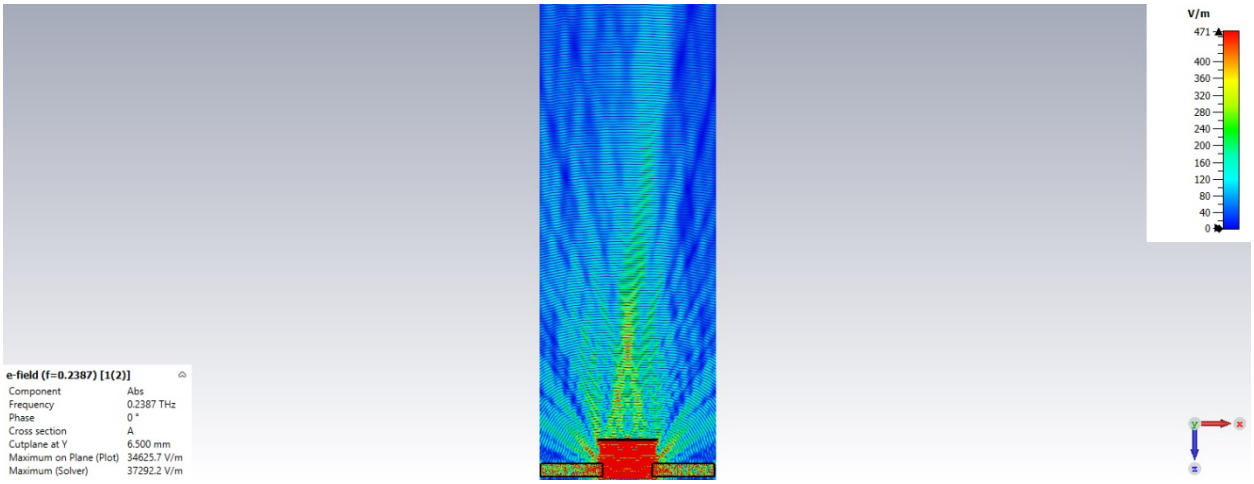

(a)

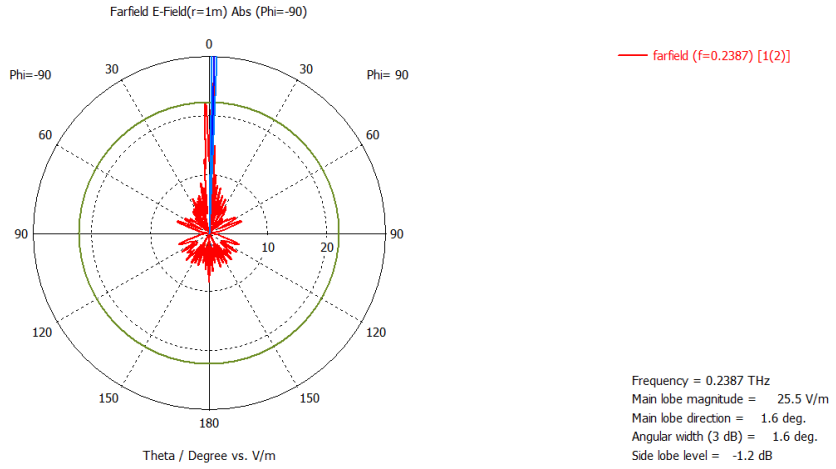

(b)

Figure 6.17. a) Top cross-section view of the electric field propagation and b) far-field result for TGFMM device model (phased array-like phase profile applied) with single aperture

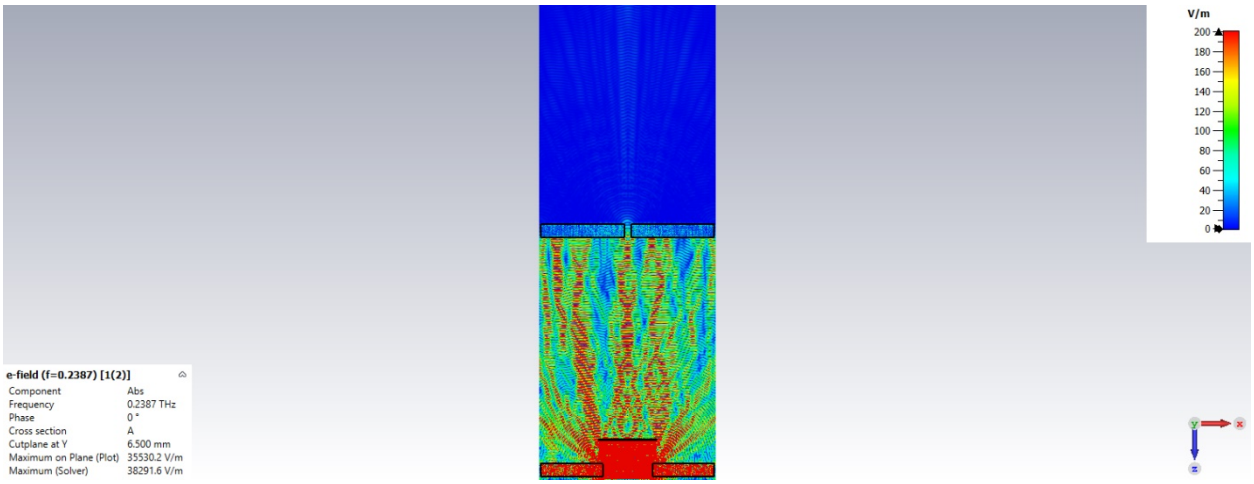

Figure 6.18. Top cross-section view of the electric field propagation for TGFMM device model (phased array-like phase profile applied) with 2 apertures

Figure 6.20 shows the total electric field intensity captured over the sensor area when the 2nd aperture is shifted to different x-positions and also the beam intensity profile at the same position for the model without the 2nd aperture. Distortions similar to the previous simulation with the TGFMM array when no voltage profile is applied can be observed. The key characteristics of the beam profile are captured with peaks closer to the center in comparison, and the center of the profile have lower intensity due to similar interferences when the center of main lobe is near the opening of the aperture.

Figure 6.21 shows the comparison of the electric field intensity obtained from scanning the 2nd aperture between the TGFMM device without a phase profile and the TGFMM device is a phased array-like phase profile. Due to the aforementioned distortions, the shifting of the beam shows up as a shift in peak intensity and a modification in the profile shape skewing towards the deflecting direction. This is consistent with the beam manipulation patterns that is observed in the experiments, where applying a phased array-like phase profile to the TGFMM array results in shifting and skewing of peaks in the resulting beam profiles towards the direction with a higher phase delay. It can be observed that the intensity and the shapes of the beam profiles from the

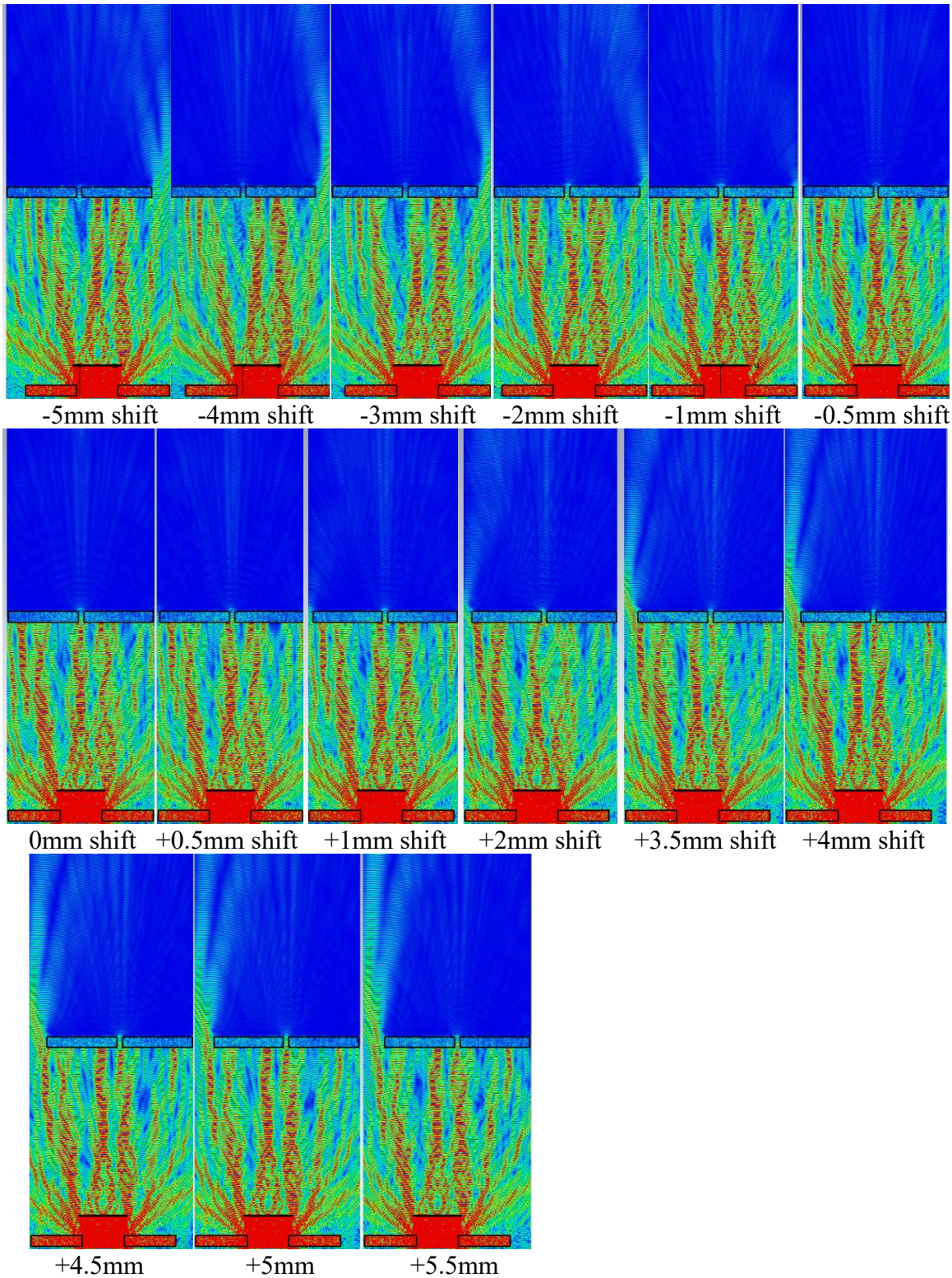

Figure 6.19. Top cross-section view of the electric field propagation for TGFMM device model (phased array-like phase profile applied) at different 2nd aperture x-positions.

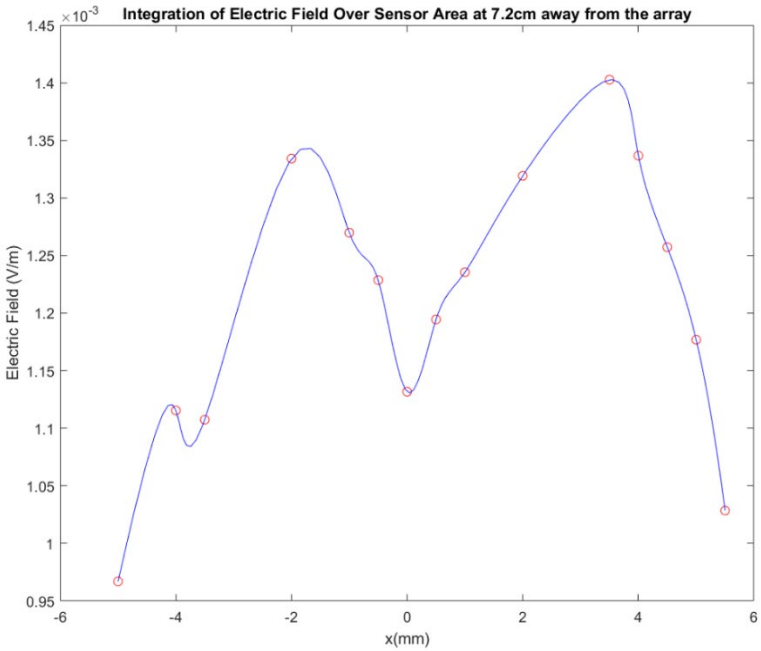

(a)

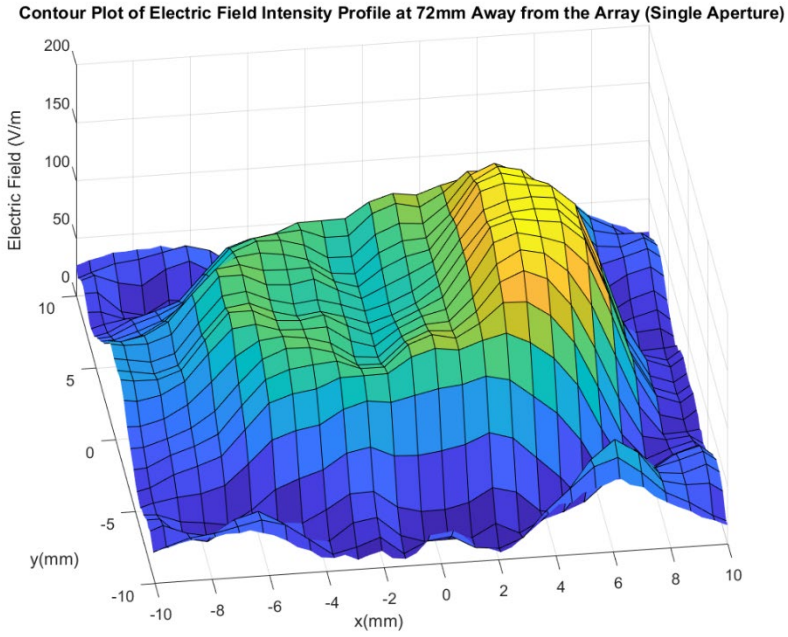

(b)

Figure 6.20. a) Electric field intensity integration over the area of the sensor at different 2nd aperture x-positions and b) Electric field profile at sensor location for TGFMM array with single aperture for TGFMM device model (phased array-like phase profile applied).

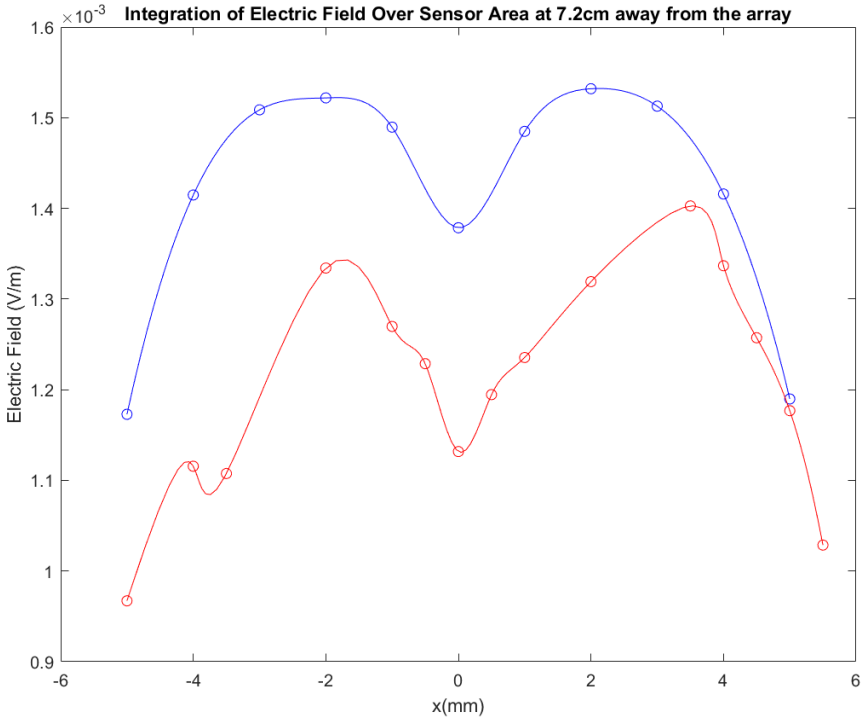

Figure 6.21. Electric field intensity integration over the area of the sensor at different 2nd aperture x-positions for TGFMM array without applied voltage profile (blue) and with phased array-like voltage profile (red)

simulation differs from the ones captured in the experiment. The error between the results is likely contributed by the differences between the simulation and experimental conditions, such as the mechanical condition of the device and deviations in the geometry of the experimental setup. The mechanical condition of the device affects how the propagating beam interfaces with the TGFMM device and also the phase delay that it experiences. The flatness of the device and the evenness of the PDLC layer will change the phase delay that is introduced to the different parts of the propagating beam causing deviation in beam modulation results. The phase delay is also affected by the performance of the PDLC, which can vary and degrade after repeated voltage application and magnetic field reset. The magnetic field reset process itself is also critical to the device performance, as the device doesn't have any alignment layer. However, current magnetic reset

method is completed manually and mechanically, which is not completely robust against errors and it might introduce minor mechanical perturbations to the TGFMM device during the reset process. It can be observed from the electric field propagation results of the simulation that the scanning method is sensitive to the geometric variations of the apertures since the intensity pattern varies quickly with the measurement distance. These deviations are minimized with efforts in matching the simulation and experimental conditions, and by observing and comparing the relative changes of the similar features in the beam profiles patterns, the TGFMM array simulations shows similar beam manipulation pattern compared with the experiment, where the similar peak of the beam shifts towards the direction that has a higher phase. This validates the results of the beam manipulation experiment. The simulation and experimental results also reveal the short coming of beam profiling using the scanning aperture, as it introduces some distortion to the beam profile itself. While these distortions can possibly be characterized due to its consistency, it might require advanced image processing technique and pattern recognition algorithms to accurately correct the distortion and quantify the performance measurement of the device.

Chapter 7. CONCLUSION AND FUTURE WORKS

7.1 CONCLUSION

The goal of this research is to develop a voltage tunable periodic structure for beam manipulation in the Terahertz (THz) region. Chapter 1 reviews the current beam manipulation technologies and also how the proposed device fits into the applications of Terahertz radiation.

Chapter 2 reviews prior beam manipulation research project that inspires the development of the proposed Tunable Gradient Fishnet Metamaterial (TGFMM) device and Chapter 3 discusses the design of the device, which utilize the large refractive index change in fishnet structures and tunability of electro-optics materials, such as Polymer Dispersed Liquid Crystal (PDLC). A circular geometry is selected for our design for its ability to reduce surface current density, which makes the device less prone to breakdown during operation. Chapter 3 also discusses the improvement of transmission and simplification of the device structure by using PET as a flexible substrate.

In Chapter 4, the geometric parameters of the design are optimized so that it can produce a large phase change in the desired frequency region between its OFF and ON state, which is critical to the objective of TGFMM. The refractive indices for the devices' OFF and ON state is also retrieved from the numerically calculated S-parameters of the device to compare with the results of the phase change investigation, and it is found that the maximum phase change and maximum refractive index change occurs a similar frequency. Refractive index is further verified using a geometrical analysis method, which allowed us to verify possible ambiguity in solutions provided by parameter extraction method. The geometric analysis is able to confirm the characteristic of the refractive index within the interested frequency range. Chapter 4 also shows a numerical preliminary study to verify the TGFMM's ability as a voltage tunable beam manipulator in the

THz frequency region. The preliminary study concludes that the TGFMM design is able to emulate a 6-element phased array to deflect an incident beam.

Chapter 5 discusses the challenges during the fabrication process. The removal of the skin layer from the previous design has simplified the design structure and the fabrication process, however, there are new considerations when fabricating the device on flexible PET substrates to minimize feature defects and maintain the flatness and evenness for each layer of the device.

In Chapter 6, the prototype TGFMM device is characterized in experiments. The frequency, phase, and voltage characteristic of the device is first investigated to ensure optimal performance is achieved in the experiments and device breakdown due to excessive voltage is avoided. The operating voltage range is determined to be 5.4V-22.5V, which is significantly lower than the previous tunable fishnet and electro-optic scanner designs. Next, the optimal frequency, the one that yields the largest phase change, is determined. The optimal frequency of the prototype is determined to be at 0.25735THz, which also deviates from the preliminary simulation results. The reported maximum phase difference (65.2257°) is also noticeably larger compared to the numerical simulation result (42.1512º). The deviation of the optimal frequency and maximum phase difference is possibly contributed by the permittivity deviation discussed earlier and as well as the effect of changes in boundary conditions discussed in Section 4.1.3. Custom phased array-like voltage profiles based on the phase and voltage characteristic at the optimal frequency are applied to the TGFMM prototype to test its beam manipulation capability. The output beam of the TGFMM prototype is profiled by scanning using the receiver of the continuous wave THz system (TeraScan 1550) for optimal signal sensitivity and we are able to capture gradual horizontal displacements of the beam profiles as the voltage of the gradient profiles increases by comparing similar peak features on the beam profiles. The beam profiles captured have observable distortions

that is likely to be caused by the TGFMM array, the output aperture and our scanning method, thus a numerical study with a simulation model that closely matches the simulation condition is performed to compared with our observations in the experiment. The numerical study shows similar beam intensity profile when they are captured with the scanning method used in the experiment, which goes to show that the beam profile distortion observed in the experiment is mainly caused by the scanning method. The numerical study also shows a similar beam manipulation pattern compared to the experiment, validating our experimental observation and so that the TGFMM array is capable of beam manipulation via the discrete control of phase delay in its array elements.

7.2 Future Works

7.2.1 *Improvement on Beam Profiling*

The current beam profiling method needs to be modified in order to eliminate or correct the distortion in the results. The following methods can potentially solve the issue and improve the profiling of the beam:

1) Characterize the distortion factor and correct it using advanced image processing technique.
2) Beam profiling using a THz-TDS system with 2D imaging capability to obtain 2D information of the beam profile.
3) Further investigation into the magnetic reset method to ensure consistent phase reset of the PDLC layer.

7.2.2 *Explore Additional Phase Profiles*

To further demonstrate the TGFMM's potential as a versatile beam manipulation device, additional phase profiles can be explored to emulate different optical components, such as concave lens, convex lens and near field beam shaper. Additionally, 2D gradient voltage profiles can be explored for doing 2D beam deflections. The additional profiles will require a reconfiguration in driving circuit to allow additional input and more fine control of the array.

7.2.3 *Image Acquisition*

With the reported success in beam deflection, the device shows its potential for image acquisition. The image of an object can be obtained by placing the object at the output of the TGFMM device in the beam profiling setup (Figure 6.8) and scanning it using the TGFMM deflected beam. The scanning beam will be captured by a beam profiler on the other end of the object and the image of the object is obtained by studying the beam profile of the beam pass through the object. The current beam profiling setup will allow us to obtain 1D information about the object, while a 2D beam profiling setup as proposed in Section 7.2.2 will allow us to obtain a 2D object profile.

7.2.4 *Multi-stage Beam Manipulation*

Multi-stage operation of the TGFMM device will be explore to expand and enhance its functionality similar to the multi-stage design of the previous EO scanner. System footprint will not be impacted significantly in the current design due to significant reduction in the size of the device. Additional analysis is needed to study the TGFMM's behavior in a multiple stage configuration to find the optimal system parameter, such as distance between the stages, incident angle of the input beam…etc., for the desired enhancement in functionality.

BIBLIOGRAPHY

[1] T. Chan, “Retro-modulators and fast beam steering for free-space optical communications”. Ph. D Dissertation, Department of Electrical and Computer Engineering, UC San Diego, San Diego, CA, 2009. Available: https://escholarship.org/uc/item/65f3t0t2

[2] Andrew C.-L. Hung, Harrison Y.-H. Lai, Ta-Wei Lin, Sheng-Gang Fu, Michael S.-C. Lu, “An electrostatically driven 2D micro-scanning mirror with capacitive sensing for projection display,” *Sensors and Actuators A: Physical*, Volume 222, 2015, pp. 122-129, Available: http://www.sciencedirect.com/science/article/pii/S0924424714004427

[3] A. Wilson, “Scanning Sensors”, 2010. [Online]. Available: https://www.vision-systems.com/articles/2010/12/scanning-sensors.html

[4] C. J. Sarabalis, R. Van Laer, and A. H. Safavi-Naeini, "Optomechanical antennas for on-chip beam-steering," *Opt. Express 26*, 2018, pp. 22075-22099.

[5] P.J. Rodrigo, V. Daria, J. Gluckstad, “Array of optical tweezers with individual beam-steering and polarization control.” *Proc. SPIE 5322*, Imaging, Manipulation, and Analysis of Biomolecules, Cells, and Tissues II, 1 July 2004, San Jose, CA, United States

[6] S-C Shen, C-T Pan, H-P Chou, “Electromagnetic optical switch for optical network communication”, *Journal of Magnetism and Magnetic Materials*. Volume 239(Issues 1–3), February 2002, pp. 610–613.

[7] V. Barua, H. Nayim, Mahmud Abdul Matin Bhuiyan, “A 2×2 MEMS Optical Switch Based on Piezoelectric Actuation”, *International Conference on Electrical and Computer Engineering, Dec 19–21, 2006, Dhaka*, p. 52-55.

[8] “Data sheet of 1205/06/50C-NIR AO Modulators at NIR”, Available: http://www.isomet.com/FinalWebSite/PDFDocs/AO%20Sheets/1205-1206-1250C%20NIR.pdf

[9] Mart B, Diemeer J. “Polymeric thermo-optic space switches for optical communications. Optical Materials,” *Materials, Physics and Devices For Molecular Electronics and Photonics*, Volume 9(Issues 1–4), Jan. 1998, pp. 192–200.

[10] Newport Corporation, “Electro-Optic Modulator Selection Guide” [Online], Available: https://www.newport.com/g/electro-optic-modulator-selection-guide

[11] Y. Zuo, M. Mony, B. Bahamin, E. Grondin, V. Aimez, and D. V. Plant, "Bulk electro-optic deflector-based switches," *Appl. Opt*. **46**, 3323-3331, 2007

[12] J.A. Abernethy, R.W. Eason and P.G.R. Smith, “Bulk optical Bragg deflectors at 1.064μm based on an electro-optically induced grating in periodically poled lithium niobate,” *CLEO/Pacific Rim 2001: The 4th Pacific Rim Conference on Lasers and Electro-Optics. 15 - 19 Jul 2001.*

[13] G. Teowee, J.T. Simpson, Tianji Zhao, M. Mansuripur, J.M. Boulton, D.R. Uhlmann, "Electro-optic properties of sol-gel derived PZT and PLZT thin films," *Microelectronic Engineering*, Volume 29, Issues 1–4, 1995 , Pages 327-330, ISSN 0167-9317.

[14] M. Heck, "Highly integrated optical phased arrays: photonic integrated circuits for optical beam shaping and beam steering". *Nanophotonics*, 6(1), 2016, pp. 93-107

[15] Q. Wang, X. Zhang, Y. Xu, Z. Tian, J. Gu, W. Yue, S. Zhang, J. Han, W. Zhang, "A Broadband Metasurface-Based Terahertz Flat-Lens Array,"*Advanced Optical Materials*, 3, 2015

[16] W. M. Zhu *et al*., "Tunable flat lens based on microfluidic reconfigurable metasurface," *2015 Transducers - 2015 18th International Conference on Solid-State Sensors, Actuators and Microsystems (TRANSDUCERS)*, Anchorage, AK, 2015, pp. 1989-1992.

[17] A. Komar, Z. Fang, I. Staude, M. Decker, A. E. Miroshnichenko, J. Bohn, R. Paniagua Dominguez, Y. F. Yu, A. I. Kuznetsov, Y. S. Kivshar, and D. N. Neshev "Liquid-crystal tunable metasurfaces for phase modulation and beam deflection (Conference Presentation)", *Proc. SPIE 10113, High Contrast Metastructures VI*, 1011316, April 28 2017

[18] P. Valley, D. L. Mathine, M. R. Dodge, J. Schwiegerling, G. Peyman, and N. Peyghambarian, "Tunable-focus flat liquid-crystal diffractive lens," *Opt. Lett*. **35**, 2010, pp. 336-338

[19] Y-K Fuh, J-K Chen, P-W Chen, "Characterization of electrically tunable liquid lens and adaptive optics for aberration correction", *Optik*, Volume 126, Issue 24, 2015, pp. 5456-5459

[20] C.-L. Chang, W.-C. Wang, H.-R. Lin, F. Ju Hsieh, Y.-B. Pun, and C.-H. Chan, "Tunable terahertz fishnet metamaterial," Applied Physics Letters, vol. 102, no. 15, p. 151903, 2013.

[21] Tao YH, Fitzgerald AJ, Wallace VP. Non-Contact, Non-Destructive Testing in Various Industrial Sectors with Terahertz Technology. Sensors. 2020; 20(3):712. https://doi.org/10.3390/s20030712

[22] https://terasense.com/applications/security/

[23] http://www.cetcthz.com/thzen/info_895.aspx?itemid=214

[24] Y. Liu, H. Liu, M. Tang, J. Huang, W. Liu, J. Dong, X. Chen, W. Fu, and Y. Zhang, "The medical application of terahertz technology in non-invasive detection of cells and tissues: opportunities and challenges", RSC Adv., 2019,9, 9354-9363

[25] https://terasense.com/applications/tds-fds-systems/

[26] W-C Wang, C. L. Tsui, “Two-dimensional mechanically resonating fiber optic scanning display system,” *Optical Engineering*, 49(9), 097401-097401-8, 2010.

[27] D. R. Schipf, C. Tsui, C. Kuo, Y. Wang, W. Wu and W. Wang, "Design of a PZT Actuated Cantilever Waveguide Scanner Using an Aerosol Deposition Process," *2014 International Symposium on Optomechatronic Technologies*, *Seattle, WA, 2014*, pp. 142-145.

[28] K. Gu, K-R Lin, W-C Wang, “2D MEMS electrostatic cantilever waveguide scanner for potential image display application”, *MATEC Web of Conferences 32 01002*, 2015

[29] Ming-Yao Li, Kuan-Cheng Peng, Yi-Feng Hsu, Peng-Jyun Chen, Chi-Leung Tsui, Wen-Jong Wu, Wei-Chih Wang, "Aerosol jet printed PZT actuated MEMS resonating cantilever scanner," Proc. SPIE 11283, Integrated Optics: Devices, Materials, and Technologies XXIV, 1128329 (25 February 2020)

[30] Wei-Chih Wang, Colin Yen, Kuang-Chen Peng, Yi-Feng Hsu, Wen-Jong Wu, "Aerosol jetted PZT actuated fiber MEMS scanner for potential microscopic imaging," Proc. SPIE 12045, Nano-, Bio-, Info-Tech Sensors, and Wearable Systems 2022, 120450C (18 April 2022)

[31] W.-C Wang, C. L. Tsui, B. Estroff, “2D Electro-Optic Scanner”, *ECS Transactions*, Vol 45, 2013, pp. 1-6.

[32] J. Luo, S. Huang, Z. Shi, B. M. Polishak, X-H, Zhou, Alex K-Y Jen, “Tailored Organic Electro-optic Materials and Their Hybrid Systems for Device Applications,” *Chemistry of Materials*, 23(3), 2011, pp. 544–553.

[33] Qing Ye, Zuoren Dong, Ronghui Qu and Zujie Fang, "Study of optical phased-array technology based on PLZT electro-optic ceramic," *2007 Asia Optical Fiber Communication and Optoelectronics Conference*, Shanghai, 2007, pp. 528-530.

[34] Qing Ye, Zuoren Dong, Ronghui Qu, and Zujie Fang, "Experimental investigation of optical beam deflection based on PLZT electro-optic ceramic," *Opt. Express*, Vol. **15**, 2007, pp. 16933-16944.

[35] Hua Jiang, Y. K. Zou, Q. Chen, K. K. Li, R. Zhang, Y. Wang, H. Ming, Zhiqiang Zheng, "Transparent electro-optic ceramics and devices," *Proc. SPIE 5644, Optoelectronic Devices and Integration, 17 January 2005*.

[36] G. Teowee, J.T. Simpson, Tianji Zhao, M. Mansuripur, J.M. Boulton, D.R. Uhlmann, “Electro-optic properties of sol-gel derived PZT and PLZT thin films”, *Microelectronic Engineering*, Volume 29, Issues 1–4, 1995, pp. 327-330.

[37] A. Glebov, V. Smirnov, M. G. Lee, L. B. Glebov, A. Sugama, S. Aoki, V. Rotar, "Angle Selective Enhancement of Beam Deflection in High-Speed Electrooptic Switches," *Photonics Technology Letters*, *IEEE*. 19, 2007, pp. 701 - 703.

[38] X.L. Tong, K. Lin, Dongxi Lv, M.H. Yang, Z.X. Liu, D.S. Zhang,"Optical Properties of PMN-PT Thin Films Prepared Using Pulsed Laser Deposition," *Applied Surface Science*, 255, 2009, 7995-7998.

[39] X. Guo, Q, Chen, K.K. Li, Y.K. Zou, H. Jian, "Electro-optic Effects of La-Modified PMN-PT Thin Films for Waveguide Applications," *Integrated Ferroelectrics*, 100:1, 2008, pp. 103-113.

[40] Y. Chen, Y. Zhang, D. Karnaushenko, L. Chen, J. Hao, F. Ding, O. G. Schmidt, "Addressable and Color-Tunable Piezophotonic Light-Emitting Stripes", *Adv. Mater.*, Vol 29, Issue 19, 2017.

[41] Boston Applied Technologies Inc., http://www.bostonati.com/products_EO%20thin%20films.html

[42] Epiphotonics, http://epiphotonics.com/products7.htm

[43] M. Kafesaki, I. Tsiapa, N. Katsarakis, Th. Koschny, C. M. Soukoulis, and E. N. Economou, "Left-handed metamaterials: The fishnet structure and its variations", *Phys. Rev. B* 75, 235114, June 19, 2007

[44] Isabel, Ana, et al. 'New Polymer Networks for PDLC Films Application'. New Polymers for Special Applications, InTech, 12 Sept. 2012. Crossref, doi:10.5772/48203

[45] K. Amundson, A. van Blaaderen, P. Wiltzius, "Morphology and electro-optic properties of polymer-dispersed liquid-crystal films," *Phys. Rev. E*. 55, 1997

[46] Hiroshi Ono, Hirohito Shimokawa, *and* Akira Emoto, "Photorefractive liquid crystal-polymer dispersion with different morphology", *Journal of Applied Physics*, 94, 2003, 23.

[47] Jose M. Sanchez-Pena, Carmen Vazquez, I. Perez, Inmaculada Rodriguez, Jose Manuel Oton, "Electro-optic system for online light transmission control of polymer-dispersed liquid crystal windows," Opt. Eng. 41(7) (1 July 2002) https://doi-org.offcampus.lib.washington.edu/10.1117/1.1481049

[48] Jin, Y.-S & Kim, G.-J & Jeon, S.-G. (2006). Terahertz dielectric properties of polymers. Journal of the Korean Physical Society. 49. 513-517.

[49] Khan, Muhammad Usman & Raad, Raad & Tubbal, Faisel & Theoharis, Panagiotis. (2021). The Impact of Bending on Radiation Characteristics of Polymer-Based Flexible Antennas for General IoT Applications. Applied Sciences. 11. 10.3390/app11199044.

[50] Z. Qin, C. Fang, Q. Pan et al. "Optical properties of NAEC-PMMA nonlinear polymeric thin film", *Journal of Materials Science*, Vol 37, 2002, pp. 4849-4852.

[51] E. Nitiss, A. Tokmakovs, K. Pudzs, J. Busenbergs, M. Rutkis, “All-organic electro-optic waveguide modulator comprising SU-8 and nonlinear optical polymer”. *Optics Express*, Vol.25, Issue 25, 2017, pp. 31036-31044.

[52] N. Shen, G. Kenanakis, M. Kafesaki, N. Katsarakis, E. Economou, C. Soukoulis, “Parametric investigation and analysis of fishnet metamaterials in the microwave regime,” *Journal of the Optical Society of America B: Optical Physics*. Vol 26. B61-B67, 2009

[53] Chi-Leung Tsui, Wei-Chih Wang, "Investigation of tunable fishnet metamaterials for optimal phase shift effect," Proc. SPIE 12000, Terahertz, RF, Millimeter, and Submillimeter-Wave Technology and Applications XV, 120000F (7 March 2022); https://doi.org/10.1117/12.2613806

[54] A. Sahu, T.V. Filippov, M. Radparvar, D. Kirichenko, & D. Gupta (2017), “Digital Time-Division Multiplexing Readout Circuit for Sensor Arrays,” *IEEE Transactions on Applied Superconductivity*, 27, 2017, pp. 1-6.

[55] Jack R. Kelly, Desmond L. Seekola, "Dielectric losses in a polymer-dispersed liquid crystal film," *Proc. SPIE 1257, Liquid Crystal Displays and Applications,* April 1, 1990.

[56] T. R. Tsai, C. Pan, C. Y. Chenc, R. Pan, and X. -. Zhang, "Characterization of Liquid Crystals 5CB In Terahertz Frequency," in Conference on Lasers and Electro-Optics, M. Fejer, F. Leonberger, J. Fujimoto, and S. Newton, eds., OSA Technical Digest (Optica Publishing Group, 2002), paper CFD7.

[57] X. Chen, T. M. Grzegorczyk, B. Wu, J. Pacheco, and J. A. Kong, "Robust Method to Retrieve the Constitutive Effective Parameters of Metamaterials", *Phys. Rev. E.*,70, 016608, 2004.

[58] Wegrowski, A., Wang, WC. & Tsui, C. Three cases of discontinuous refractive index in metamaterial study. Sci Rep 12, 3558 (2022). https://doi.org/10.1038/s41598-022-07537-1

[59] Feng-Ju Hsieh and Wei-Chih Wang, “Full extraction methods to retrieve effective refractive index and parameters of a bianisotropic metamaterial based on material dispersion models”, *Journal of Applied Physics*m, Vol 112, 064907, 2012.

[60] https://www.sciencedirect.com/topics/engineering/electron-beam-evaporation

[61] Saedi. A., Rost. M.J, “Thermodynamics of deposition flux-dependent intrinsic film stress,” Nat. Commun. 7 10733, 2016.

[62] A. L. Del Vecchio, F. Spaepen," The effect of deposition rate on the intrinsic stress in copper and silver thin films,” Journal of Applied Physics 101, 063518, 2007.

[63] Shull, A. L. & Spaepen, F. “Measurements of stress during vapor deposition of copper and silver thin films and multilayers,” J. Appl. Phys. 80, 6243–6256, 1996.

[64] http://www.deya.com.tw/products/176

VITA

Chi Leung (Addison) Tsui was borned in Hong Kong. He moved to Seattle, USA at a very young age and lived and studied there since. He earned his bachelor degree in Electric Engineering (2008) and master degree in engineering (2012) at the University of Washington, Seattle. In 2023, he earned his Doctor of Philosophy in Electrical and Computer Engineering at the University of Washington, Seattle.